

LAPPEENRANTA UNIVERSITY OF TECHNOLOGY

LUT School of Energy Systems

LUT Mechanical Engineering

Mehran Ghafouri

**SOLID-STATE PHASE TRANSFORMATION INCORPORATED WELDING
SIMULATION AND PREDICTION OF RESIDUAL STRESSES AND
DEFORMATIONS OF ULTRA-HIGH STRENGTH STEEL STRENX®960 MC**

Examiners: Prof. Timo Björk

M. Sc. (Tech) Tuomas Skriko

ABSTRACT

Lappeenranta University of Technology
LUT School of Energy Systems
LUT Mechanical Engineering

Mehran Ghafouri

Solid-state phase transformation incorporated welding simulation and prediction of residual stresses and deformations of ultra-high strength steel Strenx[®]960 MC

Master's Thesis

2018

124 pages, 44 figures, 9 tables

Examiners: Professor Timo Björk
M. Sc. (Tech) Tuomas Skriko

Keywords: welding residual stresses, solid-state phase transformation, USDFLD, UEXPAN, finite element simulation, ultra-high strength steel

This study investigates prediction of transverse residual stresses as well as angular and bending distortions in bead on plate welding of the low carbon ultra-high strength steel Strenx[®]960 MC by developing a three-dimensional sequentially-coupled thermal, metallurgical and mechanical finite element model in ABAQUS. Modelling the heat source was carried out considering a volumetric heat source based on the Goldak's double ellipsoidal heat source model implemented in DFLUX user subroutine. Modelling the heat loss was accomplished using the FILM user subroutine. The effect of solid-state phase transformation during welding was included in numerical model through applying volumetric changes induced by austenitic, bainitic and martensitic transformations based on dilatometric tests and continuous cooling transformation (CCT) diagram of the material under investigation. User subroutine USDFLD was developed to determine volume fraction of present phases based on the available mathematical kinetics models for diffusive and displacive transformations. Modification of thermal expansion coefficient was performed using user subroutine UEXPAN in ABAQUS in which volumetric changes during phase transformations were incorporated. The results of simulations indicate that distortions and residual stresses in particular, are significantly affected by solid-state bainitic and martensitic transformations.

ACKNOWLEDGEMENTS

First and foremost, I would like to express my profound gratitude to my supervisor professor Timo Björk for his continuous support and guidance during my thesis work and research. Mr. Tuomas Skriko is thanked for his support and commenting on this thesis.

Dr. Joseph Ahn from Imperial College London is highly appreciated, and I am deeply indebted to him for his fruitful comments and advices in simulation with ABAQUS. Professor Jari Larkiola from University of Oulu is warmly acknowledged for his valuable comments on modeling. Juho Mourujärvi is sincerely thanked for his patience in conducting dilatometric and hot tensile tests in University of Oulu and his close cooperation in metallurgical aspects of the research project.

My deep gratitude goes to my colleague Mr. Antti Ahola for his kind efforts in arrangement of welding tests and measurements. I would also like to thank the personnel of the laboratory of steel structures and laboratory of welding technology for their assistance and performing the experiments in Lappeenranta University of Technology. Special thanks to my friends and colleagues Mr. Mohammad Dabiri and Mr. Shahriar Afkhami for their useful discussions to improve my work.

Financial support of Business Finland (TEKES), DIMECC and SSAB is highly appreciated. CSC - IT Center for Science Ltd. is acknowledged for providing the computational resources.

Last and most importantly, my everlasting thankfulness and respect towards my supportive and beloved parents and sister whose unconditional love, care and encouragement has been my strength, to whom this research work with love is dedicated.

Mehran Ghafouri

April 2018,

Lappeenranta, Finland

TABLE OF CONTENTS

ABSTRACT	2
ACKNOWLEDGEMENTS	3
TABLE OF CONTENTS	4
LIST OF FIGURES	8
LIST OF TABLES	10
LIST OF SYMBOLS AND ABBREVIATIONS	11
1 INTRODUCTION	16
1.1 Motivation for the Investigation.....	18
1.2 Aim of the Thesis	18
1.3 Limitations	19
2 RESIDUAL STRESSES AND DEFORMATIONS	20
2.1 Residual Stresses Classification.....	20
2.2 Welding-induced Stresses	21
2.3 Residual Stresses Measurement Methods	25
2.4 Welding Deformations	26
3 THERMO-METALLURGICAL-MECHANICAL ANALYSES	28
3.1 Computational Welding Mechanics Background	28
3.2 Welding Heat Source	32
3.2.1 Heat Input and Power Density.....	32
3.3 Thermal Analysis	34
3.3.1 Fourier’s Law of Heat Conduction.....	34
3.3.2 Constitutive Heat Conduction Equation.....	35
3.3.3 Initial and Thermal Boundary Conditions.....	36
3.3.3.1 Newton’s Law of Cooling.....	36

3.3.3.2	Law of Heat Transfer by Radiation	37
3.4	Mathematical Modeling of Heat Source	37
3.4.1	Rosenthal's Point Source.....	38
3.4.2	Surface Flux Distribution (Pavelic's Disk Model).....	38
3.4.3	Hemispherical Heat Source Model.....	39
3.4.4	Ellipsoidal Heat Source Model.....	40
3.4.5	Goldak's Double Ellipsoidal Model.....	40
3.5	Metallurgical Aspects of Welding	42
3.5.1	Physical Metallurgy.....	42
3.5.2	Phase Diagram and Solid Phases.....	43
3.5.2.1	α -Ferrite	44
3.5.2.2	Austenite	45
3.5.2.3	Cementite	45
3.5.2.4	δ -Ferrite.....	45
3.5.3	Phase transformation	45
3.5.3.1	Diffusional Transformations.....	46
3.5.3.2	Diffusionless Transformations.....	47
3.5.4	Thermal Cycle and Microstructure Evolution in Welding.....	48
3.6	Mechanical Analysis	50
3.6.1	Equilibrium Equation	50
3.6.2	Thermal Elasto-Plastic Constitutive Equation.....	50
3.6.3	Strain Hardening Models.....	51
3.6.3.1	Isotropic Hardening	51
3.6.3.2	Kinematic Hardening.....	51
4	EXPERIMENTAL SETUP	53
4.1	Welding Procedure	53
4.2	Measurements.....	55

5	FINITE ELEMENT MODELING	57
5.1	Model Geometry and FE Mesh	57
5.2	Material Modeling	59
5.2.1	Material under Investigation	59
5.2.2	Temperature-Dependent Thermo-Physical Properties	60
5.2.2.1	Specific Heat	61
5.2.2.2	Latent Heat	62
5.2.2.3	Thermal Conductivity	64
5.2.2.4	Density	66
5.2.3	Temperature-Dependent Mechanical Properties	66
5.2.3.1	Poisson's Ratio	67
5.2.3.2	Young's Modulus	68
5.2.3.3	Yield Strength	69
5.2.3.4	Thermal Expansion Coefficient	71
5.3	Transient Thermal FE Modeling	72
5.3.1	Modeling of Thermal Load	72
5.3.2	Modeling of Heat Loss	76
5.3.3	"Model Change" Technique	77
5.3.4	Element Type in Thermal Analysis	78
5.4	Mechanical FE Modeling	79
5.4.1	Element Type in Mechanical Analysis	79
5.4.2	Mechanical Boundary Conditions	80
5.4.3	Mechanical Aspect of "Model Change"	80
5.4.4	Strain Decomposition	81
5.4.4.1	Elastic Strain Component	82
5.4.4.2	Plastic Strain Component	82
5.4.4.1	Thermal Strain Component	83

5.4.5	Annealing Effect.....	83
5.5	Solid-State Phase Transformation.....	84
5.5.1	Dilatometric Test.....	84
5.5.2	Phase Transformation kinetics models.....	86
5.5.2.1	Austenitic Transformation Model.....	87
5.5.2.2	Diffusive Transformation Model.....	88
5.5.2.3	Martensitic Transformation Model.....	89
5.5.3	Volume Change Strain	91
5.5.4	Computational SSPT in ABAQUS.....	93
6	RESULTS AND DISCUSSION	94
6.1	Validation of the Thermal Analysis	94
6.2	Visualization of SSPT and prediction of microstructure	102
6.3	Analysis of transverse residual stresses	105
6.4	Analysis of Deformations	107
7	CONCLUSION	110
	REFERENCES.....	112

LIST OF FIGURES

Figure 1. Schematic of the first, second and third order residual stresses (Radaj, 1992, p. 7).....	21
Figure 2. General paradigm of distribution of longitudinal (a) and transverse (b) residual stresses generated in welding (Ueda, et al., 2012, p. 7).....	25
Figure 3. Typical welding-induced deformations: longitudinal shrinkage (a), transverse shrinkage (b), angular distortion (c), twisting or rotational distortion (d), buckling distortion (e) and bending distortion (f) (SSAB, 2016, p. 73).	27
Figure 4. Major couplings in welding modelling problems (Goldak & Akhlaghi, 2005, p. 10).	29
Figure 5. Effects of variation of heat input and power density (Kou, 2003, p. 4).	34
Figure 6. Schematic of Goldak’s double ellipsoidal heat source model.....	40
Figure 7. Schematic of general crystal structures in metals.....	43
Figure 8. Fe-Fe ₃ C phase diagram (Callister, 2000, p. 303).	44
Figure 9. BCT crystal structure which is elongated in c direction (Callister, 2000, p. 335).	48
Figure 10. Different subzones of HAZ (Falkenreck, et al., 2017).	49
Figure 11. Isotropic hardening model (Hansen, 2003, p. 51).	51
Figure 12. Kinematic hardening model (Hansen, 2003, p. 52).	52
Figure 13. Robotized GMAW arm and position of the base plate.....	54
Figure 14. Location of thermocouples on top (a) and bottom (b) surfaces.....	55
Figure 15. Residual stress (a) and distortions (b) measurement paths on top surface.	56
Figure 16. Meshed geometry for FE analysis.	58
Figure 17. Specific heat as a function of temperature calculated by JMatPro.....	62
Figure 18. Temperature-dependent thermal conductivity calculated by JMatPro.	65
Figure 19. Density as a function of temperature calculated by JMatPro.	66
Figure 20. Poisson’s ratio as a function of temperature calculated by JMatPro.....	67
Figure 21. Experimental Young’s modulus of Strenx [®] 960 MC as a function of temperature.	68
Figure 22. Geometry of tensile test specimen (Dimensions in mm).....	69
Figure 23. Experimental Temperature-dependent yield strength of Strenx [®] 960 MC.	71

Figure 24. Prior-austenite grain structure of Strenx [®] 960 MC.	75
Figure 25. Applied boundary conditions in structural analysis.	80
Figure 26. Dilatometric test Apparatus (a), temperature measurement of a heated sample (b).	85
Figure 27. Schematic of heating and cooling diagram used in dilatometric tests.....	86
Figure 28. Scanning electron micrograph of Strenx [®] 960 MC.....	87
Figure 29. Predicted temperature field and thermal contours in symmetry plane.	94
Figure 30. Boundaries of the weld pool and welding isotherms on top surface from simulation versus experiment.	95
Figure 31. Predicted and measured temperature histories: locations T ₁ and T ₃ (a), T ₂ and T ₄ (b) on top surface.	96
Figure 32. Predicted and measured temperature histories: locations B ₁ and B ₃ (a), B ₂ (b) on bottom surface.....	97
Figure 33. Predicted versus experimental temperature histories at location T ₁	99
Figure 34. Predicted versus experimental temperature histories at location T ₄	99
Figure 35. Simulated versus measured temperature histories at location B ₁	100
Figure 36. Simulated versus measured temperature histories at location B ₂	101
Figure 37. Predicted fractions of austenite (a), bainite (b) and martensite (c) at t = 25s.....	103
Figure 38. Volume fractions of untransformed base metal (a), formed bainite (b) and martensite (c).	104
Figure 39. SEM micrographs of HAZ, Prior austenite grain boundaries (a), a mixture of bainite and martensite (b).	105
Figure 40. Transverse residual stresses from experimental measurements and FE simulations.....	106
Figure 41. Displacement contours (U ₃) after cooling and relaxation. (Dimensions in m)	107
Figure 42. Angular distortion along the path1.....	108
Figure 43. Angular distortion along the path2.....	108
Figure 44. Simulated versus measured bending deformation.....	109

LIST OF TABLES

<i>Table 1. Commonly considered couplings in welding simulations (Goldak & Akhlaghi, 2005, p. 10; Lindgren, 2001a; Hansen, 2003, p. 13).....</i>	29
<i>Table 2. Recommended heat source efficiency values for different processes (Grong, 1997, p. 27).</i>	33
<i>Table 3. Employed welding parameters.</i>	54
<i>Table 4. Chemical composition of Strenx[®]960 MC (wt. %).</i>	60
<i>Table 5. Mechanical properties of Böhler Union X96 (Björk, et al., 2012).</i>	60
<i>Table 6. Calculated values for latent heat of fusion, solidus and liquid temperatures.</i>	63
<i>Table 7. Goldak's parameters in FE model.....</i>	74
<i>Table 8. Ms and Bs temperatures based on empirical formula and experiment.</i>	90
<i>Table 9. Thermal expansion coefficients and full volumetric change strains of Strenx[®]960 MC.</i>	92

LIST OF SYMBOLS AND ABBREVIATIONS

A	Elongation
A_1	Lower critical temperature
A_3	Upper critical temperature
a	Semi-axis in x direction
B_f	Bainite finish temperature
B_s	Bainite start temperature
b	Semi-axis in y direction
C	Distribution width coefficient
C_{ijkl}	Stiffness tensor
C_{th}	Thermal stiffness matrix
c	Semi-axis of the ellipsoid in z direction
c_L	Specific heat in liquid state
c_S	Specific heat in solid state
c_f	Semi-axis in the front half of double-ellipsoid
c_l	Characteristic radius of heat flux distribution
c_p	Specific heat
c_r	Semi-axis in the rear half of double-ellipsoid
$[D^e]$	Elastic stiffness matrix
$[D^p]$	Plastic stiffness matrix
F_b	Body force vector
f	Yield function
f_a	Austenite fraction during heating
f_b	Bainite fraction transformed during cooling
f_f	Fraction of heat deposited in the front half of double-ellipsoid
f_i	Fraction of phase i
f_m	Martensite fraction transformed during cooling
f_r	Fraction of heat deposited in the rear half of double-ellipsoid
$f_b^{\%}$	Final fraction of bainite formed during cooling
$f_m^{\%}$	Final fraction of martensite formed during cooling

H	Specific enthalpy
H_L	Latent heat of fusion
h	Temperature-dependent heat transfer coefficient
h_c	Convective heat transfer coefficient
h_r	Radiative heat transfer coefficient
I	Welding electric current
$\vec{i}, \vec{j}, \vec{k}$	Unit vectors pertinent to x, y, z directions
k	Thermal conductivity
k_a	Factor in Machniekno kinetics
k_m	Characterization factor in Koistinen-Marburger kinetics
M_f	Martensite finish temperature
M_s	Martensite start temperature
Q_e	Effective or net heat input per unit time
Q_g	Gross or nominal heat input per unit time
Q_w	Net heat input per unit length
\dot{Q}_v	Internal volumetric heat generation rate
q'	Heat flow or heat flux density per unit area
q'_c	Convective heat flow density per unit area
q'_r	Radiative heat flow density per unit area
\vec{q}'	Heat flow or heat flux density vector
q''	Heat flow density per unit volume
s_{ij}	Deviatoric stress tensor
T	Current temperature
T_L	Liquidus temperature
T_0	Ambient temperature
T_S	Solidus temperature
T_{max}	Maximum temperature
t	Time
$t_{8/5}$	Cooling time in the range 800-500 °C
U	Arc voltage
V	Initial volume
v	Welding travel speed

$v_{8/5}$	Cooling rate in the range 800-500 °C
x, y, z	Cartesian coordinates
α	Linear thermal expansion coefficient
α_a	Austenite thermal expansion coefficient
α_b	Bainite thermal expansion coefficient
α_i	Linear thermal expansion coefficient Phase i
α_m	Martensite thermal expansion coefficient
α^d	Thermal diffusivity
δ_{ij}	Knocker delta
ΔT	Temperature increment
ΔV	Volume change
ε	Engineering strain
$\tilde{\varepsilon}$	True strain
ε_{ij}	Strain tensor
ε_x	Axial or longitudinal strain
ε_y	Lateral or transverse strain
$\dot{\varepsilon}^c$	Creep Strain increment
$\dot{\varepsilon}^e$	Elastic strain increment
$\dot{\varepsilon}^p$	Plastic strain increment
$\dot{\varepsilon}^{th}$	Thermal strain increment
$\dot{\varepsilon}^{total}$	Total strain increment
$\dot{\varepsilon}^{trp}$	Transformation plasticity strain increment
$\dot{\varepsilon}^{vp}$	Viscoplastic strain increment
$\dot{\varepsilon}^{\Delta V}$	Volumetric change strain increment
$\varepsilon_i^{\Delta V^*}$	Full volumetric change strain for phase i
$\varepsilon_a^{\Delta V^*}$	Full volumetric change strain for austenite during heating
$\varepsilon_b^{\Delta V^*}$	Full volumetric change strain for bainite during cooling
$\varepsilon_m^{\Delta V^*}$	Full volumetric change strain for martensite during cooling
ε^*	Emissivity
η	Heat source efficiency coefficient
ρ	Density
λ	Plastic flow factor

ν	Poisson's ratio
σ	Engineering stress
$\tilde{\sigma}$	True stress
$\bar{\sigma}$	Effective Von Misses stress
σ^*	Stefan-Boltzmann constant
$\sigma^I, \sigma^{II}, \sigma^{III}$	First, second and third order residual stresses
σ_{ij}	Cauchy Stress tensor
σ_y	Yield strength or yield limit
σ_u	Ultimate tensile strength
τ	Lag factor
ξ	Coordinate of the moving heat source in welding direction
∇	Divergence Operator
∇T	Temperature gradient
AHSS	Advanced High-Strength Steel
ASTM	American Society for Testing and Materials
AWS	American Welding Society
BCC	Body-Centered Cubic
BCT	Body-Centered Tetragonal
CCT	Continuous Cooling Transformation
CEV	Carbon Equivalent Value
CGHAZ	Coarse-Grained Heat-Affected Zone
CWM	Computational Welding Mechanics
EBW	Electron Beam Welding
FCAW	Flux-Cored Arc Welding
FCC	Face-Centered Cubic
FE	Finite Element
FEM	Finite Element Method
FGHAZ	Fine-Grained Heat-Affected Zone
FZ	Fusion Zone
GMAW	Gas Metal Arc Welding
GTAW	Gas Tungsten Arc Welding
ICHAZ	Inter-Critical Heat-Affected Zone
IGSCC	Intergranular Stress Corrosion Cracking

HAZ	Heat-Affected Zone
HCP	Hexagonal Close-Packed
HSLA	High Strength Low Alloy
LPHSW	Last Pass Heat Sink Welding
LSP	Laser Shock Processing
ND	Normal Direction
PWHT	Post-weld Heat Treatment
RD	Rolling Direction
SCHAZ	Sub-Critical Heat-Affected Zone
SEM	Scanning Electron Microscopy
SSPT	Solid-State Phase Transformation
TD	Transverse Direction
TMM	Thermo-Metallurgical-Mechanical
UHSS	Ultra-High Strength Steel
UIT	Ultrasonic Impact Treatment
XRD	X-Ray Diffraction

1 INTRODUCTION

Joining process is one of the frequently-employed processes in a wide spectrum of industries whose objective is to unify different materials in either temporary or perpetual manner. Among the joining processes, welding is one the most efficient and economic methods which is extensively used to make permanent joints in a diverse domain of industry applications ranging from small components in electronic companies to mega-structures in offshore and ship-building industries. Welding as is defined by American Welding Society (AWS) is “*a localized coalescence of metals or non-metals produced by either heating of the materials to a suitable temperature with or without the application of pressure, or by the application of pressure alone, with or without the use of filler metal*” (Anca, et al., 2011).

In case of metals, among the welding processes which are increasingly developing, except for a few, most welding processes operate on exerting a tremendous amount of heat into the base material which causes the atoms of the two pieces subject to welding become sufficiently close so that establishment of an atomic interaction and accordingly, joining becomes feasible. (Kielhorn, et al., 2001). This type of welding which is so called fusion welding, can be split into subcategories based on the external heat source type which is exploited to cause melting. Amidst the welding processes falling into this subcategory, arc welding processes are well-known and the most commonly used processes in different variety of industrial applications.

The significant heat which is transported into the liquid pool and consequent cooling, have notable effects on mechanical properties and microstructural evolution of material. Transient thermal field causes thermal strain and gives rise to residual stresses and change in the microstructure, which itself controls mechanical and thermal properties of the material and as a result, plastic deformation and distortions occur (Goldak, et al., 1986). Exacerbation of several calamitous phenomena which are banes for structural integrity and service performance of components, are directly addressed to appearance of detrimental residual stresses which is a matter of practical concern. Therefore, well-functioning methodologies and efficient models are required to pinpoint and analyze the residual stresses originated from welding thermal cycles.

On the other hand, necessary need of growing technology for light-weight but high-performance materials has resulted in advent and development of high strength steels during the last decades. Aside from exhibiting high strength-to-weight ratio, advanced high-strength steels (AHSS) have a magnificent combination of weldability and high energy absorption capacity making them suitable for usage in numerous manufacturing industries such as ship-building, heavy-lifting and automotive industries as well as offshore construction and industrial equipment manufacturing. (Shome & Tumuluru, 2015, pp. 1-8; Guo, et al., 2015; Guo, et al., 2017)

Considering the inevitability of utilizing welding technique in fabrication of components and in particular, widespread use of conventional arc welding processes as a joining method for AHSS, dramatic ramifications of such methods transferring high heat input into the material should be taken into account. Softening in heat-affected zone (HAZ) (Biro, et al., 2010; Skriko, et al., 2017) and reduction in strength (Azhari, et al., 2015) of ultra-high strength steels (UHSS) subject to elevated temperatures, are of considerable importance. Moreover, residual stresses as a consequence of non-uniform heating and cooling of welding become a major concern due to their effects on strength and fatigue behavior of welded joints under cyclic loading. Thus, realistic models to accurately predict and evaluate residual stresses and their implications on performance of welded structures constructed from high strength steels, become imperative in order to increase the efficiency of their load-bearing capacity and assure the safe application of them (Li, et al., 2015).

Finite element method (FEM) as a numerical method has proven its ability to give solution for a large number of linear and non-linear mathematical and engineering problems. Exponential development of computers and their increased computational capacity along with enhancement in numerical methods in the field of heat transfer problems and particularly welding, sparked computational welding mechanics (CWM) whose aim is to analyze the temperature field, stress and strains along with microstructure evolution in welded connections (Goldak & Akhlaghi, 2005, p. 2). Along the lines of welding residual stresses and their assessment, from size point of view, especially in case of large-scale welded structures, dimensions render the direct measurement methods either impracticable or cost-ineffective as it pertains to destructive measurement techniques. Simulation methods

have been developed strikingly during the last decades which facilitate the modeling of real welded structures with regards to analysis the residual stresses.

1.1 Motivation for the Investigation

Increased employment of UHSSs in a variety of industrial applications due to their favorable potentials was pointed out. Differences in manufacturing processes cause unequivocal variations in their microstructures and mechanical properties. Arc welding processes with their inherent high heat input are frequently applied as a joining method to UHSS materials. Providing safety to components and structures from UHSS they are made, in addition to exploit the maximum efficiency of their strength capacity, entail research to assess the effect of detrimental phenomena on their performance and service life. Having a sufficient understanding of welding-induced residual stresses and deformations formed by elevated temperature of welding and their effects on strength and fatigue behavior of materials under dynamic stresses, is indubitable driving force for this research.

1.2 Aim of the Thesis

It is aimed at developing a computational procedure to evaluate welding-induced residual stresses and imposed deformation of Strenx[®]960 MC UHSS material by modeling the single pass bead on plate during Gas metal arc welding (GMAW) process using a sequentially-coupled thermo-metallurgical-mechanical analysis in this thesis.

To reach this aim, an effort is put into defining several objectives to be followed:

- A meticulous attention is paid to precisely model the heat source and calibrate pertinent parameters to be able to perform a thermal analysis reflecting the temperature field and weld pool dimensions as close as possible to the experimentally measured ones.

- Study the diffusive and displacive phase transformations phenomena and developing the transformation mathematical model which applies the existing relations based on the performed dilatometric tests on the specimens made from the material under investigation. The phase transformation model is then involved in numerical simulation to study the effect of bainitic and martensitic transformations on evolution of residual stresses and deformations.

- Obtaining temperature-dependent yield strength and Young's modulus of Strenx[®]960 MC via conducting hot tensile tests at different temperatures to ensure accuracy of mechanical analysis.

1.3 Limitations

- This research is only focused on developing a computational model for 8 mm thickness Strenx[®]960 MC plate material in a single pass bead on plate by GMAW process.
- Temperature-dependent yield strength of base material is determined up to 1200 °C based on the capacity of the test machine. Mechanical properties of filler material is assumed to be identical to the parent material owing to the difficulty of obtaining those properties of filler material, especially at high temperatures.
- In computational model of phase transformation, only strains due to volume change are accounted for and transformation-induced plasticity is ignored.
- In measurement of residual stresses, inasmuch as X-ray diffraction (XRD) method is applied, solely surface transverse residual stresses are measured and through thickness stresses are neglected.

2 RESIDUAL STRESSES AND DEFORMATIONS

Residual Stresses are defined as internal stresses existing in components prior to imposing external loads which stand in equilibrium with themselves. They are titled in such case as constraint stresses that might be superimposed to reaction stresses originating from applying self-equilibrating support forces to compose total residual stresses. Stress state in a load-carrying component or structure, however, comprises external stresses and total residual stresses. These stresses are the result of inhomogeneous permanent elastic or plastic deformation in regions of material in which incongruence of deformation's state befall. (Macherauch, 1987, p. 1; Radaj, 1992, p. 5)

A wide range of residual stress states emanate from a variety of manufacturing processes and treatment technologies that might greatly affect performance and structural integrity of an engineering component or structure. Hence, it is of particular importance for designers and engineers to have a profound fathom of the origins, measurement methods, ramifications, assessment and mitigation of harmful impacts of such stresses. Residual stresses originated from welding, machining, forging and practically all fabricating technologies might have either deleterious subsequences or desirable effects contingent upon their magnitude, distribution and direction as well as their sign (Macherauch, 1987, p. 1; Barsoum & Barsoum, 2009).

2.1 Residual Stresses Classification

Residual stresses can be classified into three categories based on the scale at which they emerge, namely first order, second order and third order residual stresses. First order or first kind, σ^I , which are also known as macroscopic stresses, are averaged stresses being rather homogenous which denotes having the same direction and magnitude over macroscopic or large areas, i.e. several material's grains or crystallites with approximate size of 1 mm.

Second order or microscopic residual stresses, σ^{II} , act between adjacent grains. They extend over microscopic areas within the size of a grain or fraction of a grain. They are approximately in size of 0.01 – 1 mm. Ultimately, microscopic or ultra-microscopic stresses which are inhomogeneous stresses functioning within submicroscopic or in other

words atomic scales, e.g. residual stresses around a single dislocation, are termed third order stresses, σ^{III} with average size of $10^{-2} - 10^{-6} \text{ mm}$. (Macherauch, 1987, pp. 4-10; Radaj, 1992, pp. 5-6) Classification of the first, second and third order stresses acting in Y direction, is depicted in the figure 1.

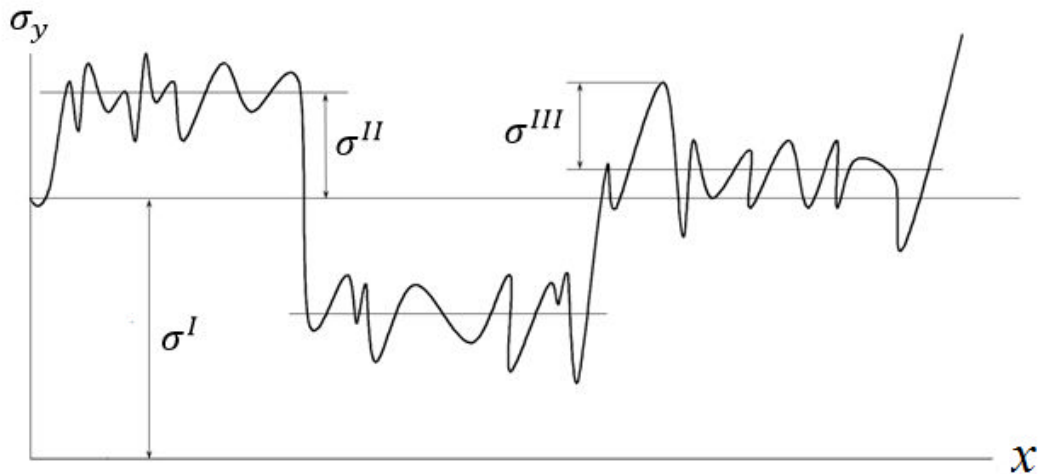


Figure 1. Schematic of the first, second and third order residual stresses (Radaj, 1992, p. 7).

It is worthy of mention that in engineering applications, first order stresses are center of attention concerning the effect of locked-in stresses on deformation. This sort of stress with different scale and distribution in material, originates from various manufacturing processes. (Pilipenko, 2001, pp. 29-30)

2.2 Welding-induced Stresses

Stresses and deformations introduced by welding processes are one of the frequently-studied subjects and major concerns in welded structures under dynamic loading or adverse service conditions (Ueda, et al., 2012, p. 1; Heinze, et al., 2011; Tsai & Kim, 2005, p. 3). During welding, Material expands as a result of localized heating which causes a sharp thermal gradient and non-uniform thermal expansion in the weld area. Thermal stresses arise due to the restriction of heat expansion by surrounding colder zone. Since yield strength is temperature-dependent and strongly decreases at elevated temperatures, any point of weld region in which thermal stresses exceed yield limit, σ_y , plastically deforms in an inhomogeneous manner. As a consequent of thermal cycle imposing rapid heating and ensuing non-uniform cooling, tensile residual stresses in a small area develop while in the adjacent region, compressive stresses rise. On condition that phase transformation which

occurs during cooling cycle accompanied by volume expansion, befalls in lower temperature where yield strength is high enough, compressive residual stresses in weld area and tensile residual stresses in surrounding region are observable. (Radaj, 1992, p. 8) It is also stated by Radaj (1992, p. 8) that where thermal stresses prevail, tensile residual stresses exist whereas, compressive stresses occur where phase transformation stress is dominant.

Exacerbation the service performance or accelerating a diverse range of degradation mechanisms of components are attributed to the presence of residual stresses. Contrary to compressive residual stresses, in most cases, tensile residual stresses are considered detrimental being principally in dimensions of material's yield strength. Tensile residual stresses are expressed by several researchers to be influential in shorten the fatigue life of welded connections by expediting fatigue crack growth rate (Barsoum & Barsoum, 2009; Cheng, et al., 2003; Liljedahla, et al., 2009; Kang, et al., 2008; Nguyen & Wahab, 1998; Webster & Ezeilo, 2001). Lee & Koh (2002) investigated the effect of residual stresses on fatigue life of internally-loaded thick-walled pressure vessel and reported improved fatigue life due to presence of tangential compressive residual stress at the inside surface of the pressure vessel. In another research, decrease in tensile residual stress was considered to enhance the fatigue crack initiation life of butt-welded joints (Teng & Chang, 2004). Adverse influence of welding-induced residual stresses on brittle fracture was previously studied and results were presented elsewhere (Moshayedi & Sattari-Far, 2015). Additionally, tensile residual stresses are responsible for decreasing the buckling strength and promotion the susceptibility to intergranular stress corrosion cracking (IGSCC) and hydrogen-induced cold cracking (Deng, 2009; Burst & Kim, 2005; Mochizuki, et al., 2002; Ueda, et al., 2012, p. 55; Mochizuki, 2007).

Considering the damaging ramifications of welding residual stresses on structural integrity and service life of welded connections, it is of paramount importance to take countermeasures in order to negate or alleviate the hazardous consequences of those stresses.

The prominence of attenuating unfavorable residual stresses has led to emergence of different stress relieving methods capable of eliminating detrimental residual stresses provided that correct *modus operandi* is applied being hitherto investigated by a large number of researchers.

Post-weld heat treatment (PWHT) is well-known for pronounced contribution in welding residual stress relief and one of the highly employed techniques to control residual stresses. Positive effects of this process in enhancement of toughness and significant reduction of residual stresses of welded structures was reported by Olabi & Hashmi (1995). Conversion of tensile residual stress to compressive residual stress at the root of welds subject to a treatment process named last pass heat sink welding (LPHSW) was demonstrated by other authors (Fricke, et al., 2001).

Pulsed magnetic technique was used to reduce residual stresses in steel specimens and a fall of 4-7% and 8-13% in the surface stress value depending on the initial stress level was reported (Klamecki, 2003). Ultrasonic impact treatment (UIT) is another post treatment method taking advantages of exerting mechanical impacts in conjunction with ultrasonic pulses into weld regions. Utilization of this method in removing high tensile residual stresses of a T-welded joint was studied by Cheng et al. (2003) and results of improvement the fatigue life of non-load carrying cruciform welded joints using the same treatment was recently published elsewhere (Yuan & Sumi, 2016).

Employment of shot peening as a residual stress mitigation technique was previously investigated (Torres & Voorwald, 2002; Cheng, et al., 2003). It is, however, mentioned that increasing the fatigue strength of material is not essentially a function of shot peening intensity and thus, determining the best shot peening condition might be quite complicated (Torres & Voorwald, 2002). In addition to mentioned operations, reduction of residual stresses using random vibration during welding (Aoki, et al., 2005), Laser Shock Processing (LSP) (Dorman, et al., 2012) and explosive treatment (Zhang, et al., 2005) were also proposed. The reader is referred to (Burst & Kim, 2005; Radaj, 1992) for more information concerning mechanism and various mitigation methods for residual stresses.

Welding residual stresses might be categorized observed from different standpoints. They might be generated temporarily during welding or can be permanent after complete cooling and temperature equalization. As it pertains to directionality of welding residual stresses, they can lie on longitudinal and transverse directions.

Welding longitudinal residual stresses are resulted from longitudinal contraction mechanism of weld seam. Tensile longitudinal residual stresses exist in a narrow region near the weld seam whose maximum magnitudes might be higher or at yield limit dropping off further away from the weld line and then relax down in the neighboring area. Compressive stresses with a lower value exist in the surrounding area whose magnitudes fall as their distance to weld line grows. (Radaj, 1992, p. 9; Pilipenko, 2001, p. 38) It is expressed by Hansen (2003, p. 19) that residual stresses have generally a mathematical sign opposing to the transient stress field sign during welding. In other words, during welding, residual stresses close to the weld seam are compressive and tensile in the adjacent area and vice versa after completion of cooling cycle. Residual stress distribution in the weld, under the influence of chemical composition of base material and weld metal and cooling rate might differ remarkably (Pilipenko, 2001, p. 38).

In the plane of plate, welding transverse residual stresses are generated according to weld line's transverse contraction mechanism specifically when the plate is constrained. During the moving of heat source, barring very slow welding speed, material in the center of weld region is the last place to be cooled down and material far from weld seam towards edges, retrieve its strength prior to the center of weld. In free boundary condition, compressive residual stresses will develop near the edges to equilibrate the tensile stresses rising in the center of weld area. In this situation transverse residual stresses are not large in magnitude. (Hansen, 2003, p. 19) Longitudinal and transverse residual stresses are schematically depicted in the figure 2. It is needless to mention that positive sign denotes tensile stresses and compressive stresses are shown with a negative sign.

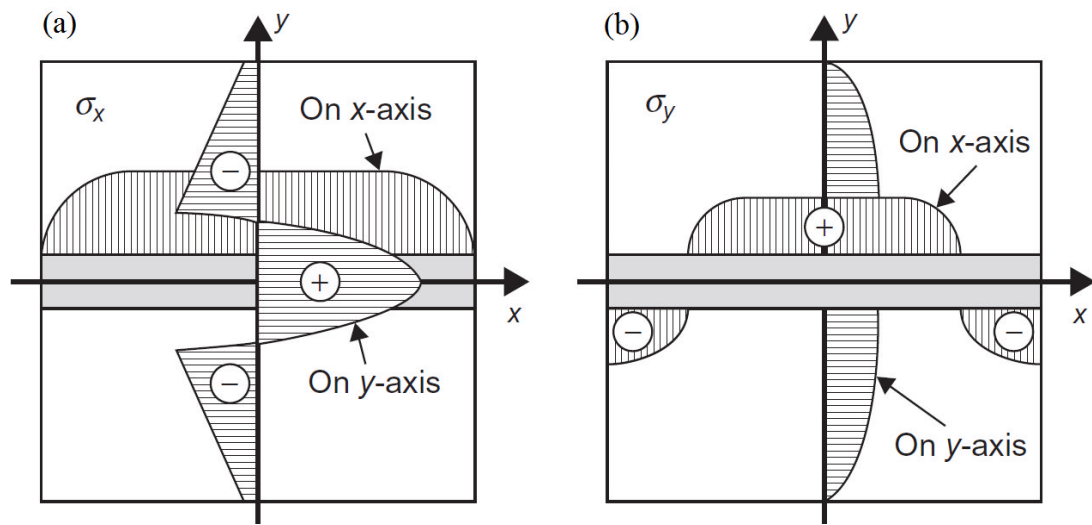


Figure 2. General paradigm of distribution of longitudinal (a) and transverse (b) residual stresses generated in welding (Ueda, et al., 2012, p. 7).

2.3 Residual Stresses Measurement Methods

In course of time, different measuring procedures including both destructive and non-destructive methods to determine various kinds of residual stresses have been developed.

Mechanical methods are destructive and in some cases simple to employ through which only 1st order stresses are determined. This method is therefore incapable for components in use putting a limitation on their applications in practice. One of the most commonly used mechanical methods which is classified as a semi-destructive method consists of drilling a hole and measuring released macroscopic strains and accordingly, distribution, sign and magnitude of residual stresses can be determined. This technique was utilized in the past by some investigators (Min, et al., 2006; Mirzaee-Sisan, et al., 2007).

The neutron-diffraction method as a non-destructive measuring process, allows analysis of the 1st and the 2nd order residual stresses on the surface as well as interior layers of the materials. It is extensively used by researchers to measure welding residual stresses (Pearce, et al., 2008; James, et al., 2006; Price, et al., 2008; Cheng, et al., 2003).

X-ray diffraction (XRD) technique analogous to neutron diffraction method is a non-destructive process to analyze the 1st and the 2nd order stresses by measuring lattice strains. Both methods have the potential to measure strains through observation the change in the

interplanar spacing of the crystal lattice. The difference between the two methods is expressed in terms of penetration depth of the scattered x-rays and neutrons. X-ray wave lengths compared to neutrons have smaller penetration depths which makes XRD procedure suitable for surface residual stresses measurement.

Further enhanced measuring methods are ultrasonic and magnetostriction methods which have the feasibility to determine the first, second and third order residual stresses. A comprehensive description of the residual stresses measurement techniques and their features can be found in the works of Macherauch (1987) and Radaj (1992).

2.4 Welding Deformations

As mentioned earlier, during welding due to high temperatures, non-linear thermal distribution and resulting melting followed by a non-uniform cooling process, welding-induced stresses together with plastic straining occur in base and weld metal after reaching the ambient temperature. These inhomogeneous plastic strains leading to permanent deformation in welded structures, also termed as welding-induced distortions. Welding deformations might seriously impair fabrication and applicability of the manufactured components or structures. Therefore, proper measures should be taken to minimize or eliminate both undesirable residual stresses and welding deformations. (Chao, 2005, p. 209)

In contrast to welding residual stresses which are consequential phenomena in jeopardizing strength and design reliability, welding deformations are mostly considered as an adverse aspect in manufacturing process. It should be noticed that high geometrical constraints result in low deformations and high residual stresses whereas, in unrestrained deformations, residual stresses are low. (Radaj, 1992, pp. 1-2; Chao, 2005, p. 209)

Welding deformations which are also entitled as shrinkage, distortion or warping can be classified into six groups. Longitudinal shrinkage, which is longitudinal shortening in weld direction. Transverse shrinkage occur perpendicular to weld seam and causes contraction in transverse direction. Angular shrinkage whose distortion mode is out-of-plane, occurs due to non-uniform temperature field through thickness of the plate. This sort of distortion can be found particularly in multi-pass welding of single-side grooved plates. Twisting or rotational distortion has a root in thermal expansion or contraction and similar to longitudinal

and transverse shrinkages, happen in plane of the plate. Buckling distortion whose mode is out-of-plane, is resulted from compressive stresses mostly in case of thin plates. Bending distortion is observable perpendicular to the plate in weld line's plane. (Goldak & Akhlaghi, 2005, pp. 153-154) Figure 3, schematically demonstrates different welding-induced distortions.

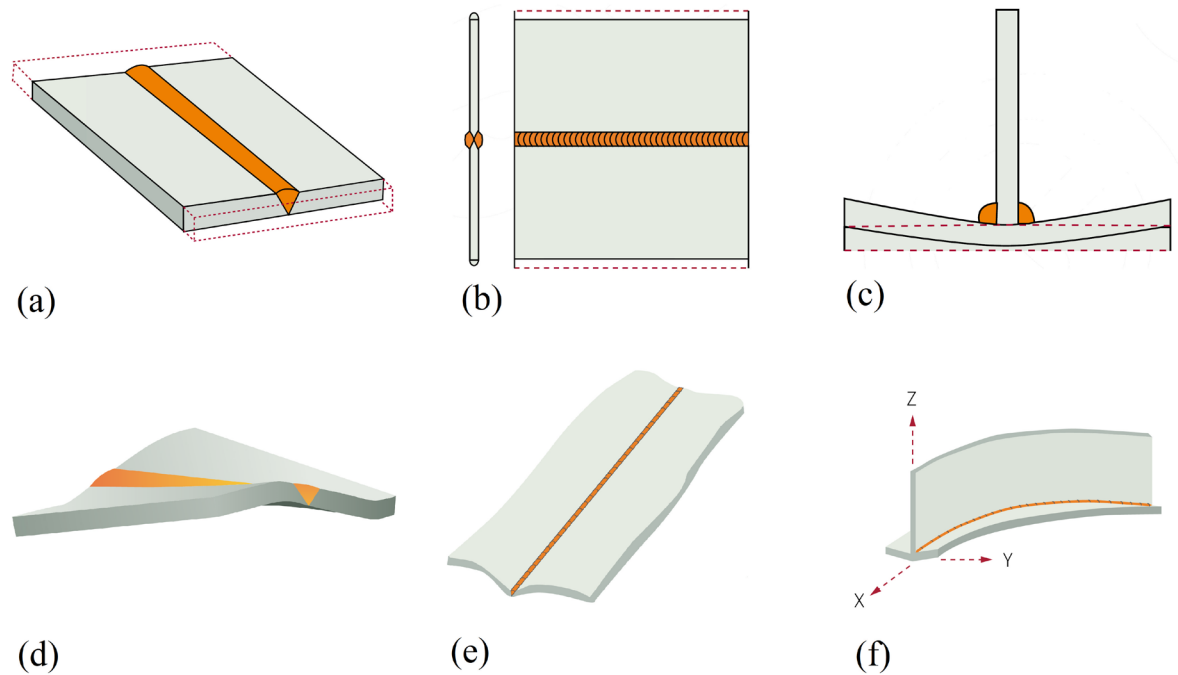


Figure 3. Typical welding-induced deformations: longitudinal shrinkage (a), transverse shrinkage (b), angular distortion (c), twisting or rotational distortion (d), buckling distortion (e) and bending distortion (f) (SSAB, 2016, p. 73).

3 THERMO-METALLURGICAL-MECHANICAL ANALYSES

In welding simulation problems, in order to determine resulted residual stresses and deformations, a series of analyses are to be performed. To establish a well-developed and efficient finite element (FE) model, a number of couplings are principally deemed between those analyses namely thermal, metallurgical and mechanical analyses. It is worthy to mention the terms modelling and simulation, are interchangeably used in the current study.

3.1 Computational Welding Mechanics Background

Establishment of approaches and models being able to correctly design welding processes and control their important parameters is the main purpose of CWM in order to gain proper service performance for mechanical components or structures (Lindgren, 2007, p. 1). This multidisciplinary research field calls for necessary collaboration from different branches of science such as welding metallurgy, material science, heat transfer and fluid flow, mechanical behavior of metals and computational sciences. Combined with fatigue and fracture mechanics, CWM can be extended to include prediction of failure phenomena such as cracking which are relevant to the thermal and strain history of the material. Examples of the latter can be found in researches by Barsoum & Barsoum (2009) and Danis et al. (2010).

Since welding processes comprise different phenomena which have strong interactions, welding simulation can be considered as a coupled problem having been previously discussed by some authors (Goldak & Akhlaghi, 2005; Lindgren, 2001a; Radaj, 1992). These couplings, nevertheless, are not of equal prominence and some of which might be neglected contingent upon the welding process (Hansen, 2003, p. 13). Major couplings in modelling of welding are described in the figure 4.

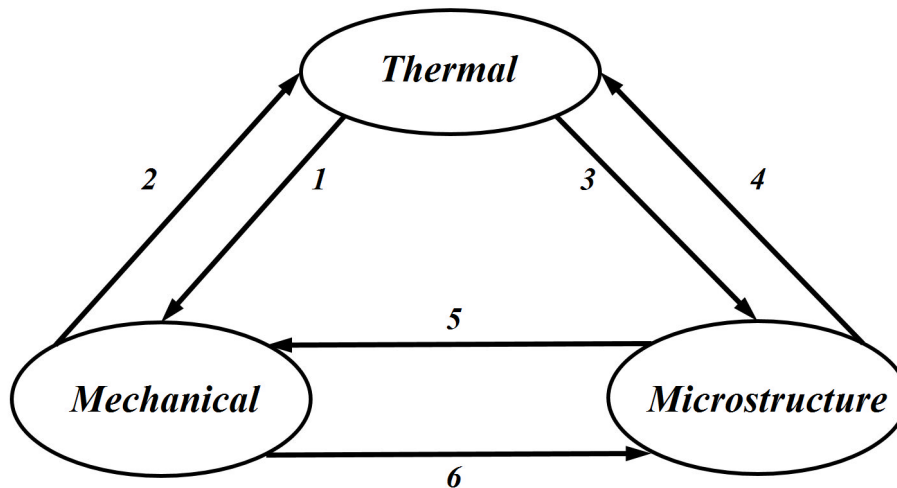


Figure 4. Major couplings in welding modelling problems (Goldak & Akhlaghi, 2005, p. 10).

Explanations corresponding to the couplings depicted in the figure 4, are summarized in the table 1.

Table 1. Commonly considered couplings in welding simulations (Goldak & Akhlaghi, 2005, p. 10; Lindgren, 2001a; Hansen, 2003, p. 13).

<i>Coupling</i>	<i>Explanation</i>
<i>1</i>	<i>Temperature field affects mechanical deformations through thermal expansion</i>
<i>2</i>	<i>Strain rate generates heat which affects thermal boundary conditions</i>
<i>3</i>	<i>Evolution of microstructure depends on temperature history</i>
<i>4</i>	<i>Latent heats during transformations as well as changes in material properties (thermal conductivity and specific heat) owing to phase transformations impacts temperature changes</i>
<i>5</i>	<i>Volume changes owing to phase transformations as well as elastic and plastic behavior depend on microstructure of the material</i>
<i>6</i>	<i>Material straining causes microstructure evolution</i>

Amidst the abovementioned couplings which are taken into account in simulation of welding processes, the couplings number 1, 3 and 5 are of more importance. It is fathomable that microstructure and thermal stress are largely affected by temperature while the effects of microstructure evolution and mechanical response on transient temperature field is not dominant. Most welding simulations involve a thermal analysis followed by a mechanical analysis which is called uncoupled or sequentially-coupled thermo-mechanical simulation and neglects the effect of mechanical response on the temperature. Application of uncoupled or sequentially-coupled thermo-mechanical models were reported in different studies. Deng & Murakawa (2006a) applied such analysis in gas tungsten arc welding (GTAW) of circumferentially butt-welded pipes made from SUS304. A similar thermo-mechanical analysis was used by Yaghi et al. (2005) to investigate temperature history and residual stresses in multi-pass butt welding of thin and thick-walled P91 steel pipes. In a study on Flux-cored arc welding (FCAW) of T-fillet joints made up of shipbuilding steel SM400A, based on the inherent strain theory, a sequentially-coupled formulation was developed to obtain inherent deformations based on which, welding distortion for large welded structures was calculated using an elastic FEM (Deng, et al., 2007). Residual stresses and angular distortion of single pass T-fillet welded joints from three different steels in GMAW process using an uncoupled formulation studied and results reported elsewhere (Bhatti, et al., 2015). With regards to bead on plate welding simulation, Shan et al. (2009) performed a sequentially-coupled thermo-mechanical analysis to investigate thermal history and residual stress field in single weld bead on plate of AISI 316L austenitic stainless steel material.

It is also feasible to solve a system of coupled non-linear equations of temperature and displacement simultaneously. This approach takes also into consideration the effect of thermal stress on temperature field and is known as fully-coupled method. Since this interaction is weak, mentioned approach is not commonly practiced in welding modelling due to increased complexity of solving equations and subsequently a large computational time. Application of a fully-coupled thermo-mechanical approach in order to simulate circumferentially butt-welded stainless steel pipes and double-pass welding T-fillet joints built from ship-building steel SM400A in GTAW and GMAW processes, respectively, along with simulation of shape metal deposition process is reported in a research by Chiumenti et al. (2010).

Provided that simulation includes metallurgical modelling along with thermal and structural (mechanical) analysis, a thermo-metallurgical-mechanical (TMM) model is then concerned. In this context, over the past two decades, numerous researches have been conducted to evaluate temperature field and residual stresses as well as displacement history. Prediction of residual stresses in single-pass as well as multi-pass welding of butt-welded pipes made up of different steel types adopting sequentially-coupled TMM finite element simulation has been verified in several researches (Lee & Chang, 2011; Deng & Murakawa, 2006b; Deng & Murakawa, 2008; Yaghi, et al., 2008).

In a study to investigate the effect of solid-state phase transformation (SSPT) on residual stress and deformation history of butt-welded joints in low and medium carbon steels plates, Deng (2009) developed a sequentially-coupled TMM model and reported that residual stresses and distortion of low carbon steel is not significantly affected by SSPT, whereas martensitic transformation has influential effects of residual stresses and distortion of medium carbon steels and hence, it is of notable importance to take into consideration SSPT for medium carbon steels. Several studies adopted TMM simulation incorporating SSPT for different joint types, fusion welding processes and different materials ranging from various types of steels (Leblond, et al., 1986a; Leblond, et al., 1986b; Lee & Chang, 2009; Piekarska, et al., 2012; Mi, et al., 2016) to nickel-based superalloy Inconel 738 (Danis, et al., 2010) and titanium alloy Ti-6Al-4V (Ahn, et al., 2017) and results were published previously.

Accuracy of the simulation, efficiency of the model and computational costs, are highly important issues in CWM. It is desirable to increase the computation efficiency without precision to be sacrificed. It is then needed to have an evaluation of the acceptable degree of accuracy. Categorizing the accuracy in different levels, Lindgren (2007, p. 167) relates the choice of selection to scope of the analysis. In the direction of increasing the level of precision, reduced accuracy, basic, standard, accurate and very accurate models are then defined. In between, adopting a simulation strategy which considers retaining major perspectives of the problem while reducing or eliminating dispensable features or less important characteristics until the boundaries of the favorable accuracy is met, can be named the key feature to keep equilibrium between required accuracy and affordable computational costs.

In the context of welding simulation, special attention should be paid to different modelling considerations with various degrees of importance, among which, heat source modelling is specifically concerned in CWM while geometrical modelling choice, material modelling and discretization are typical for general applications (Lindgren, 2007, p. 119). The eager reader is referred to a series of interesting reviews by Lindgren (2001a, 2001b, 2001c and 2006) to have a better understanding of modeling aspects, concerns and considerations involved in CWM. Along with the mentioned sources, books by Goldak & Akhlaghi (2005), Radaj (1992) and Lindgren (2007) are highly recommended to obtain a profound insight and comprehensive knowledge along the lines of CWM and its background during the last two decades.

3.2 Welding Heat Source

In order to form the weld pool in fusion welding processes, locally concentrated and time-pertinent heat is essential owing to the fact that metallic materials are heat-diffuser leading to existence of a transient and inhomogeneous temperature distribution during the welding process. High temperature of the weld pool which might reach the evaporation temperature of the base metal causes fusion of base and filler materials and consequent solidification and recrystallization result in microstructural changes affecting residual stresses and welding deformations. It is, then, a matter of prominence to have a sufficient understating of the welding heat source characteristics.

3.2.1 Heat Input and Power Density

Required energy in welding processes are provided through different sources acting either in continuous or momentary manner (Radaj, 1992, p. 21). In case of arc welding, as is practiced in experimental part of this study, electric discharge at anode and cathode produces heat. The major output of a heat source being useful in evaluation the temperature distribution, is heat input which significantly influences cooling rate and is a key parameter in thermal analysis in CWM.

In arc welding processes functioning in continuous manner, heat input which is a relative measure of energy transferred into the weld pool per unit time, is calculated from the following equation:

$$Q_g = U.I \quad (1)$$

Where Q_g is nominal or gross heat flow or heat input per unit time, U is voltage of the arc and I is electric current. Since during welding, heat is dissipated through the edges of the material, net or effective heat input resulting in melting the material should be considered (Kou, 2003, p. 37). The relation between nominal heat input and net heat input is established by defining dimensionless heat source efficiency coefficient η which is determined by the equation below:

$$\eta = \frac{Q_e}{Q_g} \quad (2)$$

Where η denotes dimensionless heat source efficiency coefficient and Q_e indicates the net heat input per unit time. Heat source efficiency varies for different welding processes as is shown in the table 2.

Table 2. Recommended heat source efficiency values for different processes (Grong, 1997, p. 27).

<i>Welding Process</i>	<i>SAW steel</i>	<i>SMAW steel</i>	<i>GMAW CO₂-steel</i>	<i>GMAW Ar-steel</i>	<i>GTAW Ar-steel</i>	<i>GTAW He-Al</i>
η	0.91-0.99	0.66-0.85	0.75-0.93	0.66-0.7	0.25-0.75	0.55-0.8

Heat input can also be expressed in terms of transferred energy per unit length by taking welding speed v into consideration as is stated by the following relationship:

$$Q_w = \frac{Q_e}{v} \quad (3)$$

Where Q_w denotes the net heat input per unit length and v is welding travel speed.

Another noteworthy feature of a heat source is power density which is intensity of heat source to cause melting. This power density which is interchangeably used with heat flux, heat flow or heat source density might be expressed per unit area or per unit volume. The heat input of a source required for welding, drops as power density of the heat source

increases. As shown in the figure 5, deeper penetration depth, better welding quality and higher welding speeds are advantages of increasing the power density of a heat source (Kou, 2003, p. 4).

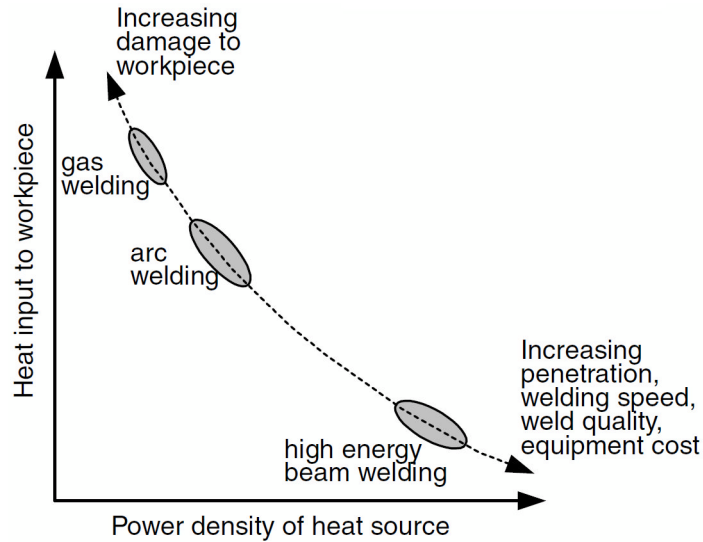


Figure 5. Effects of variation of heat input and power density (Kou, 2003, p. 4).

3.3 Thermal Analysis

As previously mentioned, the central task in welding simulation is modeling a transient heat source. That is, temperature field history is calculated through non-linear thermal analysis beneath which underlies heat conduction equation in which temperature-dependent thermo-physical properties of material are applied.

3.3.1 Fourier's Law of Heat Conduction

Heat conduction theory was formulated by Fourier in the early 19th century. Fourier's law states that heat flux or heat flow density from a surface is proportional to the temperature gradient with minus sign which signifies that in the direction of the falling temperature heat flows (Serth & Lestina, 2014, p. 2). In one dimensional condition, it has the following form:

$$q' = -k \frac{\partial T}{\partial x} \quad (4)$$

Where q' denotes heat flux density per unit area, k indicates material's thermal conductivity, $\partial T/\partial x$ shows the temperature changes in the arbitrary direction x . A more general form of Fourier's law for a three-dimensional problems is expressed through adding the heat flux in all three dimensions:

$$\vec{q}' = -k\left(\frac{\partial T}{\partial x}\vec{i} + \frac{\partial T}{\partial y}\vec{j} + \frac{\partial T}{\partial z}\vec{k}\right) \quad (5)$$

Where \vec{q}' shows the heat flux density vector, $\vec{i}, \vec{j}, \vec{k}$ are unit vectors related to directions x, y, z in Cartesian coordinate system, respectively. The term between parentheses in the above equation, is a vector known as temperature gradient shown also by ∇T and ultimately heat flux vector can be stated as:

$$\vec{q}' = -k\nabla T \quad (6)$$

Where ∇ is divergence operator and is defined by the following relationship:

$$\nabla = \left(\frac{\partial}{\partial x}, \frac{\partial}{\partial y}, \frac{\partial}{\partial z}\right)$$

3.3.2 Constitutive Heat Conduction Equation

Transient thermal analysis during welding is described by the constitutive heat conduction equation for an isotropic and homogeneous material which is derived from Fourier's law and law of energy conservation (Guo, 2015, p. 263):

$$\rho(T)c_p(T)\frac{\partial T}{\partial t} = \frac{\partial}{\partial x}\left(k(T)\frac{\partial T}{\partial x}\right) + \frac{\partial}{\partial y}\left(k(T)\frac{\partial T}{\partial y}\right) + \frac{\partial}{\partial z}\left(k(T)\frac{\partial T}{\partial z}\right) + \dot{Q}_v \quad (7)$$

Where $\rho(T)$, $c_p(T)$ and $k(T)$ denote density, specific heat and thermal conductivity of material as a function of temperature, respectively. t represents time and \dot{Q}_v is known as volumetric heat source density or internal volumetric heat generation rate.

3.3.3 Initial and Thermal Boundary Conditions

Solving the aforesaid differential equation entails integration process which typically inserts arbitrary constant into the equation. Finding a unique solution for the equation requires defining specific conditions i.e. evaluation of the function value at certain values for independent variables and correspondingly, exerting force to solve the equation under the mentioned condition, results in unique values. (Çengel & Ghajar, 2015, pp. 82-83)

Defining temperature distribution at initial time $t = 0$ is function of Cartesian coordinates and mathematical expression takes the form of:

$$T(x, y, z, 0) = f(x, y, z) \quad (8)$$

The condition above where $f(x, y, z)$ is temperature distribution at the time $t = 0$ in a solid body, is called initial condition and in the case of welding with isothermal medium, $f(x, y, z) = T_0$ in which T_0 is a constant equal to ambient or room temperature.

The most frequently-encountered thermal boundary conditions are specified temperature, specified heat flux, convection and radiation (Çengel & Ghajar, 2015, p. 84). In simulation of welding processes, nevertheless, heat losses by convection or radiation or a combination of which, comprises thermal boundary conditions.

3.3.3.1 Newton's Law of Cooling

Heat loss by convection during welding is expressed through Newton's law of cooling which states that heat flow density from a medium is proportional to the temperature difference between the body and the surrounding area i.e. the hotter the object, the more rapidly it cools down as is stated by the following equation:

$$q'_c = h_c(T - T_0) \quad (9)$$

Where q'_c and h_c are respectively, convective heat flow density per unit area and convective heat transfer coefficient. T Denotes body temperature and T_0 indicates ambient temperature. Heat losses due to convection are prevailing for lower temperatures (Deng & Murakawa, 2006a).

3.3.3.2 Law of Heat Transfer by Radiation

Another source of heat loss during welding is radiation in which heat dissipates as an electromagnetic wave. Thermal radiation is governed by Stefan-Boltzmann's law which considers the heat flow density per unit area is directly correlated to the fourth power of temperature difference between the medium and the ambient (Radaj, 1992, pp. 24-25):

$$q'_r = \varepsilon^* \sigma^* (T^4 - T_0^4) \quad (10)$$

Where q'_r denotes radiative heat flow density per unit area, $\varepsilon^* < 1$ is dimensionless emissivity of the boundary surface and Stefan-Boltzmann's constant is shown by $\sigma^* = 5.67 * 10^{-8} [\frac{J}{m^2sK^4}]$. Heat loss through radiation is dominant in high temperatures. The fourth power of temperature difference implies a highly non-linear condition and hereupon, boosting the computational cost during the analysis. Linearization of the equation is performed via defining a radiative heat transfer coefficient:

$$q'_r = h_r (T - T_0) \quad (11)$$

Where h_r signifies radiative heat transfer coefficient. Implementation of the combined boundary condition in simulation of welding with specified parameters by means of FEM will be discussed in more details further in the chapter 5.

3.4 Mathematical Modeling of Heat Source

Modeling a heat source is a rigorous task considering the complexity of a combined interaction of different factors with weld pool. The early endeavors to present an analytical method so as to calculate the temperature field history of a moving heat source in arc welding was made by Rosenthal leading to punctual and line heat sources to be put forward (Rosenthal, 1946). From that time onwards, remarkable improvement was made and a variety of mathematical models with respect to analysis and modeling a moving heat source were suggested (Pavelic, et al., 1969; Paley & Hibbert, 1975; Westby, 1968; Goldak, et al., 1984). In the following, some of those models, their characteristics and formulations are discussed shortly.

3.4.1 Rosenthal's Point Source

Applying Fourier's heat flow theory, Rosenthal (1946) proposed solution to find the temperature distribution generated by moving a point heat source on the surface of semi-infinite plate:

$$T - T_0 = \frac{Q_e}{2\pi kR} e^{-\frac{v(w+R)}{2\alpha^d}} \quad (12)$$

Where Q_e indicates net heat input per unit time, k is thermal conductivity, v represents welding travel speed, α^d is thermal diffusivity, R and w are distances from the center of arc and distance in x direction in a moving coordinate, respectively, which can be calculated from the following formula (Eagar & Tsai, 1983):

$$R = \sqrt{w^2 + y^2 + z^2} \quad (13)$$

$$w = x - vt \quad (14)$$

$$\alpha^d = \frac{k}{\rho c_p} \quad (15)$$

Where ρ and c_p are density and specific heat respectively. Rosenthal's point source due to its intrinsic nature which ignores actual temperature distribution on the surface, phase changes and molten metal flow in the weld pool strongly affecting the weld pool shape, is prone to serious inaccuracies, particularly in fusion zone (FZ) and HAZ (Nunes, JR, 1983; Goldak, et al., 1984).

3.4.2 Surface Flux Distribution (Pavelic's Disk Model)

Deficiencies in Rosenthal's models, triggered conduction of several researches to enhance the prediction of thermal field history during welding. Pavelic et al. (1969) developed a model which took into account temperature distribution over the surface of the solid material. This model which is also known as Pavelic disk's model, follows a Gaussian distribution (normal distribution) for the heat flux applied during welding which is stated as follows:

$$q'(r) = q'(0)e^{-Cr^2} \quad (16)$$

Where $q'(r)$ signifies heat source surface flux at radius r , $q'(0)$ shows the maximum heat flux density at the center of arc, C is defined as distribution width coefficient depending on diameter of the heat source and r is radial distance from the center of the heat source. Although surface flux distribution model is superior and more realistic compared to Rosenthal's method, it is explained that this model, nonetheless, is incapable of justifying the rapid heat transfer through FZ and more importantly, this model is impractical where prediction of FZ in deep penetration welding processes such as electron beam welding (EBW) or laser welding is concerned. Some researchers put into effort to present alternative methods (Friedman, 1975; Krutz & Segerlind, 1978).

3.4.3 Hemispherical Heat Source Model

Inefficacy of surface flux distribution concerning the temperature distribution in weld zone in high power density welding processes, led to emerge of volumetric source models. Mathematical expression of hemispherical heat source model takes the form of:

$$q''(x, y, \xi) = \frac{6\sqrt{3}Q_e}{c_l^3\pi\sqrt{\pi}} e^{-\frac{3x^2}{c_l^2}} e^{-\frac{3y^2}{c_l^2}} e^{-\frac{3\xi^2}{c_l^2}} \quad (17)$$

Where $q''(x, y, \xi)$ is power density, c_l is the characteristic radius of heat flux distribution, ξ is defined via the following equation connecting fixed to the moving coordinate system:

$$\xi = z + v(\tau - t) \quad (18)$$

Where τ is a lag factor through which position of heat source at the time $t = 0$ is defined. Notwithstanding the superiority of this model considering a volumetric source to the Pavelic's model, the ability of hemispherical model respecting appropriate modeling the welds which spherically are non-symmetric is questionable (Goldak & Akhlaghi, 2005, p. 30).

3.4.4 Ellipsoidal Heat Source Model

The aforementioned weakness of hemispherical model brought about development in heat source distribution prediction where ellipsoidal power density model was proposed assuming an ellipsoidal shape for heat source distribution with semi-axes of the ellipsoid a, b, c related to coordinate axes x, y, ξ which is expressed by the following equation:

$$q''(x, y, \xi) = \frac{6\sqrt{3}Q_e}{abc\pi\sqrt{\pi}} e^{-\frac{3x^2}{a^2}} e^{-\frac{3y^2}{b^2}} e^{-\frac{3\xi^2}{c^2}} \quad (19)$$

The above equation can also be transformed for a fixed coordinate system:

$$q''(x, y, z, t) = \frac{6\sqrt{3}Q_e}{abc\pi\sqrt{\pi}} e^{-\frac{3x^2}{a^2}} e^{-\frac{3y^2}{b^2}} e^{-\frac{3[z+v(\tau-t)]^2}{c^2}} \quad (20)$$

3.4.5 Goldak's Double Ellipsoidal Model

Drawing comparisons between measurement of thermal gradient and calculations by ellipsoid power density distribution demonstrated that temperature gradient in front of the heat source is much sharper than the rear part and on this account, further a mathematical model elaborated by Goldak et al. (1984) which postulates Gaussian thermal distribution of heat source is made up of two ellipsoidal shapes, stepped into existence (see the figure 6).

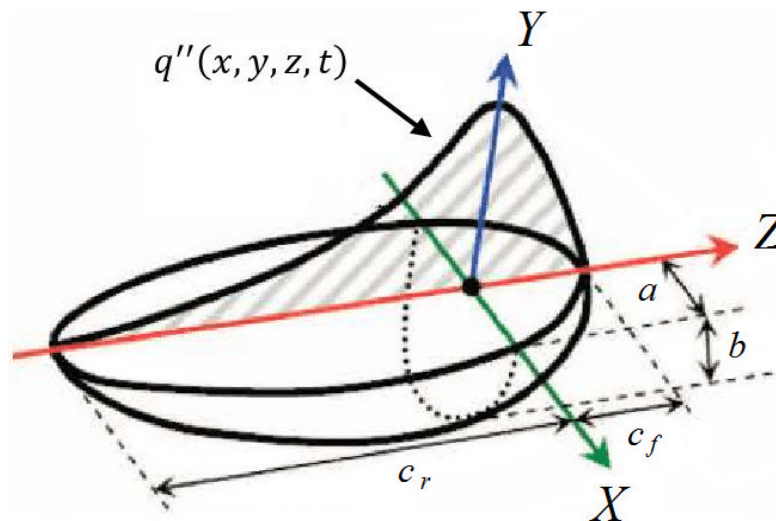


Figure 6. Schematic of Goldak's double ellipsoidal heat source model.

Volumetric heat flux in the front half of the source is calculated by the following equation:

$$q''(x, y, z, t) = \frac{6\sqrt{3}f_f Q_e}{abc_f \pi \sqrt{\pi}} e^{-\frac{3x^2}{a^2}} e^{-\frac{3y^2}{b^2}} e^{-\frac{3[z+v(\tau-t)]^2}{c_f^2}} \quad (21)$$

Where f_f and c_f respectively denote the dimensionless fraction of transferred heat and semi-axis in the front half, Q_e is calculated from equation (2) and volumetric heat flux density is indicated by $q''(x, y, z, t)$. Likewise for the rear half:

$$q''(x, y, z, t) = \frac{6\sqrt{3}f_r Q_e}{abc_r \pi \sqrt{\pi}} e^{-\frac{3x^2}{a^2}} e^{-\frac{3y^2}{b^2}} e^{-\frac{3[z+v(\tau-t)]^2}{c_r^2}} \quad (22)$$

Where f_r signifies the fraction of heat deposited in the rear part and c_r is semi-axis in the rear part. Taking the continuity of the heat source into account, the following correlations are observable:

$$\frac{f_r}{c_r} = \frac{f_f}{c_f} \quad (23)$$

$$f_f + f_r = 2 \quad (24)$$

Substitution the equation (24) in equation (23), f_f and f_r can be obtained from the following mathematical expressions:

$$f_f = \frac{2c_f}{c_f + c_r} \quad (25)$$

$$f_r = \frac{2c_r}{c_f + c_r} \quad (26)$$

Weld pool characteristics parameters namely a , b , c_r and c_f are influenced by welding parameters and can be estimated through metallography of the cross-section and surface ripple markings of the weld pool (Goldak & Akhlaghi, 2005, p. 34). Double-Ellipsoidal model was revealed to have flexibility to model both high power density welding processes as well as shallow penetration arc welding processes (Goldak, et al., 1984). In case of deep penetration welding such as EBW and laser welding, nonetheless, the most stringent results were obtained applying a conical heat source model with Gaussian and linear distribution respectively for radial and axial directions (Goldak, et al., 1986).

3.5 Metallurgical Aspects of Welding

From Metallurgical standpoint, welding comprises diverse phenomena such as melting, diffusion, phase-transformation, solidification, etc., each can have a significant effect on final microstructure of the weld. Investigation of welding metallurgy necessitates having a sufficient knowledge of physical metallurgy of steels, phase equilibrium, phase transformation mechanism and temperatures along with microstructural constituents and relevant terminologies which will be discussed briefly in the following.

3.5.1 Physical Metallurgy

In liquid state, metals are amorphous with no arranged atoms. As temperature decreases below the liquidus temperature T_L at which solid starts to form from liquid in cooling, small particles of solid called nuclei begin to form. As solidification proceeds, nuclei grow larger and turn into grains. Approaching the solidus temperature T_S at which the last liquid vanishes in cooling and below which solid phase is stable, grains meet at irregular sites referred to as grain boundaries. (Durand-Charre, 2004, p. 48; Hartmann, et al., 2001, pp. 116-117)

Metals in solid state have crystalline structure. Atoms in each crystal are ordered in a regular and repeating paradigm called crystal lattice. Each grain at a certain temperature has a crystalline structure similar to the other grains, however, each grain develops individually independent from other grains and as a result, varies lattice orientation from one grain to another. Typical crystalline structures in metals are body-centered cubic (BCC), face-centered cubic (FCC) and hexagonal close-packed (HCP) as shown in the figure 7. (Durand-Charre, 2004, pp. 38-39; Hartmann, et al., 2001, p. 116)

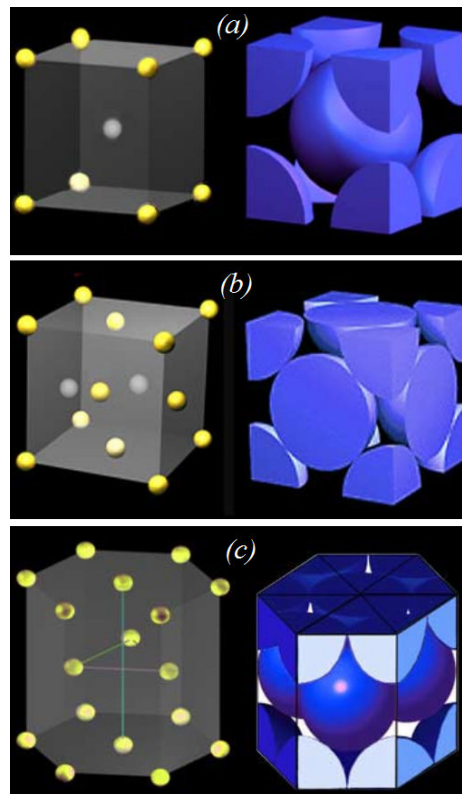


Figure 7. Schematic of general crystal structures in metals.

3.5.2 Phase Diagram and Solid Phases

Compared to pure metals, metal alloys are far more employed in engineering applications which typically contain metallic or non-metallic elements in their matrix. Alloying elements which are deliberately added to the base metal in order to enhance desirable properties of material, might place in the matrix of parent metal in either substitutional or interstitial solid solution. In case of presence of different alloying elements, several phases with their own crystalline lattice might form due to incomplete dissolution of alloying element in base material matrix. Those phases are time-temperature-dependent and might transform to other phases upon heating or cooling. The presence of alloying elements and amidst them carbon in steels, has pronounced effect in phase transformation temperature and fraction of different phases. Structure and stability of each phase for a specified alloy system in different temperatures along with metallurgical events and microstructural control are well described by phase diagrams or constitutional diagrams. (Callister, 2000, pp. 282-286) Figure 8 demonstrates the phase diagram for steels in which equilibrium of Iron-Iron Carbon versus temperature is plotted.

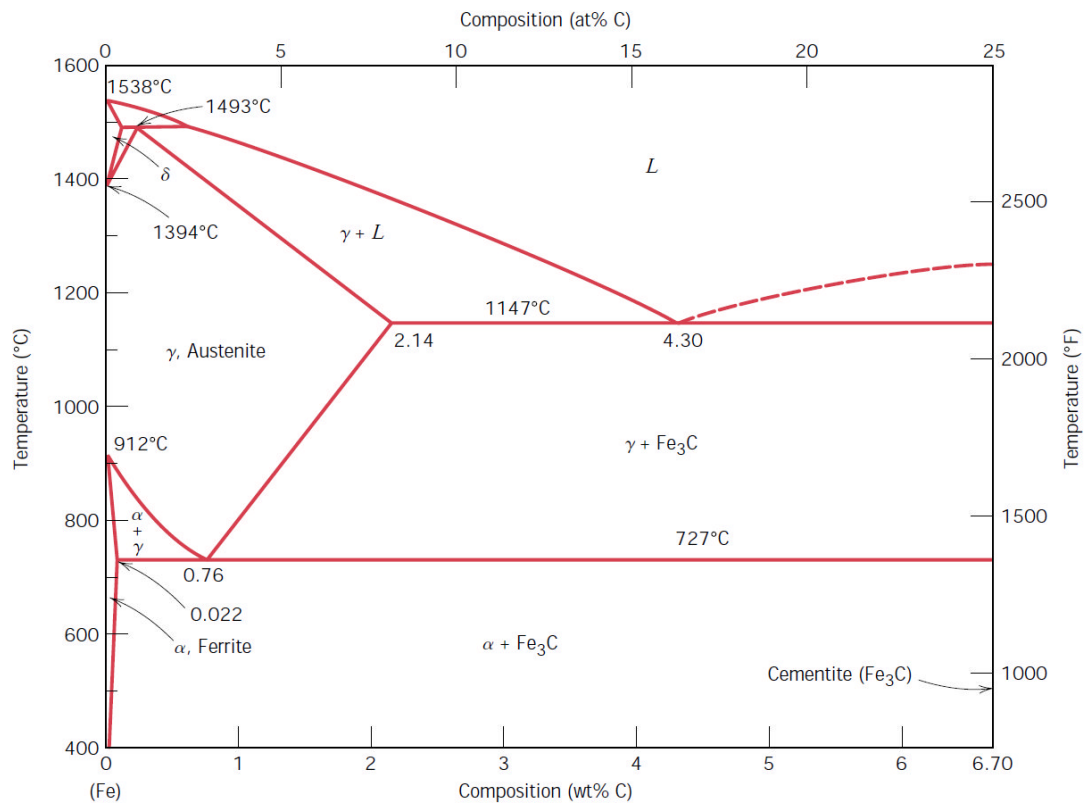


Figure 8. Fe-Fe₃C phase diagram (Callister, 2000, p. 303).

Different equilibrium phases are distinguishable in metastable Fe-C phase diagram; δ -ferrite, austenite, cementite (Fe₃C) and α -ferrite.

Delta iron (δ -Fe) which is a phase with BCC crystalline lattice being stable at high temperatures between almost 1394 °C and melting point. Gamma iron (γ -Fe) which is also known as austenite with FCC lattice structure and remains stable between 912 and 1394 °C (Callister, 2000, p. 302).

3.5.2.1 α -Ferrite

Interstitial solid solution of carbon atoms in α -iron is termed ferrite having a BCC crystalline structure with a slight carbon solubility which has direct correlation with temperature increase, rising from 0.008% at almost 0 °C to a maximum amount of 0.022% at A_1 Temperature.

3.5.2.2 Austenite

Solid solution of carbon atoms in γ -iron is called austenite which is not stable at temperatures below A_1 temperature. Similar to ferrite, carbon interstitially dissolves in iron lattice, nevertheless, solubility of carbon atoms in FCC structure is far greater than BCC lattices. The solubility of carbon in austenite increase as temperature rises, fluctuating between 0.8% at A_1 (eutectoid) temperature and almost 2.14% at 1147 °C. If austenite is heated above A_1 temperature and held sufficiently with respect to time, homogenous austenite is produced and the process is referred to as austenitization.

3.5.2.3 Cementite

Iron carbide (Fe_3C) is a hard and brittle intermetallic compound in iron-carbon phase diagram which is also called cementite. Cementite contains approximately 6.67% carbon and owns orthorhombic crystalline lattice. Cementite is metastable and remains indefinitely at ambient temperatures. Owing to the fact that cementite is not factually an equilibrium compound, the iron-carbon phase diagram is called metastable phase diagram.

3.5.2.4 δ -Ferrite

Solid solution of carbon in δ -iron is named δ -ferrite with a BCC structure similar to α -ferrite however, with a different lattice parameter. Carbon atoms are dissolved in this phase up to 0.1% at almost 1495 °C.

3.5.3 Phase transformation

Being small-scale structure of a material subject to microscopic examination, microstructure is extensively responsible for physical and particularly mechanical properties of material. In context of steels, characterization of microstructure is based on the present phases and their fractions, topological arrangement and the direction in which they are placed. Microstructure itself changes upon the variation of alloying elements and carbon in particular, heating rate and the temperature to which material is heated as well as cooling rate. (Callister, 2000, p. 324)

As pointed out before, microstructural alteration befalls upon heating and cooling. In this scheme and concerning the phase transformation of steels, special attention should be focused on two critical temperatures playing a practically important role in microstructural

transformations of steels. The lower critical or eutectoid temperature which is conventionally designated by A_1 , is austenite disappearance temperature in cooling as well as austenitization start or cementite disappearance temperature during heating, below which all austenite is transformed into ferrite and cementite. The upper critical temperature or α -ferrite disappearance temperature in heating is frequently shown by A_3 which is the temperature at which austenitization is completed and above which, merely austenite dominates. (Callister, 2000, p. S-125) These critical temperatures depends on carbon content and alloying elements.

SSPT and in this special case, austenite decomposition, can be divided into two major categories, namely diffusional and diffusionless transformations.

3.5.3.1 Diffusional Transformations

Diffusional transformations are also known as diffusive or diffusion-controlled as well as civilian transformations. In diffusional transformation, might exist one or more nascent phases whose chemical compositions differ from the extant parent phase which requires long-distance diffusion. Diffusional transformations might proceed in another fashion in which original phase decomposes into one or more new phases with similar composition, however, different crystalline lattice. As the name indicates, the most substantial factor in this transformation is thermally activated atomic diffusion or movement of individual atoms. Inasmuch as diffusion is a time-dependent phenomenon, such transformations are not instantaneous and occur in the course of time. The process of a diffusive transformation commences with nucleation of infinitesimal particles also known as nuclei generally at grain boundaries followed by their growth until attainment a fraction which is thermodynamically in equilibrium. (Durand-Charre, 2004, p. 178; Porter, et al., 2009, p. 261)

For a eutectoid steel when austenite is slowly cooled down below the eutectoid temperature, a diffusive transformation occur in which austenite decomposes into a contiguously formed mixture of cementite lamellae embedded in alternate ferrite. This microstructure whose composition unequivocally differs from its parent phase, is called pearlite and eutectoid reaction is often termed as pearlite transformation. (Callister, 2000, p. 306; Durand-Charre, 2004, p. 194)

In addition to formation of pearlite upon austenite decomposition, other microstructural constituents might appear depends on cooling rate. One of those microconstituents is bainite whose transformation happens in temperature ranges between those for pearlite and martensite. Microstructure of bainite is a mixture of ferrite and cementite in which needles of ferrite are separated by particles of cementite. Diffusion of carbon controls the rate of nucleation and growth of bainite. (Durand-Charre, 2004, p. 223) Mechanism of bainite formation is complicated and despite having distinct diffusive prospects regarding its transformation, is a case of controversy which includes both displacive and diffusional interpretation (Hackenberg, 2012, p. 30).

3.5.3.2 Diffusionless Transformations

The terms non-diffusive, displacive or military transformations are interchangeably used with diffusionless transformation which refers to a transformation in which the chemical composition of the nascent phase which is thermodynamically metastable, remains identical to extant parent phase, however, there is a change in crystalline lattice compared to the parent phase. As the name of the transformation implies, cooperative displacement of atoms, dominantly by shear movement happens. The distances over which this movement happens, is less than an atomic diameter leading to a change in crystalline lattice. Inasmuch as atoms are displaced in a regimented manner together in a block, such transformation is also termed military transformation. (Porter, et al., 2009 , p. 383; Durand-Charre, 2004, p. 178; Kelly, 2012, p. 5)

Martensitic transformation in steels is best example of displacive transformations. Martensite as a microstructural constituent is formed upon the rapid cooling or quenching of austenite to relatively low temperatures. Owing to high quenching rate, diffusion of carbon atoms are prohibited and thus, diffusion is not incorporated in such transformation. As a result, this time-independent athermal transformation which is only contingent upon temperature, occur instantaneously, i.e. nucleation and growth of martensite grains happen in a very rapid rate, almost as high as velocity of sound, in the matrix of austenite. (Callister, 2000)

Martensite is a single phase metastable microconstituent (Callister, 2000, p. 334; Durand-Charre, 2004, p. 209) which is inherited ideally the chemical composition of its extant parent phase, namely, austenite (Deng, 2009). Upon rapid cooling, dissolved carbon atoms are locked in octahedral interstitial sites between iron atoms (Deng, 2009; Kelly, 2012, p. 11) and FCC crystal structure of austenite undergoes a change into Body-centered tetragonal (BCT) martensite. In other words, Martensitic transformation occur upon shear deformation of austenite structure and trapping the carbon atoms in solid solution in a BCT lattice (Lancaster, 1999, pp. 226-228). BCT structure as is shown in the figure 9, is similar to BCC structure which is expanded along one of its axes. Martensite can be called as supersaturated solid solution of carbon atoms in BCC ferrite (Callister, 2000, p. 335; Porter, et al., 2009, p. 383).

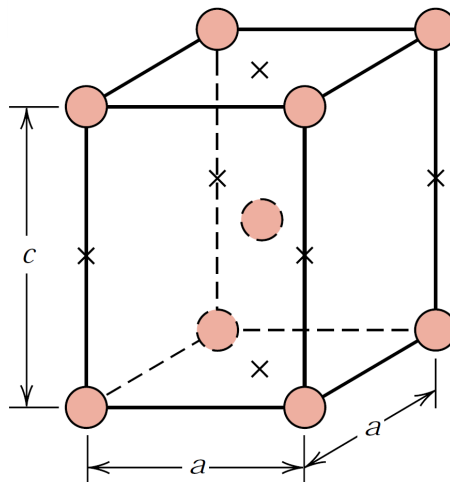


Figure 9. BCT crystal structure which is elongated in c direction (Callister, 2000, p. 335).

3.5.4 Thermal Cycle and Microstructure Evolution in Welding

From Metallurgical standpoint, microstructure of the joint in fusion welding, can be categorized into FZ, HAZ and base material. FZ is characterized by the points whose peak temperatures exceed melting temperature. A part of base material adjacent to FZ, essentially undergoes thermal cycles with sharp ascent in temperature up to approximately melting point ensued by a smooth fall. As the distance from weld line increases, the peak temperature and sharpness of the cycle for this area drops. This critical zone is called HAZ which is characterized by the area whose peak temperature fluctuates between A_1 temperature and melting point. (Radaj, 1992, p. 100)

Due to peak temperatures experienced by this area during welding thermal cycle as a result of retaining various distances from weld line, HAZ can be divided into four distinct subzones: the coarse-grained HAZ (CGHAZ) which is adjoining the FZ, the fine-grained HAZ (FGHAZ), the inter-critical HAZ (ICHAZ) and the sub-critical HAZ (SCHAZ) which is adjacent to the base material. Microstructural evolution in each subzone is highly dependent on peak temperature, cooling rate and the time that subzone is exposed to its peak temperature. (Yaghi, et al., 2008; Guo, et al., 2015)

CGHAZ in which grain growth occurs, is characterized by the area whose peak temperature exceeds grain-coarsening temperature, i.e. almost 1100 °C up to melting temperature. FGHAZ constitutes grains with sizes smaller compared to that of parent material and experienced peak temperatures in this subzone range from A_3 temperature to 1100 °C.

On traveling towards base metal, ICHAZ, a narrow region in which partial austenitization during SSPT occurs, forms between A_1 and A_3 temperatures. Passing through inter-critical subzone towards base material, peak temperature drops below A_1 temperature. Inasmuch as austenite transformation temperature is not reached, no phase transformation happens, nonetheless, owing to overtempering, limited growth of carbide is observable. (Yaghi, et al., 2008) This subzone is termed as SCHAZ. The figure 10 depicts schematically different subzones of HAZ for a high strength low alloy (HSLA) steel.

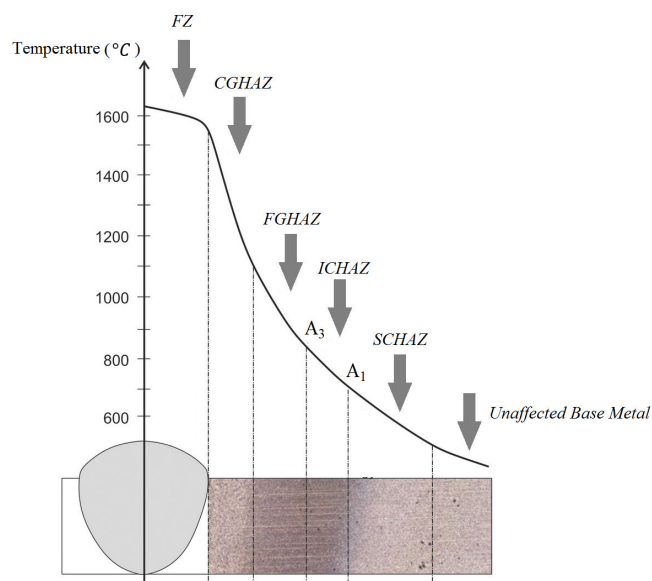


Figure 10. Different subzones of HAZ (Falkenreck, et al., 2017).

3.6 Mechanical Analysis

Residual stresses and deformations are evaluated upon solving non-linear elasto-plastic equations in mechanical analysis which uses the transient temperature history obtained in thermal analysis as thermal load. Structural analysis comprises a set of governing partial differential equations upon which prediction of straining and stress field becomes possible.

3.6.1 Equilibrium Equation

Partial differential equations regarding the equilibrium of momentum by which mechanical problem is governed can be expressed in matrix notation as follows (Chiumenti, et al., 2010):

$$\nabla \cdot \sigma + F_b = 0 \quad (27)$$

Where ∇ denotes divergence operator, σ is Cauchy stress tensor and F_b signifies body force vector. Using index notation equation (27) can be written as (Lee & Chang, 2011):

$$\sigma_{ij,j} + F_{bi} = 0 \quad (28)$$

3.6.2 Thermal Elasto-Plastic Constitutive Equation

The relation between stress and strain is generally expressed by constitutive equation as is demonstrated below in incremental form (Bhatti, et al., 2014):

$$\{d\sigma\} = [D]\{d\varepsilon\} - [C_{th}]\{dT\} \quad (29)$$

Where $d\sigma$, $d\varepsilon$ and dT are increments of stress, strain and temperature, respectively. C_{th} is matrix of thermal stiffness and $[D]$ can be defined as:

$$[D] = [D^e] + [D^p]$$

Where $[D^e]$ denotes the stiffness matrix in elastic range and likewise $[D^p]$ is plastic stiffness matrix.

3.6.3 Strain Hardening Models

Strain hardening (work hardening) is defined as increase in the strength of material through plastic deformation which can be observed as a rise in the stress-strain curve subsequent to yielding. Since loading and unloading affects the yield strength of steel materials, in terms of welding simulation, strain hardening exerts influence on formation of residual stresses owing to non-uniform thermal expansion. (Hansen, 2003, p. 51)

3.6.3.1 Isotropic Hardening

In isotropic hardening model, as is schematically depicted in the figure 11, following the yielding, yield surface sustains its initial shape, origin and orientation, however, it experiences uniform expansion in all directions in stress space during plastic deformation as stress rises (Hansen, 2003, p. 51). Neglecting the Bauschinger effect, isotropic hardening implies the condition that material during loading develops an increase in its yield due to work hardening. During unloading material does not undergo yielding until it reaches the same yield stress experienced during loading.

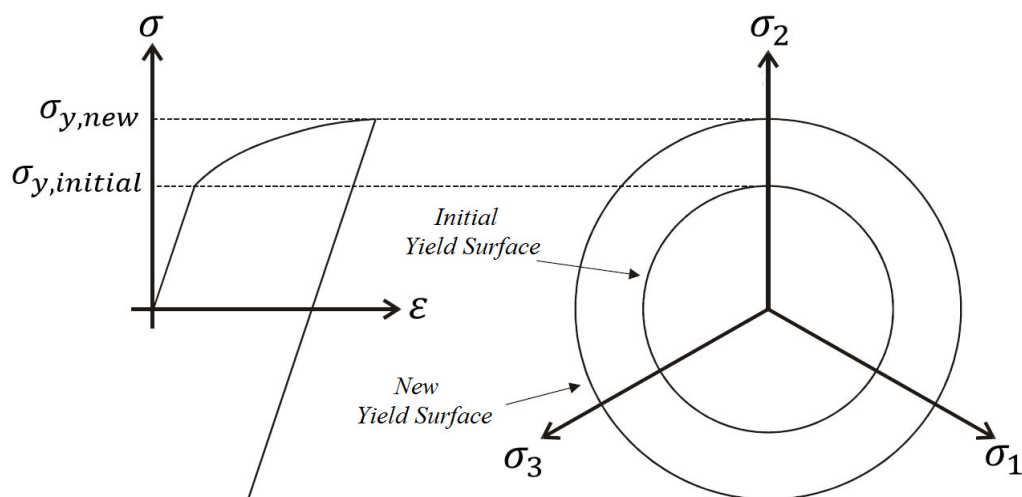


Figure 11. Isotropic hardening model (Hansen, 2003, p. 51).

3.6.3.2 Kinematic Hardening

In kinematic hardening model, yield surface is assumed to translate in stress space while retains its initial size, shape and orientation respecting the origin of stress space (Hansen, 2003, p. 52). Bauschinger effect in kinematic hardening model is considered where hardening in loading results in softening during subsequent unloading. Schematic of kinematic hardening model and change in yield surface origin is shown in the figure 12.

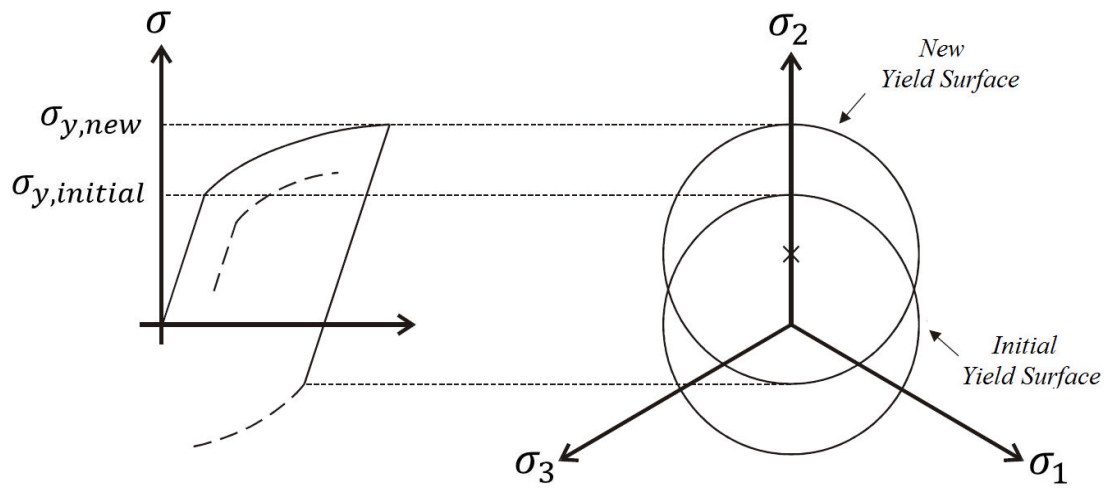


Figure 12. Kinematic hardening model (Hansen, 2003, p. 52).

4 EXPERIMENTAL SETUP

Single pass bead on plate welding of a low alloy UHSS using a robotized GMAW process is investigated. A series of measurements is performed prior to as well as post welding to guarantee the correctness and accuracy of simulation.

4.1 Welding Procedure

Prior to welding, base material in the vicinity of weld line as well as the location of thermocouples, was sandblasted to ensure a clean surface free from iron oxide. The base material is a rectangular plate with 8 mm thickness and 300 mm length and width. The plate is placed horizontally on four small supports without any clamping which allows free deformations. Heat conduction between the specimen and supports are neglected as they are insignificant and unlikely to affect the temperature distribution.

As welding starts, torch travels along the centerline of the plate and a layer of filler material is deposited on the surface of the base material in a single pass GMAW process. The start and stop position of the welding torch is marked at 10 mm far from each edge on the plates' centerline which makes the total welding length 280 mm. It is worthy of note that the plate is positioned in such a way that welding torch travels in transverse (perpendicular to rolling) direction. The convention for welding direction is assumed to be along the positive Y -axis and $+Z$ is normal to the top surface of the plate. Welding condition and arbitrary coordinate system considered for this study is shown in the figure 13.

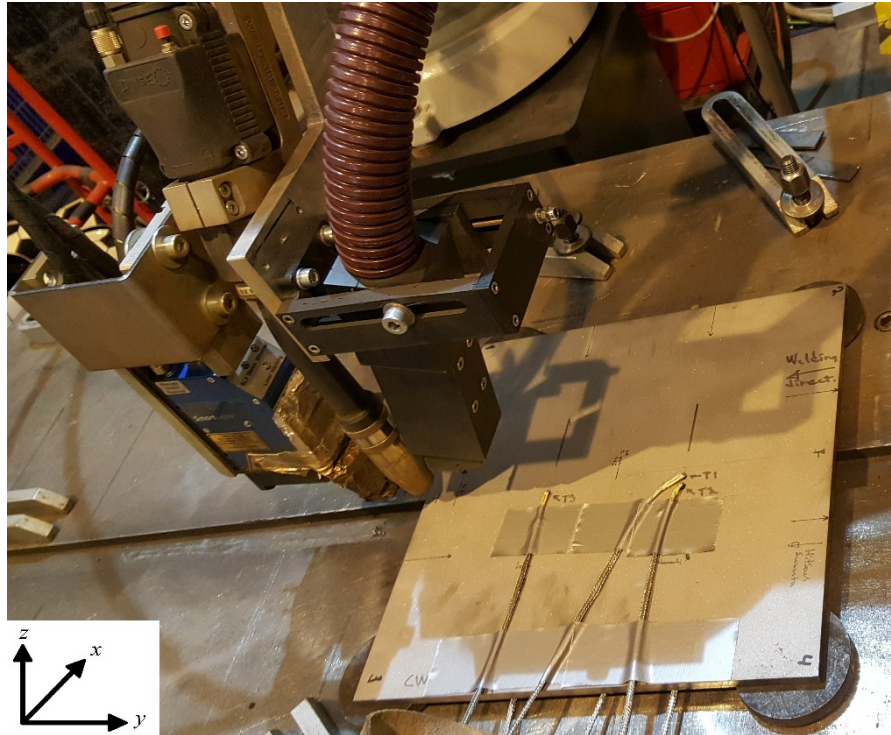


Figure 13. Robotized GMAW arm and position of the base plate.

Welding was performed in an ambient temperature of approximately 20 °C and no preheating based on the recommendations of the manufacturer of the base material was applied. Welding parameters should be chosen to meet the heat input requirements as this material undergoes softening effect and hence, heat input should be in an optimum level (Björk, et al., 2012). Table 3 provides the welding parameters applied in GMAW process.

Table 3. Employed welding parameters.

<i>Average voltage</i> (V)	<i>Average current</i> (A)	<i>Travel speed</i> $\left(\frac{m}{min}\right)$	<i>Wire feed rate</i> $\left(\frac{m}{min}\right)$	<i>Wire diameter</i> (mm)	<i>Gas flow</i> $\left(\frac{L}{min}\right)$	<i>Shielding gas</i>
28	200	0.42	10	1.0	19.3	92% Ar + 8% CO ₂

Considering a welding efficiency of 0.8 for GMAW process in this study a total energy equal to 179.2 kJ corresponding to a net heat input of 640 J/mm is supplied which lies in the permitted heat input range recommended by the manufacturer of this material.

4.2 Measurements

Monitoring the thermal cycle during welding is accomplished positioning several thermocouples at different locations on the top surface as well as bottom surface of the plate. Thermocouples on the top surface are named T_1 to T_4 and the ones on the bottom side are denoted with B_1 to B_3 . The position of attached thermocouples are shown in the figure 14.

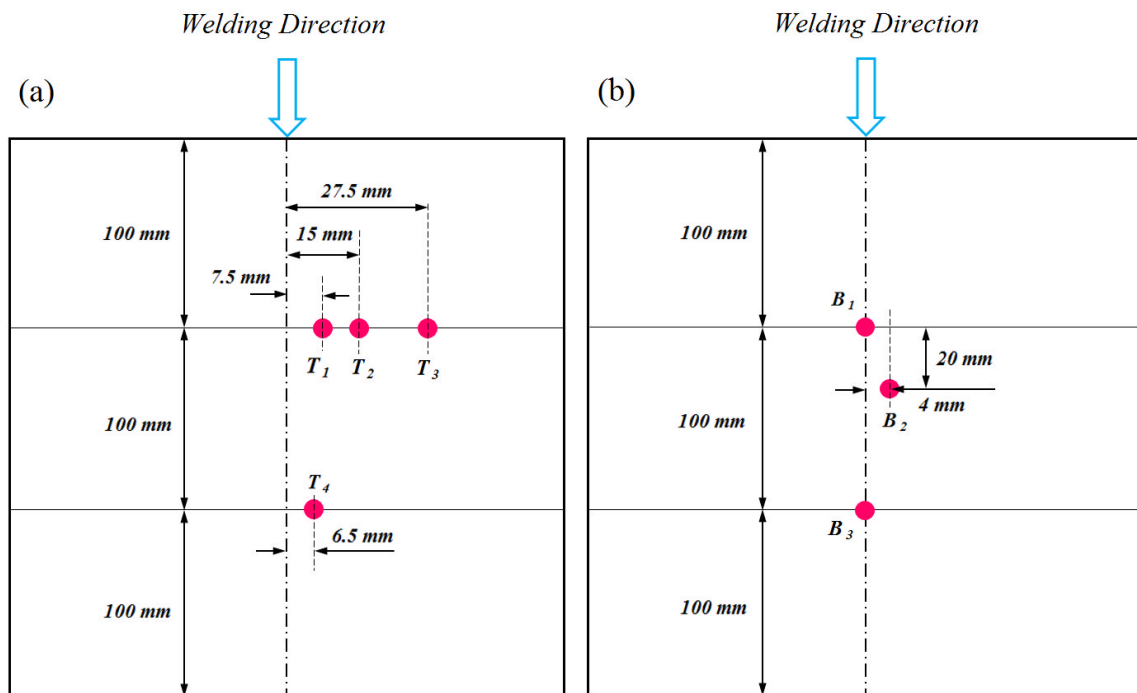


Figure 14. Location of thermocouples on top (a) and bottom (b) surfaces.

Dimensions of the test piece were measured using a laser shape measuring system before and after welding to make the possibility of analysis of deformation and comparison with numerical simulation.

X-ray diffraction method was applied to determine transverse residual stresses using Xstress 3000 G3 portable diffractometer on top surface in mid-section perpendicular to welding direction. Figure 15 (a) depicts schematically the axis along which transverse residual stresses are measured. The red line in the figure shows the measurement path. Angular distortion and out of plane bending deformation on specified paths before and after welding were measured using laser profile scanner to make the possibility of analysis of deformation and comparison with numerical simulation as are shown in the figure 15 (b). Green line shows the measuring paths for out of plane bending deformation along the weld seam. The

two red lines starting right beside the weld toe and ending at the edge of the test piece, demonstrate the measuring paths for angular distortion.

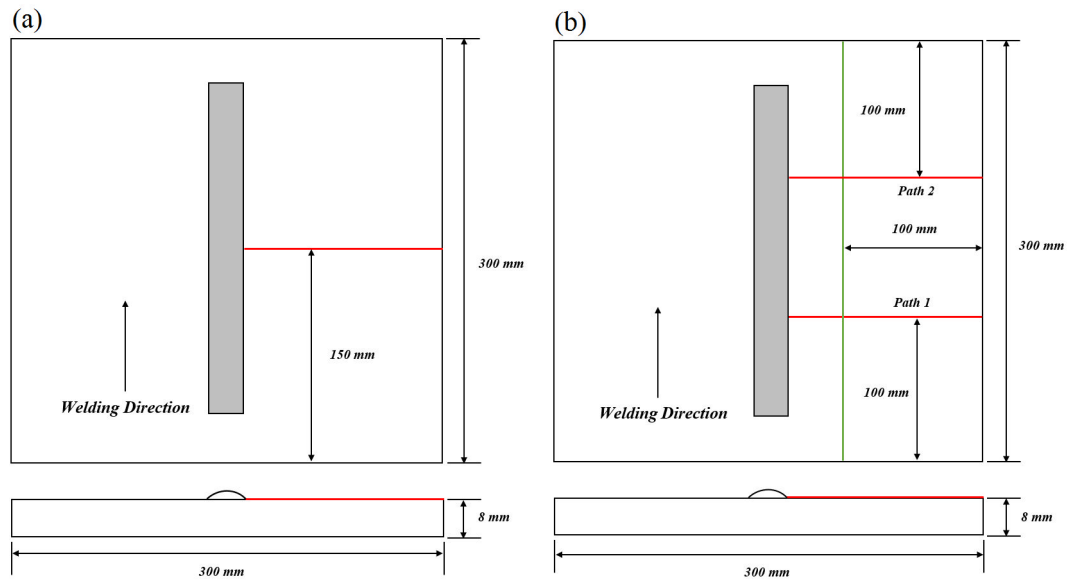


Figure 15. Residual stress (a) and distortions (b) measurement paths on top surface.

5 FINITE ELEMENT MODELING

Evolution of residual stresses due to a transient thermal field and consequent distortions by means of FEM is investigated in this study. Accurate prediction of temperature history and capturing the residual stresses are performed using sequentially-coupled formulation. Inasmuch as dimensional changes during welding are inconsequential and mechanical work performed is negligible in comparison with transferred thermal energy from the arc or in other words, the effect of stress field on thermal field is insignificant, sequentially-coupled analysis is stated to have a desirable performance (Deng & Murakawa, 2006a; Lee & Chang, 2009).

In thermal analysis, a moving heat source upon solving the non-linear constitutive heat conduction equation subject to defined boundary conditions is modelled and temperature field history is determined. Developing a well-defined computational strategy to model the thermal energy is the core of welding simulation. The resulting temperature distribution of all the nodes is then applied as a body load to find the structural response in the subsequent mechanical analysis.

5.1 Model Geometry and FE Mesh

Different geometry types have been applied in CWM based on the required accuracy level and available computational power. Two and three-dimensional models can be both applied to analyze residual stresses for bead on plate welding. Plane strain or generalized plane strain models assume heat flow in welding direction and longitudinal displacements to be zero and only analyze cross section of the weld. Plane stress models, however, are applicable for thin plates in which arc travels in the plane of the model. Stress through thickness is then ignored and displacement exists in the plane of the mesh. Three-dimensional models consider all the strain and stress components to be present and offer more accuracy but larger computational costs. (Lindgren, 2001a) Nonetheless, the numerical procedure to determine temperature history and simulation of residual stress distribution induced by GMAW process in this study is carried out developing a 3D thermo-metallurgical-mechanical FE model in Abaqus / Standard code. (ABAQUS, 2017).

The curvature of the deposited bead is extracted from the macrosection of the weld bead to model the as-welded geometry. Due to symmetry with regards to the weld centerline, only one half of the geometry is considered as analysis domain. Identical time steps and FE mesh, albeit with different element types, utilized in analysis of thermal contours and stress field because nodal temperatures captured in heat transfer analysis should be transferred to the model for structural analysis.

Accuracy of applied heat flux being caused by a traversing torch along the weld seam which results in high temperatures and increased stress gradient in FZ and HAZ has been ensured employing a fine mesh grid in molten zone and its vicinity which progressively becomes coarser as moving further towards the edges transverse to welding direction in order to save computational time as commonly used and justified by other researchers. (Ahn, et al., 2017; Lee & Chang, 2011) Mesh refinement was performed by generating several partitions through which gradual mesh coarsening has been applied as the distance from welding centerline increases. Mesh sensitivity analysis was accomplished to minimize the effect of mesh density on analysis precision. Mesh convergence is reached when further mesh refinement adds no more accuracy to the analysis. A fine mesh with a total number of 152078 elements and 169452 nodes and smallest element size of $1 \times 0.5 \times 0.5$ mm was found to be able to render accurate results as is depicted in the figure 16.

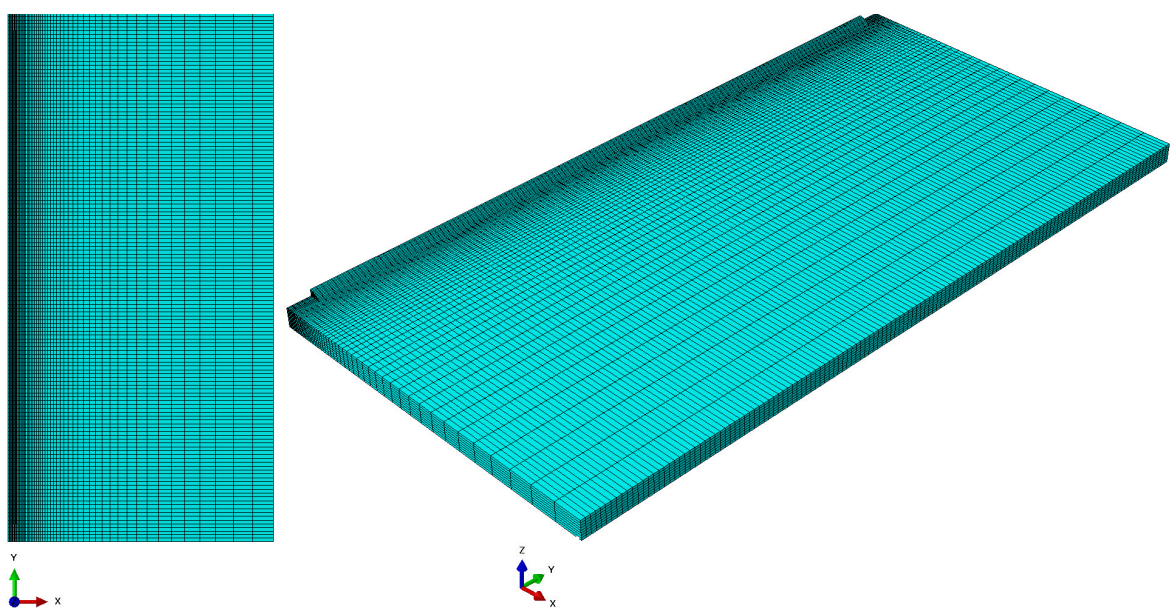


Figure 16. Meshed geometry for FE analysis.

5.2 Material Modeling

In CWM, material modeling in which thermo-physical and mechanical properties and even material microstructure are taken into account, becomes immensely prominent as they practically govern different phenomena in welding. In material modeling pertinent to welding simulations, material properties are frequently adopted as a function of temperature by researchers (Zhu & Chao, 2002). In order to evaluate the phenomena correctly and increase the accuracy of simulation, sufficient knowledge of material properties along with parameters to which might exert impacts, such as heating and cooling rates, seems to be necessary. Although precise measurement of temperature-dependent material properties is a matter of consideration in simulation of welding phenomena, a close attention to time-consuming and costly experiments and difficulty of obtaining accurate material data specifically in high temperatures should be paid. Influence of role-playing material properties on accuracy of welding simulation and residual stresses have been investigated by various researchers and simplifications and assumptions have been subsequently put forward to overcome simulation-related problems which will be discussed in the following sub-sections wherever appropriate. This study, however, uses temperature-dependent thermo-physical properties separately for base and filler materials and mechanical properties of filler material are assumed to be identical to that of parent material. It is attempted in this thesis to the feasible extent to measure temperature-dependent mechanical properties by conducting experiments. Other material properties are extracted from either JMatPro software or reliable existing literature and relevant formulae whenever applicable, to reach an adequate precision of required data for simulation. It is worthy to mention that all the mentioned material properties are calculated in heating direction.

5.2.1 Material under Investigation

The material under investigation in this study is Strenx[®]960 MC, a direct-quenched HSLA steel with low carbon content manufactured by SSAB. This material is made from hot strip rolling and direct-quenching processes which differs from steels manufactured with conventional quenching procedures i.e. hot rolling, reheating, quenching and finally tempering (Siltanen, et al., 2015). This UHSS offers a minimum yield strength of 960 MPa along with good formability and impact toughness (Guo, et al., 2015). Table 4 represents chemical composition of the parent material based on material's certificate of the manufacturer.

Table 4. Chemical composition of Strenx®960 MC (wt. %).

<i>C</i>	<i>Si</i>	<i>Mn</i>	<i>P</i>	<i>S</i>	<i>Al</i>	<i>Nb</i>	<i>V</i>	<i>Ti</i>	<i>Cu</i>	<i>Cr</i>	<i>Ni</i>	<i>Mo</i>
0.097	0.200	1.090	0.008	0.001	0.034	0.001	0.009	0.020	0.033	1.130	0.380	0.191

Considering low carbon and alloy contents, carbon equivalent value (CEV) which is a pivotal parameter in evaluation the weldability of steels as well as determining preheating and interpass temperature of welding, can be calculated by the following equation (Amraei, et al., 2016; Guo, et al., 2015):

$$CEV = C + \frac{Mn}{6} + \frac{Cr + Mo + V}{5} + \frac{Ni + Cu}{15} \quad (30)$$

Making use of equation (30), the resultant $CEV = 0.57$ demonstrates the material has good weldability without a necessity for preheating (Björk, et al., 2012).

Filler material used in the experimental part of the study for GMAW process is Böhler Union X96 solid wire with a diameter of 1 mm having virtually the same strength as the base material. Nominal and measured mechanical properties of Böhler Union X96 is shown in the table 5.

Table 5. Mechanical properties of Böhler Union X96 (Björk, et al., 2012).

	<i>Yield Strength</i> σ_y [MPa]	<i>Ultimate Tensile Strength</i> σ_u [MPa]	<i>Elongation</i> <i>A</i> [%]
<i>Nominal</i>	930	980	14
<i>Measured</i>	990	1245	14

5.2.2 Temperature-Dependent Thermo-Physical Properties

Analysis of transient heat transfer is dependent on specifying physical and thermal properties of material. These parameters namely, specific heat, thermal conductivity and density, basically vary upon temperature changes. Regarding the influence of each parameter as a constant value or a function of temperature on welding simulation and transient thermal distribution, several researches have been conducted (Heinze, et al., 2012; Little &

Kamtekar, 1998; Zhu & Chao, 2002; Bhatti, et al., 2015). These parameters, nevertheless, are calculated making use of JMatPro version 8.0.1. unless otherwise stated.

5.2.2.1 Specific Heat

Specific heat c_p is a measure of required heat per unit mass to increase the temperature of substance by 1 K. At constant pressures, it can be stated by the following equation (Porter, et al., 2009):

$$c_p = \left(\frac{\partial H}{\partial T}\right)_P \quad (31)$$

Where H is specific enthalpy and c_p shows specific heat.

Regarding the effect of specific heat on temperature distribution, referring to finding of other researchers concerning the calculation of 800-500 °C cooling time, Watt et al. (1988) contend that presumption of specific heat as a constant value is absolutely incorrect and might lead to serious errors in calculation. Bhatti et al. (2015) explain that among thermal properties required to predict temperature field in welding simulation of carbon steels, specific heat is the most remarkable parameter. It, thus, should be taken as a function of temperature especially for analysis of angular distortion. They state that notwithstanding the variation of specific heat with temperature, it is inconsequentially affected by steel grade and therefore was deemed the same for steel grades in their work. Other researchers, contrariwise, claimed specific heat to negligibly affect thermal field distribution in simulation problems and thus, taking the constant value of ambient temperature over the whole temperature range will lead to rational results for thermal analysis (Zhu & Chao, 2002). This investigation, nonetheless, takes advantage of temperature-dependent specific heat for both parent and filler materials as demonstrated in the figure 17.

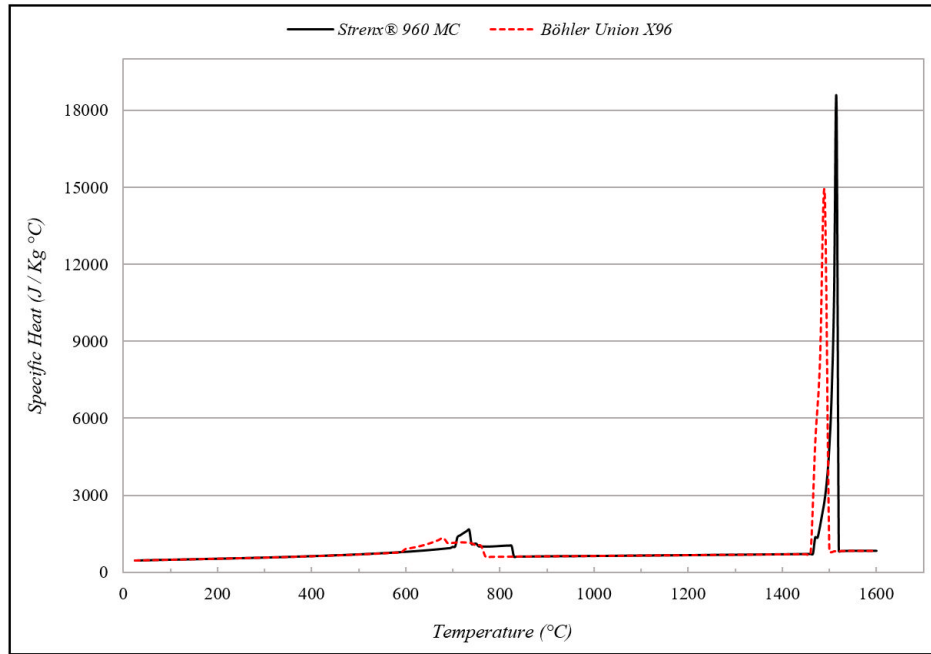


Figure 17. Specific heat as a function of temperature calculated by JMatPro.

5.2.2.2 Latent Heat

In figure 17, peaks at almost 750 °C and 1500 °C correspond to respectively, latent heat of transformation (solid-state austenitic transformation) and latent heat of fusion (solid-liquid transformation). The latter is the energy per unit mass should be transferred to a solid at its melting point to melt it without any change in temperature (Hansen, 2003, p. 44). It can be calculated by integration upon the area under the specific heat-temperature curve between the solidus and liquidus temperature. Applying the latent heat in model and removing the peak in specific heat graph in mushy zone has the advantage of avoiding the nonlinearity in modeling due to an abrupt change in material's property over a narrow temperature range and consequently reducing computational expense. Thermal impacts of solidification in weld puddle is reflected into the model by taking the latent heat of fusion into consideration as is practiced by other researchers (Deng & Murakawa, 2006a). The change in the specific heat in the mushy zone (between solidus and liquidus temperatures) might be defined as follows (Piekarska, et al., 2012):

$$c(T) = \begin{cases} c_S & T < T_S \\ \frac{c_S + c_L}{2} + \frac{H_L}{T_L - T_S} & T_S \leq T \leq T_L \\ c_L & T > T_L \end{cases} \quad (32)$$

Where c_S and c_L are respectively specific heat in solid and liquid states and H_L denotes latent heat of fusion. Solidus and liquidus temperatures are shown by T_S and T_L respectively, which can be measured experimentally, however, they can be approximated by empirical relations upon their chemical compositions (Qian, et al., 2012):

$$T_S = \begin{cases} 1534 - 410 \times C_e & C_e < 0.1\% \\ 1534 - 184 \times C_e & C_e > 0.2\% \\ 1493 & 0.1\% < C_e < 0.2\% \end{cases} \quad (33)$$

Where:

$$C_e = \frac{80.5(C) + 33.5(S + P) + 3.75(Mn) + 17.8(Si) + 3.8(Al) + 1.5(Cr) + 3(Ni)}{80.5}$$

Likewise, for liquidus temperature the following empirical relation can be employed (Gryc, et al., 2013).

$$T_L = 1536 - 65(C\%) - 8(Si\%) - 5(Mn\%) - 30(P\%) - 25(S\%) - 1.7(Al\%) - 5(Cu\%) - 1.5(Cr\%) - 4(Ni\%) - 2(V\%) - 7(Nb\%) - 14(Ti\%) \quad (34)$$

Together with the computed values for latent heat of fusion for the material under investigation and filler material, the values for solidus and liquidus temperatures calculated from the aforesaid equations are summarized in the table 6.

Table 6. Calculated values for latent heat of fusion, solidus and liquid temperatures.

	Latent heat of fusion $H_L \left[\frac{J}{kg} \right]$	Solidus Temperature $T_S [^{\circ}C]$	Liquidus Temperature $T_L [^{\circ}C]$
<i>Strenx[®] 960 MC</i>	237000	1465	1520
<i>Böhler Union X96</i>	260000	1460	1500

5.2.2.3 Thermal Conductivity

Thermal conductivity, k , is a material property which accounts for the ability of material to transfer the heat (Çengel & Ghajar, 2015, p. 18). A lower heat conductivity signifies that material cumulates more heat and hence, a longer time is required for the heat to be conducted to the neighboring material (Bhatti, et al., 2015). This parameter is highly temperature-dependent and varies upon the temperature changes.

With respect to the impact of thermal conductivity on transient thermal field in welding, a large number of studies have been hitherto conducted. Little & Kamtekar (1998) state that the value chosen for thermal conductivity is a decisive factor in transient thermal distribution as adopting a higher value of k , results in rising peak temperature in areas far from the weld seam and a lower peak in the weld region. It was concluded by Zhu & Chao (2002) that thermal conductivity has a definite impact in thermal field distribution and either an averaged or a constant conductivity value at room temperature will lead to acceptable results in prediction of thermal analysis, residual stresses and distortions in welding of aluminum. In a study to investigate the effect of thermo-physical and mechanical properties of different steel grades on angular distortion and residual stresses, Bhatti et al. (2015) declare that prediction of transient temperature field with reasonable accuracy is possible by applying temperature-dependent specific heat and assuming a constant value of ambient temperature for k . The same authors believe that evaluation of welding-induced residual stresses can be performed considering all the thermal properties at constant values, whereas for a precise analysis of angular distortion, it is of prominence that thermal properties and in particular, specific heat to be taken temperature-dependent within the thermal analysis. It has been emphasized the magnitude of thermal conductivity, broadly changes from one steel grade to another (Little & Kamtekar, 1998).

Two major phenomena are stated to be responsible for transferring heat in weld pool, namely conduction and thermo-capillary flow also known as Marangoni effect. The latter, which is the reason for accelerating the lateral thermal conduction at top of the weld puddle, exists owing to surface tension gradient. (Lampa, et al., 1999)

In order to compensate the convective stirring effect due to fluid flow in weld pool, an artificially increased value for thermal conductivity in temperatures above melting point is considered in modelling by different researchers. The magnitude of this effective heat conductivity due to Marangoni effect compared to the conductivity at room temperature, was considered between two and three between solidus and liquidus temperatures by various authors (Brickstad & Josefson, 1998; Danis, et al., 2010; Lampa, et al., 1999; Yaghi, et al., 2006). Taljat et al. (1998) and Lee & Chang (2011) assumed that thermal conductivity of material linearly increases by a factor of three between solidus temperature and 3000 K, whereas Barsoum & Barsoum (2009) considered an increase of almost sixfold in heat conductivity of material between solidus temperature and 2000°C. In his investigation, Hansen (2003, pp. 41-42) spread the increase in heat conductivity corresponding to molten area over rather a wide thermal range inasmuch as drastic changes in material properties in a narrow temperature span, necessitates small time step and consequently increased number of equations to solve and finally a large computational time. This study, considers temperature-dependent thermal conductivity which is depicted in the figure 18. It should be mentioned that in simulation, thermal conductivity is increased to almost three times the one of room temperature between T_S and T_L .

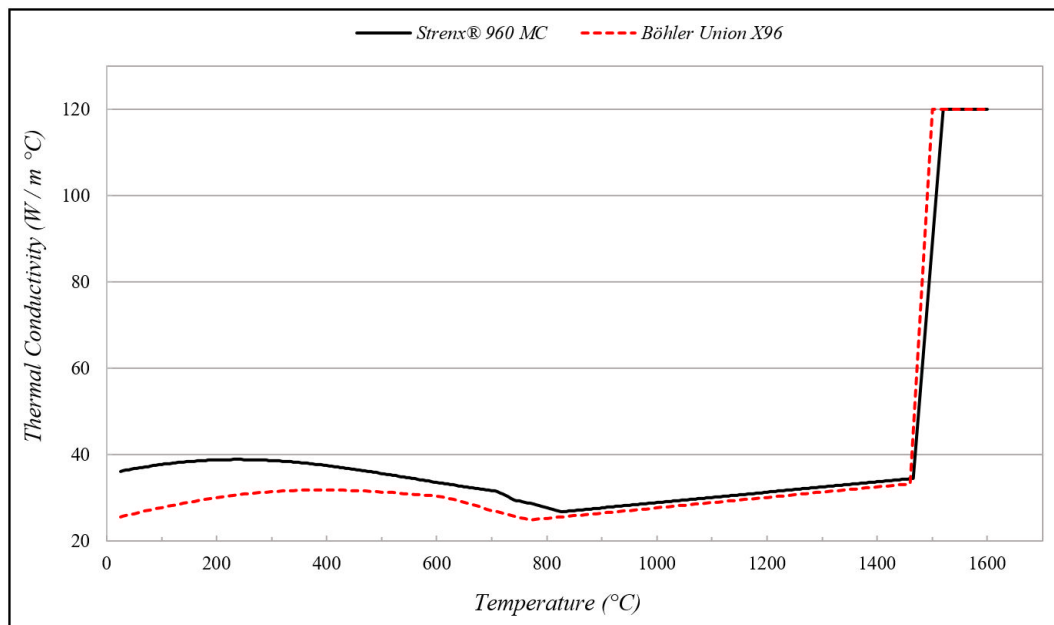


Figure 18. Temperature-dependent thermal conductivity calculated by JMatPro.

5.2.2.4 Density

In welding simulation problems, this physical property of material can be taken as temperature-independent. It was found by researchers to have negligible effect on analysis of temperature field during welding and hence was applied as a constant value of room temperature over the entire temperature spectrum in their simulations (Danis, et al., 2010; Bhatti, et al., 2015). Provided that temperature dependency of density is required, it can be postulated that density linearly falls from the ambient value as temperature proceeds towards the melting zone. It, hence, becomes stable at the density value of liquid (Hansen, 2003, p. 43). The figure 19 depicts the variation of density as a function of temperature.

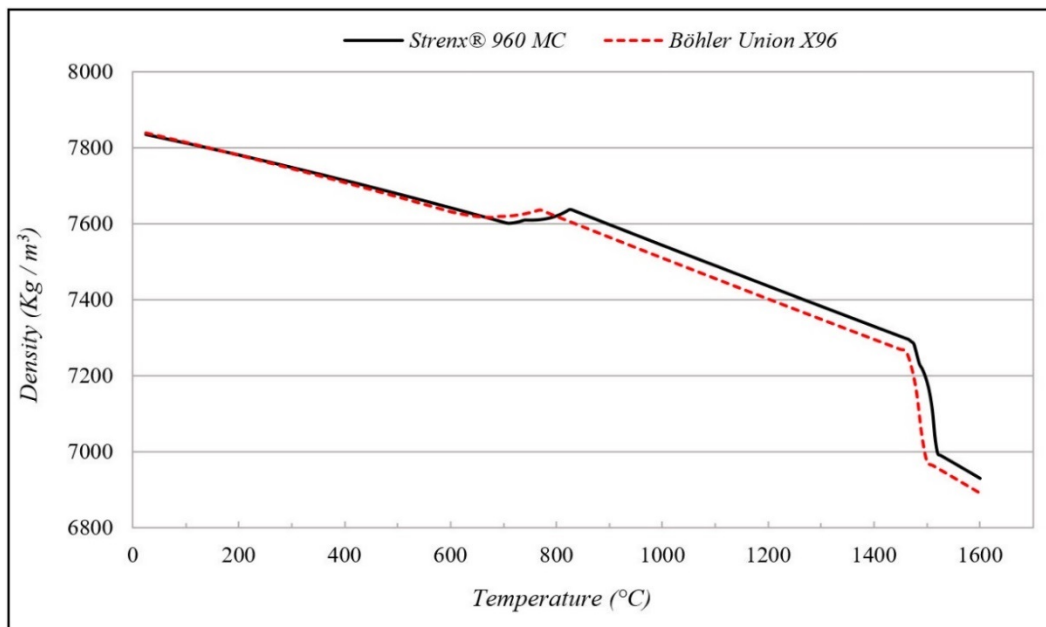


Figure 19. Density as a function of temperature calculated by JMatPro.

5.2.3 Temperature-Dependent Mechanical Properties

Mechanical properties of material are essential factors in assessing the induced residual stresses and distortions in numerical simulations of welding. These material characteristics values under the influence of nonlinearity of increased temperature and ensuing cooling and in general thermal cycle, will undergo vicissitudes through the changes that occurs in material's microstructure. Principally, mechanical properties of material which are used in assessment of residual stresses and welding deformations are yield strength, modulus of elasticity (Young's modulus), thermal expansion coefficient and Poisson's ratio. Mechanical

Properties of filler material in this study is presumed to be identical to the ones of parent material due to difficulty of obtaining those properties especially at high temperatures.

5.2.3.1 Poisson's Ratio

Applying tension or compression on steel materials, comprises both axial and transverse strains. The ratio of transverse or contraction strains to axial or expansion strains which is accompanied by a negative sign is called Poisson's ratio as is stated in the following expression:

$$\nu = -\frac{\varepsilon_y}{\varepsilon_x} \quad (35)$$

Where ν is Poisson's ratio, ε_y is lateral or transverse strain and ε_x denotes axial or longitudinal strain. A positive value for Poisson's ratio is obtained since the sign of lateral strain opposes the sign of axial strain (Dowling, 2013, p. 203). Along with Young's modulus, Poisson's ratio characterizes elastic behavior of material. In simulation of welding processes, due to unimportant effect of this material property on residual stresses, in several researches it has been therefore, considered as a constant value (Bhatti, et al., 2015; Lee & Chang, 2011). This study, however, considers temperature-dependent Poisson's ratio as is shown in the figure 20.

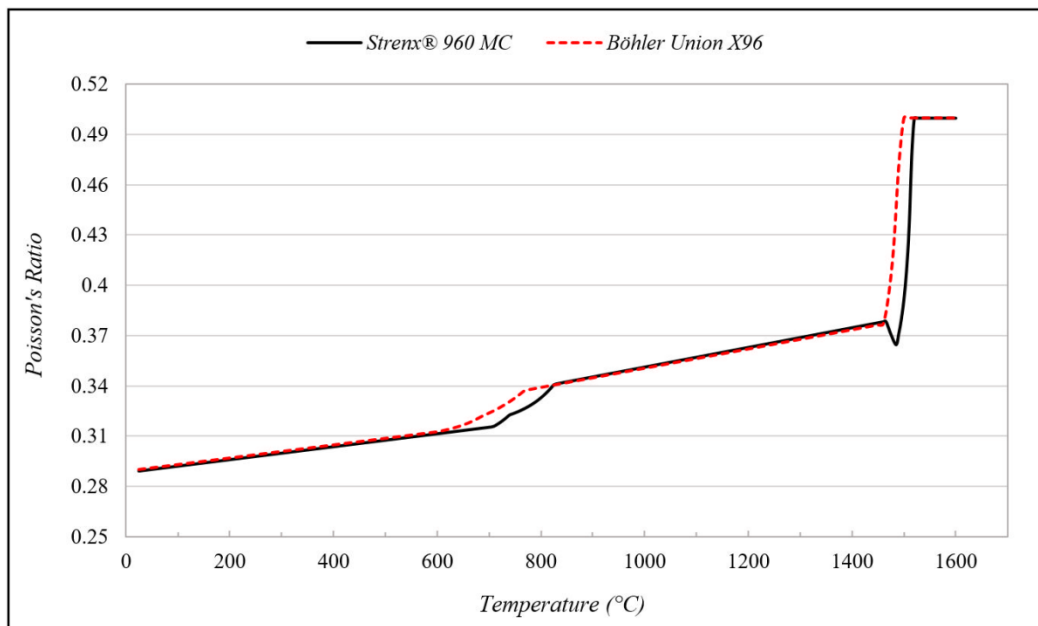


Figure 20. Poisson's ratio as a function of temperature calculated by JMatPro.

5.2.3.2 Young's Modulus

Upon loading, deformations which usually appear can be either elastic or plastic. Elastic deformation will be recovered quickly upon unloading. In elastic region, where only this deformation exists, stress and strain are proportional prior to yielding based on Hooke's law. This proportionality which is also called material's stiffness is referred to as modulus of elasticity or Young's modulus. (Dowling, 2013, p. 21) In uniaxial tensile test, this parameter is considered as the slope of stress-strain curve prior to yield limit as follows:

$$E = \frac{\sigma}{\varepsilon} \quad (36)$$

Where E is Young's modulus, σ and ε denote respectively, stress and strain in elastic region. The figure 21 shows variation of Young's modulus as a function of temperature which is obtained as the slope of stress-strain curves in elastic region from hot tensile test of standard cylindrical specimens in different temperatures. Since in each temperature, three specimens are tested, Young's modulus in the graph in each temperature is considered as the average of those three calculated values.

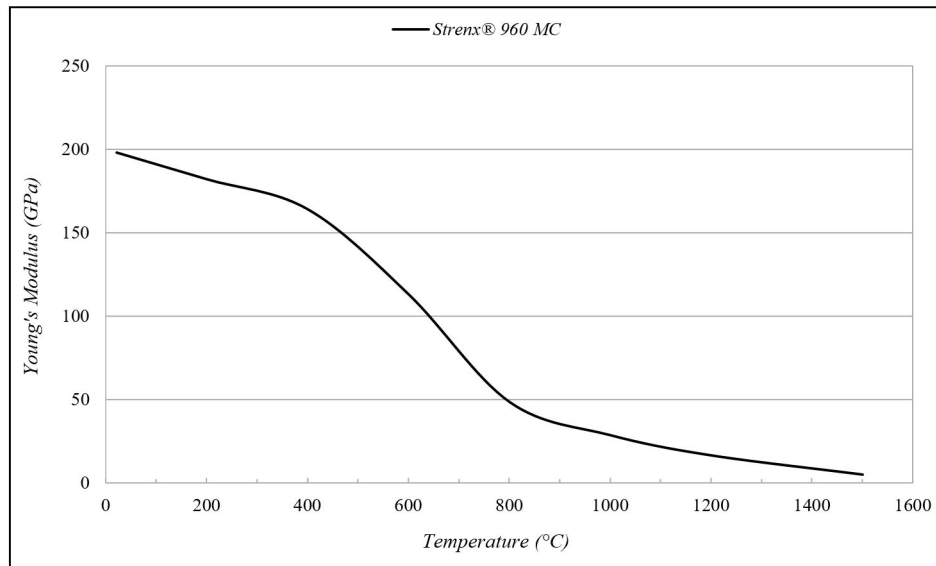


Figure 21. Experimental Young's modulus of Strenx®960 MC as a function of temperature.

5.2.3.3 Yield Strength

As previously mentioned, deformations which occur upon loading can be either elastic or plastic. Deformations which are not recovered on unloading are called plastic deformations which are permanent. The state in which this process of deformation befall and a relatively large further deformation is expected on even a small increase in stress, is called yielding and the stress value at the commencement of this behavior is so called yield strength (Dowling, 2013, p. 21). The value of yield strength can be identified with several approaches. Offset methods is one of the most widely approaches to specify yield point in which a line in stress-strain diagram is drawn parallel to the Young's modulus by an arbitrary offset distance which is commonly considered to be a strain of 0.2% or 0.002. The intersection point of this line with the engineering stress-strain curve is named offset yield strength or proof stress.

Yield strength is highly temperature-dependent, as temperature increases material softens and based on the steel type, a considerable diminish of yield strength is observable at higher temperatures and eventually vanishes at melting temperature. Since yield strength is a deciding factor whether material behaves elastically or plastically, it is of considerable importance to have temperature-dependent values of this material property in welding simulation problems.

In this study, elasto-plastic characteristics of material are obtained through conducting tensile test at room temperature and hot tensile tests in the range of 200-1200 °C. Laser cut specimens were machined to meet the dimensional requirements of standardized cylindrical tensile test specimens based on ASTM-E8M-04. Schematic geometry of tensile test specimens is depicted in the figure 22.

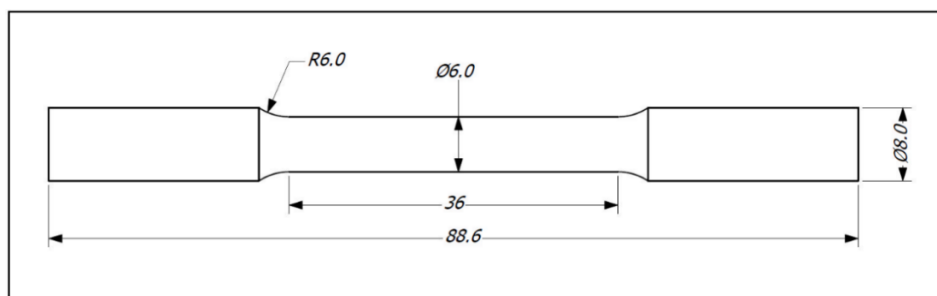


Figure 22. Geometry of tensile test specimen (Dimensions in mm).

Tensile tests were carried out in Zwick / Roell Z100 testing machine for tensile tests at elevated temperatures as well as room temperature. To perform hot tensile tests, specimens were heated up inside the oven up to the desired temperature and then were loaded to accomplish the tensile test. In order to ensure reliable results, strain rates of the experiments were chosen 0.00007 / s and 0.00025 / s for temperatures up to 600 °C and 0.0014 / s for temperatures above 600 °C . At each temperature, three specimens were tested to assure reliable results for elasto-plastic properties of material.

The output of the testing machine reflects engineering stress and strain data which should be transformed into true stress and strain to be applicable in property module in ABAQUS concerning the material plasticity in structural analysis. Making use of the following equation, engineering strain is related to true strain (Dowling, 2013, p. 144):

$$\tilde{\varepsilon} = Ln (1 + \varepsilon) \quad (37)$$

And likewise for true and engineering stress:

$$\tilde{\sigma} = \sigma \times (1 + \varepsilon) \quad (38)$$

Where $\tilde{\varepsilon}$ and $\tilde{\sigma}$ are respectively, true strain and stress and corresponding engineering strain and stress are shown with ε and σ , respectively. The figure 23 shows experimental temperature-dependent yield strength of the parent material.

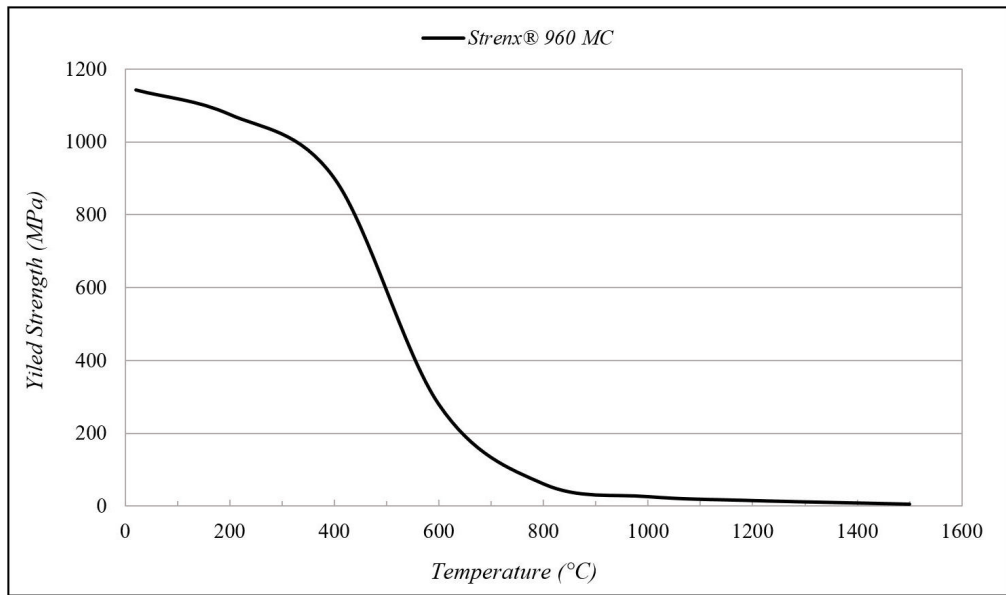


Figure 23. Experimental Temperature-dependent yield strength of Strenx®960 MC.

5.2.3.4 Thermal Expansion Coefficient

When an unconstrained steel body is exposed to an environment with increasing temperature, it expands and contraction will happen when temperature decreases. Such behavior is known as thermal dilatation and the relation between expansion and temperature is expressed through defining thermal expansion coefficient which can be either linear or volumetric corresponding to linear and volumetric expansion. (Hansen, 2003, pp. 48-49)

Thermal strain can be obtained using the following expression:

$$\varepsilon^{th} = \int_{T_2}^{T_1} \alpha(T) d(T) \quad (39)$$

Where ε^{th} is thermal strain and $\alpha(T)$ denotes temperature-dependent thermal expansion coefficient. In general, thermal expansion increases as temperatures rises until A_1 temperature where phase change happens and in the case of HSLA steels, material phase(s) transform(s) to austenite with higher atomic packing factor leading to a drop in thermal expansion. As soon as austenite transformation is completed and material is fully austenitized at A_3 temperature, thermal expansion coefficient begins to climb up as temperature increases. During the cooling stage, due to contraction, decrease in thermal expansion coefficient continues until the formation of martensite, when decomposition of

austenite into martensite causes a volume increase which gives rise to thermal expansion coefficient. Application of thermal expansion coefficient in simulation of welding in the present study, is accomplished developing a user subroutine in ABAQUS which will be discussed further in more details.

5.3 Transient Thermal FE Modeling

As previously mentioned, thermal analysis in ABAQUS is accomplished upon solving three-dimensional heat conduction equations for a moving heat source using temperature dependent thermo-physical properties of material explained previously in the section 5.2.2. Arc energy transmitted to parent and filler materials in this study, is modelled considering a volumetric heat flux by applying Goldak's double ellipsoidal heat source model. Welding process is generally comprised of heating stage during which temperature of material is increased to melting point and then cooling stage in which heat source is removed and material's temperature drops down to the ambient temperature.

5.3.1 Modeling of Thermal Load

Introduction the body heat flux was performed developing ABAQUS user subroutine DFLUX in FORTRAN programming language in which equations (40) and (41) are implemented. As a function of introduced welding speed, time and reference coordinates, local coordinates of the heat source are calculated by DFLUX. At each integration point, DFLUX is called to calculate volumetric heat flux as a function of weld pool dimensions and heat input per unit time.

Referring to the equation (21) and choosing Y -axis as welding direction in this study, volumetric heat flux for the front half of the heat source can be re-written in the following form:

$$\begin{cases} q''(x, y, z, t) = \frac{6\sqrt{3}f_f Q}{ab_f c \pi \sqrt{\pi}} e^{\frac{-3x^2}{a^2}} e^{\frac{-3[y-vt-y_0]^2}{b_f^2}} e^{\frac{-3z^2}{c^2}} \\ y \geq 0 \end{cases} \quad (40)$$

Likewise for the rear half using the equation (22):

$$\begin{cases} q''(x, y, z, t) = \frac{6\sqrt{3}f_r Q}{ab_r c \pi \sqrt{\pi}} e^{-\frac{3x^2}{a^2}} e^{-\frac{3[y-vt-y_0]^2}{b_r^2}} e^{-\frac{3z^2}{c^2}} \\ y < 0 \end{cases} \quad (41)$$

It is stated that arc power or heat input transmitted to material can be divided into two portions. One is heat of metal droplets and the other one is heat of arc. They can be partitioned to reach a better agreement between numerically simulated weld pool dimensions as well as temperature distribution and experimentally obtained ones (Pardo & Weckman, 1989). A value of 40% for arc heat and 60% for heat of droplets have been commonly used by researchers (Deng & Murakawa, 2006b; Lee & Chang, 2011; Pardo & Weckman, 1989) in terms of power allocation which was similarly found in this study to result in a suitable match of temperature histories and weld pool shape with experiment.

Characteristics parameters of the weld puddle namely a , b_f , b_r and c were initially obtained from the photomacrograph of weld cross-section and weld pool boundaries dimensioning as is suggested by Goldak & Akhlaghi (2005, p. 34) to have a rough estimation of these parameters. Forasmuch as accurate modeling of heat source is of paramount importance in prediction of residual stresses and distortions, calibration of the heat source mathematical model, comes to play a vital role.

The first issue in calibration of heat source model, is to adjust Goldak's weld pool characteristics parameters to compare temperatures extracted from the thermocouples attached on specific point on the test piece versus the corresponding nodes in FE mesh. The second matter is that simulated weld pool and bead shapes and boundaries of FZ and HAZ conform as accurate as possible to those experimentally observed and measured from micrographic examination of weld cross-section.

In order to predict temperature distribution in heating and cooling stages more precisely, several points on top as well as bottom surfaces were considered to be compared with experimental measurements. Adjusted characteristics parameters of Goldak's model reflected the most accurate results in terms of temperature histories, are shown in the table 7.

Table 7. Goldak's parameters in FE model

a [m]	b_f [m]	b_r [m]	c [m]	f_f	f_r
0.0046	0.005	0.011	0.004	0.62	1.38

In welding simulation studies, steel materials are generally considered as isotropic materials. The term isotropy connotes that material properties at a special point are identical in all directions. Provided that direction-dependent properties are exhibited by materials, they are addressed to as anisotropic materials. Materials with three mutually orthogonal planes of symmetry with regards to their properties are called orthotropic or orthogonally anisotropic materials. They are categorized as a subset of anisotropic materials because their properties show dependency on direction along which they are measured. (Ventsel & Krauthammer, 2001, p. 197)

Physical, electrical and particularly, mechanical properties of materials are highly dependent on their microstructures (Callister, 2000, p. 284). Grain size among the microstructural characteristics plays a major role in the abovementioned material properties. If in polycrystalline materials, crystals have a preferred crystallographic orientation, they are called textured materials. Development of anisotropy in mechanical properties of steels has been stated to be significantly under the influence of this inherent material property. (Chakrabarti, et al., 2007)

In the context of mechanical properties, it is of particular importance to draw a relation between mechanical behavior and the nature of dislocations, their density and motion (Suryanarayana, 2012). The higher the dislocation density, the more pronounced the resistance of dislocation movement by other dislocations and as a result, the necessary stress to make plastic deformation increases. In between, the effect of grain size needs to be taken into consideration. That is, a microstructure with smaller grain size, implies that the total grain boundary area is larger compared to the one with coarse grains. Grain boundaries act as barriers and impede the motion of dislocations. (Callister, 2000, pp. 206-207)

It is stated that rolled steel sheets display orthotropic behavior (Lauwagie, et al., 2003). Production method of steels can cause changes in spatial organization and size of grains in different directions and consequently imposes anisotropy. The mechanism is not discussed here but it is considered as known a priori.

Regarding the physical properties, in a study by Jonšta et al. (2015), it was found that heat transfer is facilitated in coarse-grained steels due to existence of smaller grain boundary area. Higher thermal conductivity was resulted as a consequence of increasing the grain size and subsequent decrease in grain boundaries which means less barrier in heat conduction through the grains. Specific heat, on the other hand, remained virtually unchanged in their experiments.

Austenite morphologies of the investigated material in rolling direction (RD), Transverse direction (TD) and normal direction (ND) are shown in the figure 24.

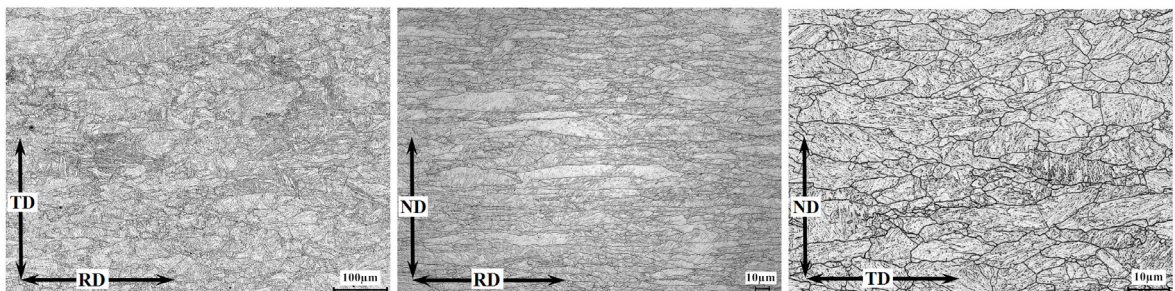


Figure 24. Prior-austenite grain structure of Strenx[®]960 MC.

From the figure above, grain refinement in section RD-ND in normal (through thickness) direction is observable. Grains are elongated in RD while very well compressed in ND. A similar trend in section TD-ND is recognizable where grain size is larger in TD compared to the one in ND. Prior-austenite grain sizes were measured in RD, TD and ND which are approximately $61\ \mu\text{m}$, $50.5\ \mu\text{m}$ and $11\ \mu\text{m}$, respectively. In fact, smaller grain size in ND implies higher number of barriers which incorporate in weaker heat transportation in through thickness direction compared to the RD or TD which imposes anisotropy to properties of this hot rolled UHSS.

This study tries to take into consideration the anisotropic nature of the material by applying various thermal conductivities in different directions for the parent material. Concerning this matter, parent material was defined as an anisotropic material and owing to the lack of experimental data regarding the anisotropic thermal conductivity, artificially decreased thermal conductivity values were assigned to the whole temperature ranges below the solidus temperature in thickness direction.

With respect to conductivity in the welding direction (transverse to rolling direction), inasmuch as grains in rolling and transverse directions, obtained approximately the same sizes, identical temperature-dependent thermal conductivity (as was presented in the figure 18) to which were assigned. Iteration method was adopted to calibrate through thickness values so that outputs of the simulation demonstrate temperature histories with close agreement to the experimental ones.

5.3.2 Modeling of Heat Loss

Nonlinearity of heat transfer problems are generally associated with temperature-dependent material properties especially when latent heat effects are concerned as well as thermal boundary conditions due to the nature of heat transfer coefficient which is also temperature-dependent.

Heat losses in this study were modelled taking into account both convection and radiation. ABAQUS user subroutine FILM was developed to model the heat loss during welding by involving the combined effect of radiation and convection which is represented via the two following equations frequently used by researchers (Deng & Murakawa, 2006a; Yaghi, et al., 2006; Brickstad & Josefson, 1998):

$$h = \begin{cases} 0.0668 \times T \left(\frac{W}{m^2 \cdot ^\circ C} \right) & 0 \leq T \leq 500 \\ 0.231 \times T - 82.1 \left(\frac{W}{m^2 \cdot ^\circ C} \right) & T \geq 500 \end{cases} \quad (42)$$

Where h denotes temperature-dependent heat transfer coefficient. Inside the FORTRAN code, a sink temperature was also defined which represents the ambient temperature. The

above equations were applied on all the surfaces that are anticipated to have heat exchange with the air. It is obvious that symmetry plane of the weld is excluded since there is no contact between this surface and the surrounding environment.

5.3.3 “Model Change” Technique

Modeling the gradual deposition of filler material and step-by-step building-up the weld geometry during welding is referred to as element birth and death technique. Element birth was employed by Brickstad & Josefson (1998) allocating a high softening temperature to the elements which are not yet activated and as a result, they gain very low yield stress and stiffness. They, thus, become strain free elements holding low stresses when they are activated.

Application of this approach makes it feasible to model the weld beads laying on the parent material without any strain mismatch due to a build-up stress at nodes connecting undeformed filler material and previously deformed base material (Yaghi, et al., 2005). Element birth and death technique in ABAQUS is facilitated through “Model Change” option as an interaction, inasmuch as activation and deactivation of elements during the welding in their corresponding steps are available which makes it convenient to track the position of moving heat source and hold an update regarding the status of filler metal whether it is deposited or not (Lee & Chang, 2011).

Prior to thermal analysis, the model with all the elements representing filler material is active. In the first step, all the filler material elements are deactivated representing the situation in which the weld beads are not laid. In thermal analysis, by deactivating an element, a thermal conductivity equivalent to zero is automatically assigned to that element (Yaghi, et al., 2006). In the upcoming steps, a part of the FE mesh demonstrating the fragment of weld bead (to be deposited at its corresponding time step) is reactivated. By element activation, thermal conductivity is boosted from the zero value to that of the material defined in material properties.

In this study, the weld metal part was divided into 200 pieces via partitioning and consequently 200 steps were defined in each, a fragment of weld metal was activated. Considering the length of weld seam and welding speed, each portion corresponds to a

welding time of 0.2 second. The higher the number of time steps, the smaller the deposition time and the more realistic the simulation, while an increased analysis time due to a larger number of elements in FE mesh is expected and hence, an optimization criterion regarding the required accuracy and computational power should be adopted.

At the inception of thermal analysis, element deactivation was carried out using the following command in the ABAQUS input file for the first step:

```
*Model Change, Type=Element, Remove
```

Reactivation of the elements was commenced from the second step until the laying the last fragment of the filler material, each in its corresponding step via applying the following command in ABAQUS input file in all the steps that element reactivation is supposed to be fulfilled:

```
*Model Change, Type=Element, Add
```

It is also possible to apply element birth and death in ABAQUS through interaction menu and creating “Model Change” interaction (which has the same functionality as the aforementioned command) and apply deactivation and then reactivation to the specified elements. Using this method, elements are activated as strain free elements. The interested reader is referred to useful articles by Lindgren (2001a) and Yaghi et al. (2005) to gain a deeper understanding regarding the concept of element birth and death in finite element analysis.

5.3.4 Element Type in Thermal Analysis

In the context of element order suitable for welding simulations, Lindgren (2001a) explains that it is generally more favorable to have a finer mesh grid with low-order elements compared to a coarser mesh including higher-order elements. Nevertheless, both linear and quadratic elements have been used in welding simulation problems by different researchers. In the case of three-dimensional modeling, Deng (2009), Deng & Murakawa (2006a), Lee & Chang (2009) and Danis et al. (2010) used eight-node linear brick elements for both thermal and mechanical analyses while Shan et al. (2009) applied quadratic brick elements

each with 20 nodes in heat transfer as well as in mechanical analysis. Ahn et al. (2017) on the other hand, employed quadratic and linear brick elements, respectively in thermal and mechanical analysis.

Thermal analysis in this investigation was conducted using linear hexahedral eight-node three-dimensional continuum diffusive heat transfer elements (DC3D8) with temperature as the only degree of freedom at each node. Application of first order diffusive elements owing to their special integration approach are recommended to give solution to heat transfer analyses incorporating latent heat effects, as has been involved in this study, whereas second order elements are suitable when latent heat effects are negligible and thus, solution will be smooth (ABAQUS, 2017).

5.4 Mechanical FE Modeling

Mechanical analysis was performed reading the temperature history obtained as the result of the solving the heat conduction equations upon the completion of thermal analysis. Temperature field was used as thermal load in predefined field in ABAQUS in mechanical analysis. An FE mesh identical to the one used in thermal analysis was applied in mechanical analysis in order to avoid mesh incompatibilities and convenient data transferring and mapping between the two analyses. Nonetheless, the element type and boundary conditions employed in mechanical analysis, differ from to the ones applied in heat transfer analysis which will be discussed in the following sections.

5.4.1 Element Type in Mechanical Analysis

First order reduced integration hexahedral three-dimensional continuum elements (C3D8R) with three translational degrees of freedom at each node were used in mechanical analysis. A better convergence is supposed to be achieved and excessive locking is prohibited during mechanical analysis using reduced integration elements (Lee & Chang, 2011). Selection of reduced integration versus full integration elements accounts also for a smaller computational cost, however in the case of C3D8R, due to owning only one integration point, hourglassing problem might occur in which distortion of element happens in the way that uncontrolled mesh distortion might be resulted. It is recommended to use first order reduced integration in a sufficiently fine mesh even though hourglass control is included in first order reduced integration elements in ABAQUS. (ABAQUS, 2017)

5.4.2 Mechanical Boundary Conditions

Boundary conditions in mechanical analysis was applied to only prevent rigid body motion and realistically simulate the welding condition in which no special clamping and fixture were employed. That is, the symmetry plane is restricted in X - direction. Point A , The first node lying on welding centerline on the top plate is constrained in Y and Z -directions and the last point on the welding centerline, point B , is restricted to move in Z -direction as is shown in the figure 25.

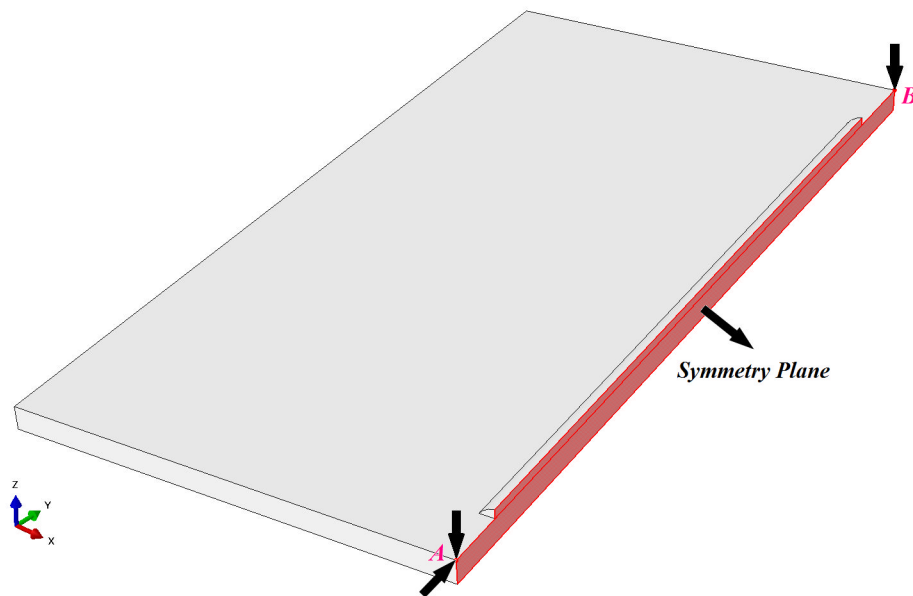


Figure 25. Applied boundary conditions in structural analysis.

5.4.3 Mechanical Aspect of “Model Change”

Analogous to activation / deactivation of elements representing the continues deposition of filler material in thermal analysis, “Model Change” technique, in mechanical analysis, assigns a drastically decreased value of stiffness to the elements that are deactivated corresponding to the condition that heat source has not yet reached a certain point and filler material that is not yet laid in a given time (Lee & Chang, 2011).

As soon as the welding torch approaches and filler material is melted and deposited, status of corresponding elements are changed from deactivated to reactivated to which temperature-dependent mechanical properties are allocated and the value of stiffness is altered from that reduced one to that of the material. As mentioned before, these elements are reactivated as strain free elements without any strain history record which avoids the

model to suffer from any build-up stress during step change and consequently elements are brought into existence without entailing any strain incompatibilities.

5.4.4 Strain Decomposition

In order to calculate residual stresses in welding simulation problems, the total deformation should be determined. During a non-linear FE analysis, total strain increment is obtained from incremental displacements (Lindgren, 2001b). Using the infinitesimal strain theory, decomposition of total strain rate is expressed in following equation:

$$\dot{\epsilon}^{total} = \dot{\epsilon}^e + \dot{\epsilon}^p + \dot{\epsilon}^{th} + \dot{\epsilon}^{AV} + \dot{\epsilon}^{trp} + \dot{\epsilon}^{vp} + \dot{\epsilon}^c \quad (43)$$

Where $\dot{\epsilon}_{total}$ is the total strain rate of the material undergoes welding $\dot{\epsilon}^e$, $\dot{\epsilon}^p$, $\dot{\epsilon}^{th}$, $\dot{\epsilon}^{AV}$, $\dot{\epsilon}^{trp}$, $\dot{\epsilon}^{vp}$ and $\dot{\epsilon}^c$ are respectively, elastic, plastic, thermal (originated by thermal expansion), volumetric change, transformation plasticity, viscoplastic and creep strain components. It is stated that elastic, thermal and inelastic strain components in order to predict welding-induced residual stresses, have to be taken into consideration (Lindgren, 2001b). However, investigating the strain components caused by creep, transformation plasticity and viscoplasticity are out of the scope of this thesis and hence, are neglected in calculations. Ignoring the three mentioned strain rate components, the equation (43) can be simplified as follows:

$$\dot{\epsilon}^{total} = \dot{\epsilon}^e + \dot{\epsilon}^p + \dot{\epsilon}^{th} + \dot{\epsilon}^{AV} \quad (44)$$

This study accounts for phase transformation and thus, strain rate imposed by volume change due to phase transformation is included in the calculations to study the effect of SSPT on welding residual stresses and distortions of the material under investigation.

Lindgren (2001b) discusses that in FE analyses of welding simulations, mechanical analysis contains more nonlinearity compared to the thermal one due to mechanical behavior of materials especially at high temperatures which incorporates in numerical problems and therefore, it is recommended that analysis should contain temperature dependencies of mechanical properties.

5.4.4.1 Elastic Strain Component

Elastic strain component is calculated employing temperature-dependent Poisson's ratio and Young's modulus and generalized Hooke's law for isotropic elastic material as follows:

$$\sigma_{ij} = C_{ijkl}\varepsilon_{kl} \quad (i, j, k, l = 1, 2, 3) \quad (45)$$

Where C_{ijkl} denotes the fourth order stiffness tensor. σ_{ij} and ε_{kl} , are second order stress and strain tensors, respectively. Inverting the generalized Hooke's law, elastic strain component can be expressed as a function of stress by the following equation:

$$\varepsilon_{ij}^e = \frac{1}{E} [(1 + \nu)\sigma_{ij} - \nu\sigma_{kk}\delta_{ij}] \quad (46)$$

Where δ_{ij} is Kronecker delta, E is modulus of elasticity and ν is Poisson's ratio.

5.4.4.2 Plastic Strain Component

Plastic strain component is modeled using temperature-dependent mechanical properties (Yield stress is assumed to be rate-independent and is contingent upon plastic strain and temperature) with Von Mises yield surface and isotropic hardening features as is demonstrated in incremental form (Lindgren, 2001b; Zhu & Chao, 2002):

$$\varepsilon_{ij}^p = \lambda' \frac{\partial f}{\partial \sigma_{ij}} = \lambda s_{ij} \quad (47)$$

Where λ signifies the plastic flow factor and is equal to zero for elastic deformation. f is the yield function and is defined as:

$$f = \bar{\sigma} - \sigma_y \quad (48)$$

Where $\bar{\sigma}$ and σ_y denote effective Von Mises stress and yield stress, respectively. $\bar{\sigma}$ is calculated by the following equation:

$$\bar{\sigma} = \sqrt{\frac{3}{2}(s_{ij}s_{ij})} \quad (49)$$

Where s_{ij} denotes the deviatoric stress and is calculated by subtracting the hydrostatic stress tensor from the total stress tensor:

$$s_{ij} = \sigma_{ij} - \frac{1}{3} \sigma_{kk} \delta_{ij} \quad (50)$$

5.4.4.1 Thermal Strain Component

Thermal strain rate originated by thermal expansion can be calculated in numerical computations using temperature-dependent thermal expansion coefficient and a reference temperature as follows (Lindgren, 2001b):

$$\varepsilon^{th} = \alpha_{n+1}(T_{n+1} - T_{ref}) - \alpha_n(T_n - T_{ref}) \quad (51)$$

Where ε^{th} is the increment of thermal strain caused by thermal expansion, α is temperature-dependent thermal expansion coefficient, T is temperature and indices n , $n + 1$ and ref for T denote initial, current and reference temperatures, respectively.

5.4.5 Annealing Effect

This study considers annealing effect which is applied solely for plastic behavior of material or user-defined material model without any impact on other material properties (ABAQUS, 2017). In material science, annealing is a heat treatment process which includes exposing the material to an elevated temperature and microstructural recrystallization and recovery are permitted to occur. As a result, dislocations by previous cold working are removed and the effect of strain hardening is negated. (Callister, 2000 , p. S-124; ABAQUS, 2017)

In FE analysis, annealing process refers to simulation of stress relaxation when material is heated up to high temperatures. When temperature of a material point in model rises and exceeds a specified value called annealing temperature, the effect of prior work hardening for that point is removed and strain hardening memory is lost. Annihilation of stress and plastic strain histories in ABAQUS is accomplished by resetting the equivalent plastic strain to zero. Provided that temperature of a material point drops down below the annealing temperature during cooling, it can work harden again. (Ahn, et al., 2017; Lee & Chang, 2009)

Annealing temperature in this study was presumed 900 °C for both parent and filler materials.

5.5 Solid-State Phase Transformation

In order to include volume change strain component in calculation of total strain increment, phase transformation should be involved in the numerical model. Implementation the analysis of SSPT in computational model to predict residual stresses is generally performed using the kinetics of phase transformation and continuous cooling transformation (CCT) diagrams.

Kinetics of SSPT can be defined based on the applied mathematical models which require dilatometric data regarding the present phases during heating and cooling, transformation temperatures, linear thermal expansion coefficients of microstructural constituents as well as structural strain (full volumetric change strain) of each phase which can be determined conducting dilatometric tests. Further hardness measurements and metallographic examination of the specimens together with dilatometric data, CCT diagram representing the final fraction of phases arising from austenite decomposition during cooling, is experimentally obtained.

5.5.1 Dilatometric Test

Cylindrical specimens from Strenx[®]960 MC material were used for dilatometric tests. Full volumetric change strains were measured using Gleeble 3500-GTC thermo-mechanical simulator as is shown in the figure 26 (a). Specimens are heated by an alternating-current resistance system which applies heat equally through the cross-section. Temperature of the specimen during the test is measured continuously by a K-type thermocouple which provides signals so that feedback control of specimen temperatures can be accurately accomplished (see the figure 26 (b)). Quenching of the specimen is carried out in vacuum chamber. A dilatometer is used to measure the changes in diameter of the sample during heating and cooling stages.

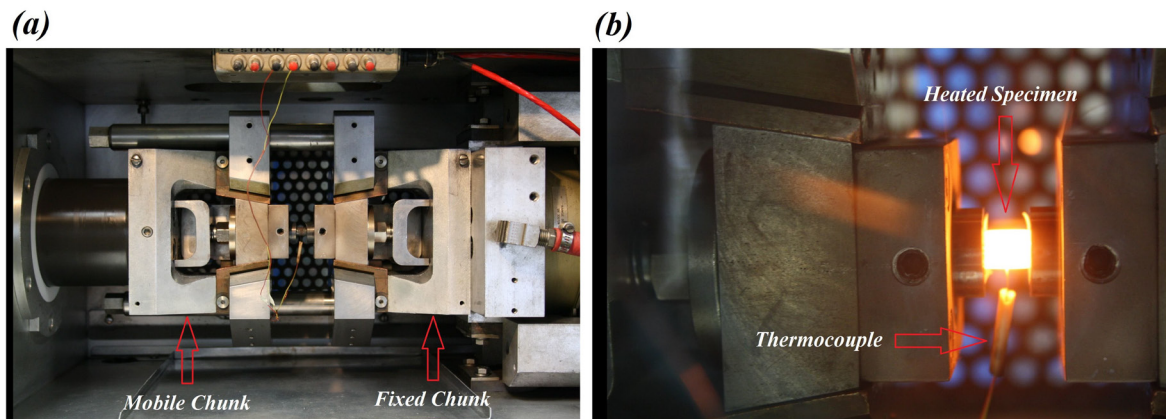


Figure 26. Dilatometric test Apparatus (a), temperature measurement of a heated sample (b).

Thermal cycle for the specimens in this study comprises heating the samples with a heating rate of $640\text{ }^{\circ}\text{C}/\text{s}$ to a peak temperature of $1350\text{ }^{\circ}\text{C}$ to ensure full austenitization at which the specimens were held for 0.1 s before cooling cycle began. A_1 and A_3 temperatures for high strength steels can be sensitive to heating rate, i.e. the mentioned temperatures can rise upon higher heating rates (Kubiak & Piekarska, 2016). Regarding the UHSS S960, Guo et al. (2015) reported that A_1 is not affected by heating rate, while A_3 arises upon greater heating rates.

Heating rate for dilatometric tests in this study was chosen to be able to consider the real situation of GMAW process in which heating rate can exceed several hundreds $^{\circ}\text{C}/\text{s}$ and consequently a high temperature for full austenitization to picture the condition where high heating rates are concerned. Heating rates higher than $640\text{ }^{\circ}\text{C}/\text{s}$ are unlikely to be experienced during GMAW process and thus, A_3 temperature during the experiment is not greater than the one obtained in dilatometric test with a heating rate of $640\text{ }^{\circ}\text{C}/\text{s}$.

Cooling cycle consists of continuous quenching the specimens with 10 different cooling rates; 5, 10, 20, 30, 40, 50, 60, 70, 80 and $90\text{ }^{\circ}\text{C}/\text{s}$. For lower cooling rates, i.e. $5 - 40\text{ }^{\circ}\text{C}/\text{s}$, specimens with 6 mm diameter and 9 mm length were used, whereas for cooling rates $50 - 90\text{ }^{\circ}\text{C}/\text{s}$, dimensions of the specimens were 5 mm and 7.5 mm , respectively for diameter and length as is depicted schematically in the figure 27.

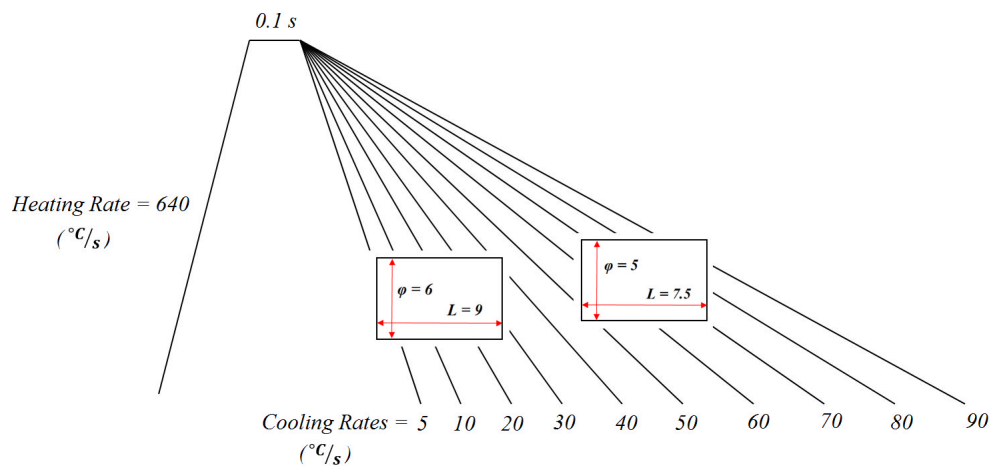


Figure 27. Schematic of heating and cooling diagram used in dilatometric tests.

It is far-fetched that during welding, test piece undergoes very slow cooling rates, nevertheless, including different cooling rates in the experiments, facilitates the study of the effect of each cooling rate on fraction of phases arising from austenite during cooling. The most probable cooling rate in HAZ, will be selected for further SSPT modeling based on the temperatures measured by thermocouples during welding and identifying cooling time in the range 800-500 °C ($t_{8/5}$) and calculating the cooling rate in the range 800-500 °C ($v_{8/5}$).

The heated and cooled specimens after dilatometric tests were machined, polished and etched using 2% Nital for hardness measurements and microstructural examinations. Hardness of each sample was measured three times using Struers Duramin-A300 hardness testing machine and the average value was considered as the hardness at the cooling rate for the specimen. Microstructural observation of the samples were carried out utilizing Keyence VK-X200 laser scanning microscope. CCT diagram of the material was determined making use of dilatometric data and hardness measurement. Fraction of phases extracted from metallographic photos pertinent to each cooling rate.

5.5.2 Phase Transformation kinetics models

Thermal cycles during welding are addressed to as the particular contributor in occurrence of SSPT and associated volume change in steels. Volumetric change strains induced by transformation are derived from phase work hardening owing to the difference in thermal expansion coefficient of present phases. (Ahn, et al., 2017)

5.5.2.1 Austenitic Transformation Model

Base material microstructure before undergoing any thermal cycle, based on the scanning electron microscopy (SEM), as is shown in the figure 28, is assumed to be a combination of bainite and martensite.

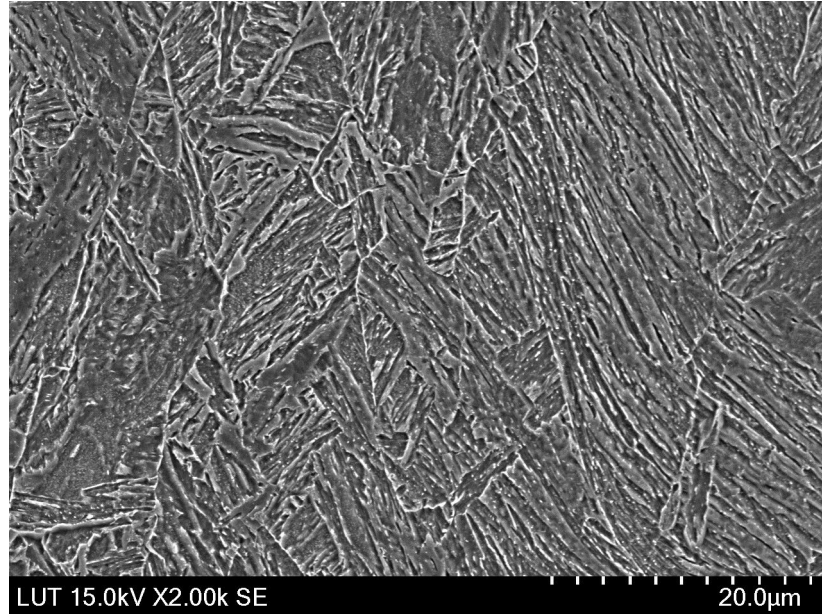


Figure 28. Scanning electron micrograph of Strenx[®]960 MC.

When material is heated up to A_1 Temperature, bainitic-martensitic microstructure begins to transform to austenite with FCC structure during which material is subjected to a decrease in its net volume. When A_3 temperature is reached, Transformation is completed and material is fully austenitic. Nonetheless, increase in the volume fraction of austenite in heating, between A_1 and A_3 temperatures, in the case of partial or incomplete austenitic transformation in the current study, is assumed to follow a linear rule as follows (Kubiak & Piekarska, 2016):

$$f_a = \frac{T_{max} - A_1}{A_3 - A_1}, \quad A_1 \leq T_{max} \leq A_3 \quad (52)$$

Where f_a denotes the fraction of austenite during austenitic transformation as a function of the maximum temperature a material point meets during heating which is indicated by T_{max} .

A_1 and A_3 temperatures might be calculated via empirical formula, however, in this study they were set to 775 °C and 863 °C correspond to A_1 and A_3 , respectively. They were

determined based on the analysis of the experimentally obtained dilatometric curve during heating and application of tangent-intersection method as was practiced by Li et al. (2016).

5.5.2.2 Diffusive Transformation Model

Fraction of phases arising from austenite during cooling process, might be obtained based on the final fraction of the specific microstructural constituent determined from CCT diagram along with starting and ending transformation temperatures of that phase, using applied diffusive transformation kinetics. The experimentally-determined CCT diagram of the base material reveals that for the concerned cooling rate, base material microstructure consists of almost 70% bainite and 30% martensite which necessitates considering diffusive transformation of austenite to bainite. The kinetics model of Machnienko for diffusive transformation has been applied in this study as was practiced by Piekarska et al. (2012). Exclusively for bainite transformation, the mentioned model is written in the following form:

$$f_b(T, t) = f_b^{\%} f_a \left[1 - \exp \left(-k_a \frac{B_s - T}{B_s - B_f} \right) \right], \quad B_f \leq T \leq B_s \quad (53)$$

Where $f_b(T, t)$ denotes the fraction of bainite during diffusive transformation as a function of T , current temperature. f_a is the fraction of austenite formed during heating and $f_b^{\%}$ is the final fraction of bainite determined based on the CCT diagram for a specific cooling rate and is set to 70% in this special case. k_a is a factor which is adjusted in the range 2.5-3. Bainite start temperature (B_s) is the temperature at which transformation of bainite from austenite with FCC structure starts involving net volume increase, whereas bainite finish temperature (B_f), corresponds to the temperature at which bainite transformation is completed.

The B_s temperature might be calculated via the proposed empirical equations, however, this study applies experimentally-determined B_s temperature for the concerned cooling rate. Table 8 presents the value of B_s temperature using some of the empirical formula along with the experimental value of B_s temperature. Based on the CCT diagram, for higher cooling rates there is no practical B_f temperature, nevertheless, in order to facilitate the calculations, it is assumed that transformation of bainite from austenite is completed when martensite transformation begins and hence, B_f temperature is considered equal to martensite start temperature (M_s).

5.5.2.3 Martensitic Transformation Model

Transformation of martensite with BCT structure from austenite with FCC crystal lattice, similar to bainite transformation, is followed by an increase in the net volume. Upon the recorded temperature history during heating process, the decision was made whether or not a particular point undergoes diffusive and / or martensitic transformation.

The amount of martensite transformed from austenite in cooling, depends highly on the martensite start temperature (M_s), which is the onset of transformation of austenite into martensite. Martensite transformation is presumed to be completed when martensite finish temperature (M_f) is met, which is the temperature at which austenite is fully transformed to martensite and below which, further cooling has no effect on the amount of the formed martensite. (Lee & Chang, 2009)

A number of empirical formula have been hitherto proposed to calculate M_s temperature; such as the one by Steven & Haynes (1956) for low alloy steels and van Bohemen (2012) for plain carbon steels, mostly based on the chemical composition of the material. In a study, Lee & Lee (2008) found that in addition to chemical composition, prior-austenite grain size has an effect on martensite formation temperature in low alloy steel and thus, in their proposed predictive equation, the influence of prior-austenite grain size number is considered, i.e. reduction in ASTM grain size number results in increasing the M_s temperature.

It was assumed that M_s temperature for base and weld metal to be identical in this thesis and hence, was experimentally obtained using the dilatometric curve during cooling process using ASTM A1033 based on which martensite start temperature can be specified as the local minimum point on dilatometric curve during cooling where austenite starts to transform to martensite and the contraction changes to expansion. A comparison between M_s temperature calculated from abovementioned formula and the one experimentally obtained, has been drawn and the results are summarized in the table 8.

Table 8. M_s and B_s temperatures based on empirical formula and experiment.

Reference	Steven & Haynes, 1956	van Bohemen, 2012	Lee & Lee, 2008	Experiment
B_s (°C)	597	605	-	520
M_s (°C)	450	455	445	460

Analogous to determining M_s temperature, it was assumed that M_f temperature is the local maximum point on dilatometric curve where expansion has approached its maximum value during cooling stage and transformation of martensite from austenite is completed which was accordingly set to 355 °C.

The fraction of transformed martensite during cooling, in temperature ranges below M_s , can be tracked using Koistinen-Marburger kinetics model as is expressed in the following formulation:

$$f_m = f_m^{\%} f_a [1 - \exp(-k_m(M_s - T))], \quad M_f \leq T \leq M_s \quad (54)$$

Where f_m denotes the fraction of martensite during martensitic transformation at T , current temperature, $f_m^{\%}$ is the final fraction of martensite obtained upon the study of the CCT diagram for the concerned cooling rate which was set a value of 30% in this scenario. Transformation evolution is characterized according to temperature by the factor k_m which is frequently considered 0.011 for carbon steels in previous researches by several researchers (Deng & Murakawa, 2006b; Lee & Chang, 2011; Yaghi, et al., 2008).

It was, however, found in an investigation by Li et al. (2015) that considering the value of 0.011 for characterization factor in the above equation for low alloy high strength steels, some errors might be resulted in the calculation of martensite fraction and thus, was optimized to a value of 0.05 which was also employed in this study.

5.5.3 Volume Change Strain

The sum of the strains due to thermal expansion and volume change is generally referred to as thermal dilatation which is a dominant factor in residual stress analysis (Lindgren, 2001a). In order to take into account the effect of volume change strain on total strain increment, this strain rate component is incorporated in thermal strain increment originated by change in linear thermal expansion coefficient which is demonstrated in the following relationship:

$$d\varepsilon^{th+\Delta V} = d\varepsilon^{th} + d\varepsilon^{\Delta V} = \sum_i \alpha_i f_i dT - \text{sign}(dT) \sum_i \varepsilon_i^{\Delta V*} df_i \quad (55)$$

Where α_i stands for linear thermal expansion coefficient of phase i which could be either austenite, bainite or martensite in this study. These values are determined by experimentation based on the dilatometric curves. f_i indicates fraction of phase i , which were determined by equations (52), (53) and (54) for austenite, bainite and martensite fractions, receptively. $\varepsilon_i^{\Delta V*}$ is full volumetric change strain of phase i corresponding to volume change strain due to full austenitic, bainitic and martensitic transformations in the current research. The derivative of the mathematical expression used to calculate the fraction of phase i is signified with df_i which is calculated as follows in incremental form for austenite phase in modeling:

$$\Delta f_a = \frac{\Delta T}{A_3 - A_1} \quad (56)$$

And likewise for bainite:

$$\Delta f_b = f_b^{\%} f_a \left(\frac{-k_a}{B_s - B_f} \right) \exp \left(-k_a \frac{B_s - T}{B_s - B_f} \right) \Delta T, \quad B_f \leq T \leq B_s \quad (57)$$

And martensite:

$$\Delta f_m = f_m^{\%} f_a (-k_m) \exp \left(-k_m (M_s - T) \right) \Delta T, \quad M_f \leq T \leq M_s \quad (58)$$

Where ΔT is the temperature increment in the above equations.

In order to calculate volume change strain for austenite transformation during heating as well as bainite and martensite transformations in cooling, full volumetric change strains concerning the three transformations should be determined. These values are adjusted experimentally in this research by analyzing the dilatometric curves during heating and cooling. Full volumetric change strains for austenite can be obtained from the dilatometric curve during heating by the following equation:

$$\varepsilon_a^{\Delta V^*} = \frac{1}{3} \left(\frac{\Delta V}{V} \right)_a \quad (59)$$

Where index a refers to the austenite phase and $\varepsilon_a^{\Delta V^*}$ denotes the full volumetric change strain due to austenite transformation. Similarly, the above equation can be rewritten for bainite and martensite as follows:

$$\varepsilon_b^{\Delta V^*} = \frac{1}{3} \left(\frac{\Delta V}{V} \right)_b \quad (60)$$

$$\varepsilon_m^{\Delta V^*} = \frac{1}{3} \left(\frac{\Delta V}{V} \right)_m \quad (61)$$

Where index b and m signify the bainite and martensite phases, respectively. $\varepsilon_b^{\Delta V^*}$ and $\varepsilon_m^{\Delta V^*}$, respectively, stand for full volumetric change strains due to bainite and martensite transformations. The experimentally-determined values for full volumetric change strains as well as linear thermal expansion coefficients for austenite, bainite and martensite phases, are summarized in the table 9.

Table 9. Thermal expansion coefficients and full volumetric change strains of Strenx[®]960 MC.

<i>Microconstituent</i>	<i>Thermal Expansion Coefficient</i> $(\alpha_i) [1/^\circ\text{C}]$		<i>Full Volumetric Change Strain</i> $(\varepsilon_i^{\Delta V^*})$	
	<i>Austenite</i>	α_a	2.44×10^{-5}	$\varepsilon_a^{\Delta V^*}$
<i>Bainite</i>	α_b	1.15×10^{-5}	$\varepsilon_b^{\Delta V^*}$	4.10×10^{-3}
<i>Martensite</i>	α_m	1.37×10^{-5}	$\varepsilon_m^{\Delta V^*}$	5.75×10^{-3}

Volume change strain during austenite transformation is less significant than bainitic and martensitic transformations in terms of influence on residual stresses inasmuch as the former, practically occurs at higher temperatures which contributes with smaller effects on stress field due to weaker mechanical properties at higher temperatures (Yaghi, et al., 2008).

Modification of thermal strain rate due to expansion in order to involve volume change strain increment, is performed through employment of “*sign*” in equation (55) which is a sign function and depends on temperature change, i.e. provided that temperature difference is positive which happens during heating, *sign* is equal to +1 and during bainitic and martensitic transformations it is equal to -1.

5.5.4 Computational SSPT in ABAQUS

In FE analysis to predict welding-induced residual stresses by ABAQUS, the SSPT kinetics during heating and cooling processes expressed in numerical format, should be implemented in numerical subroutines. To do this, USDFLD and UEXPAN user subroutines were developed to take into account the effect of phase transformation.

USDFLD user subroutine is generally utilized to define material properties at each integration point of an element as a function of field variables. ABAQUS Utility routine GETVRM inside the USDFLD is used to access material point data. That is, temperature changes between the increments are saved inside a field variable. Based on the sign of temperature change (positive during heating and negative in cooling) and maximum temperature of each integration point which was recorded by GETVRM, different scenarios are deemed and the decision is made whether or not the point has undergone transformation. For the material points underwent transformation, relevant kinetics model is applied to obtain fraction of austenite during heating and arising phases upon the austenite decomposition in cooling.

UEXPAN user subroutine is employed in applications where incremental thermal strains are defined as a function of temperature, field variables or state variables (ABAQUS, 2017). The output of USDFLD user subroutine saved in field variables and state variables are passed into the UEXPAN where mathematical expressions of phase transformation kinetics as well as modification of thermal strain increment due to thermal expansion coefficient by incorporating the volume change strain increment is implemented.

6 RESULTS AND DISCUSSION

This chapter presents the results of simulated cases versus experimental measurements in order to validate the presented FE model to simulate bead on plate welding process and assess the precision degree of the model in evaluation of temperature field, welding-induced transverse residual stresses and distortions.

6.1 Validation of the Thermal Analysis

Verification of the correctness and accuracy level of the elaborated thermo-numerical model has been performed drawing comparisons between the numerically obtained temperature field versus the experimentally captured results from the thermocouples placed on different locations on the top surface as well as the bottom surface.

Welding starts at 10 mm from the plate's edges on centerline and ends after travelling 280 mm in a straight line in a single pass bead on plate GMAW process. The figure 29 shows the temperature field during welding based on the numerical simulation. Maximum temperature calculated in the thermal analysis is 1895°C , which lies within the realistic range in practice.

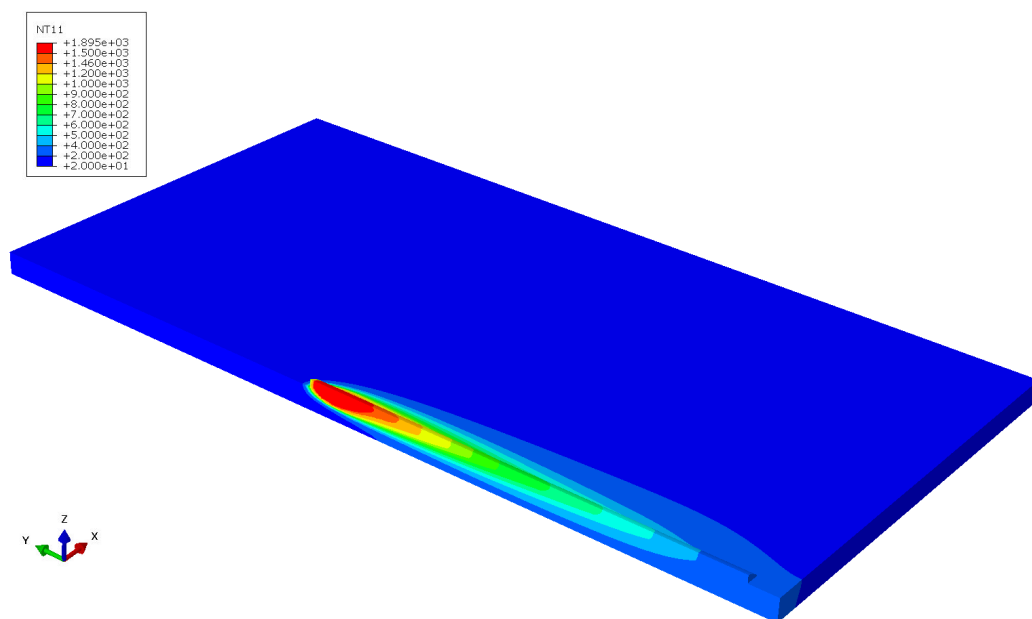


Figure 29. Predicted temperature field and thermal contours in symmetry plane.

Prediction of the shape and size of the weld pool might act as an auxiliary index of correct thermal distribution in fusion zone supplementary to temperature history records. Determining the precise weld pool shape and boundaries requires modeling the fluid flow and dynamics of weld pool which is not the concern of this study. In this regard, however, Goldak's parameters were adjusted in a realistic manner so that width of the reinforcement and depth of penetration are in close concurrence with the experimentally observed ones. A comparison between the dimensions of the fused reinforcement on top surface versus the numerically simulated one, has been drawn in the figure 30.

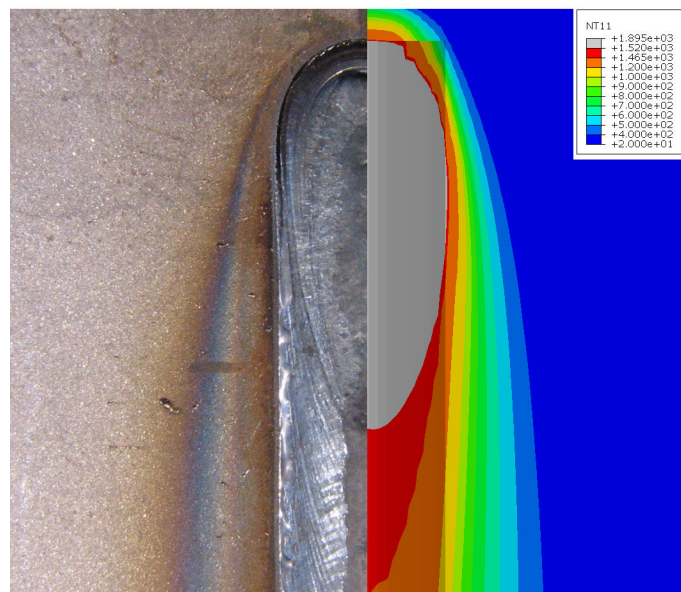


Figure 30. Boundaries of the weld pool and welding isotherms on top surface from simulation versus experiment.

Thermal cycles at specified positions measured by thermocouples in comparison with the simulation results at certain nodes which correspond to the location of thermocouples, are depicted in the figure 31 for the top surface and the figure 32 for the bottom side. Thermal cycles' curves from simulation are plotted in solid lines while the experimentally captured ones are shown in dashed lines.

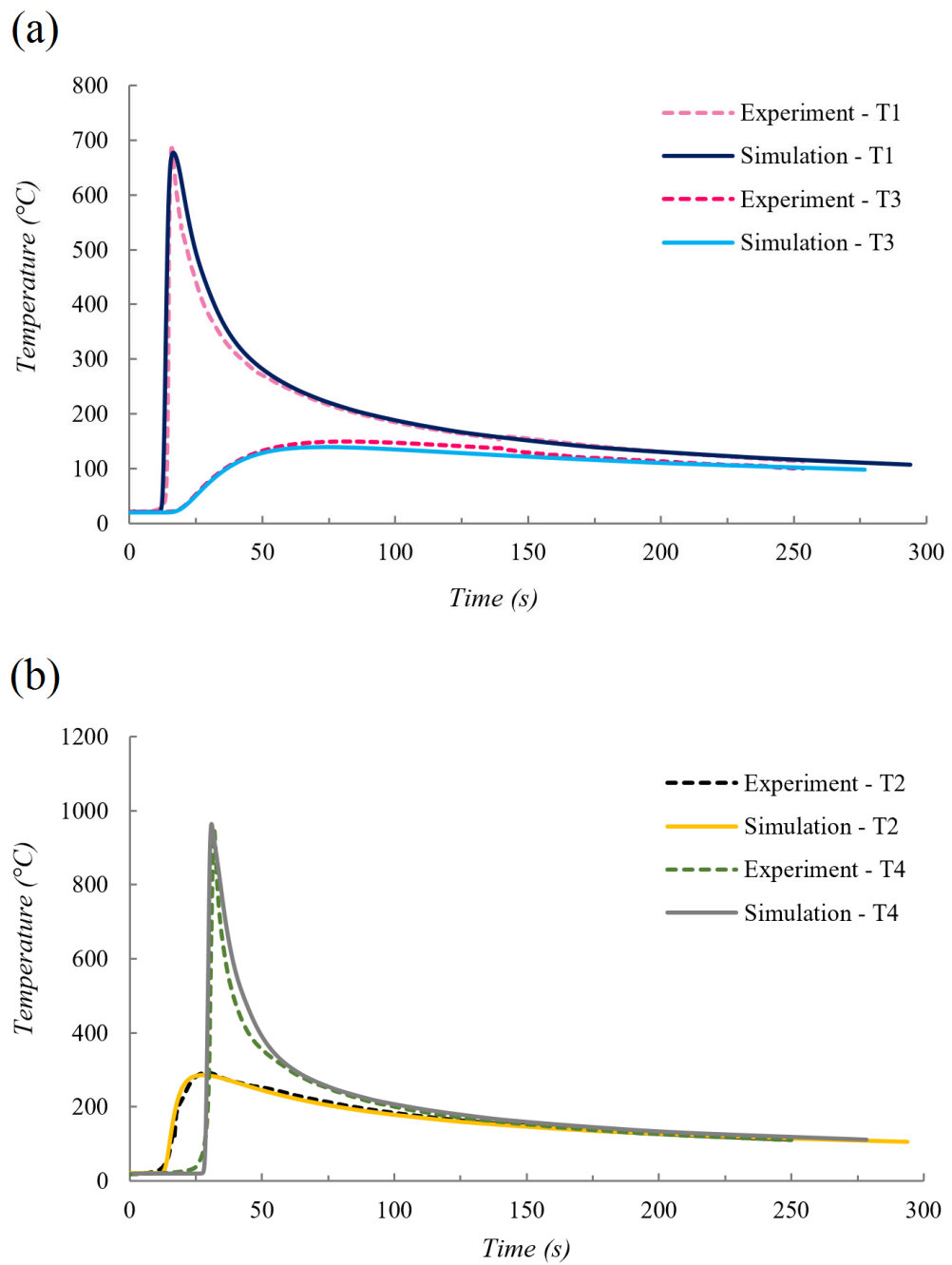


Figure 31. Predicted and measured temperature histories: locations T₁ and T₃ (a), T₂ and T₄ (b) on top surface.

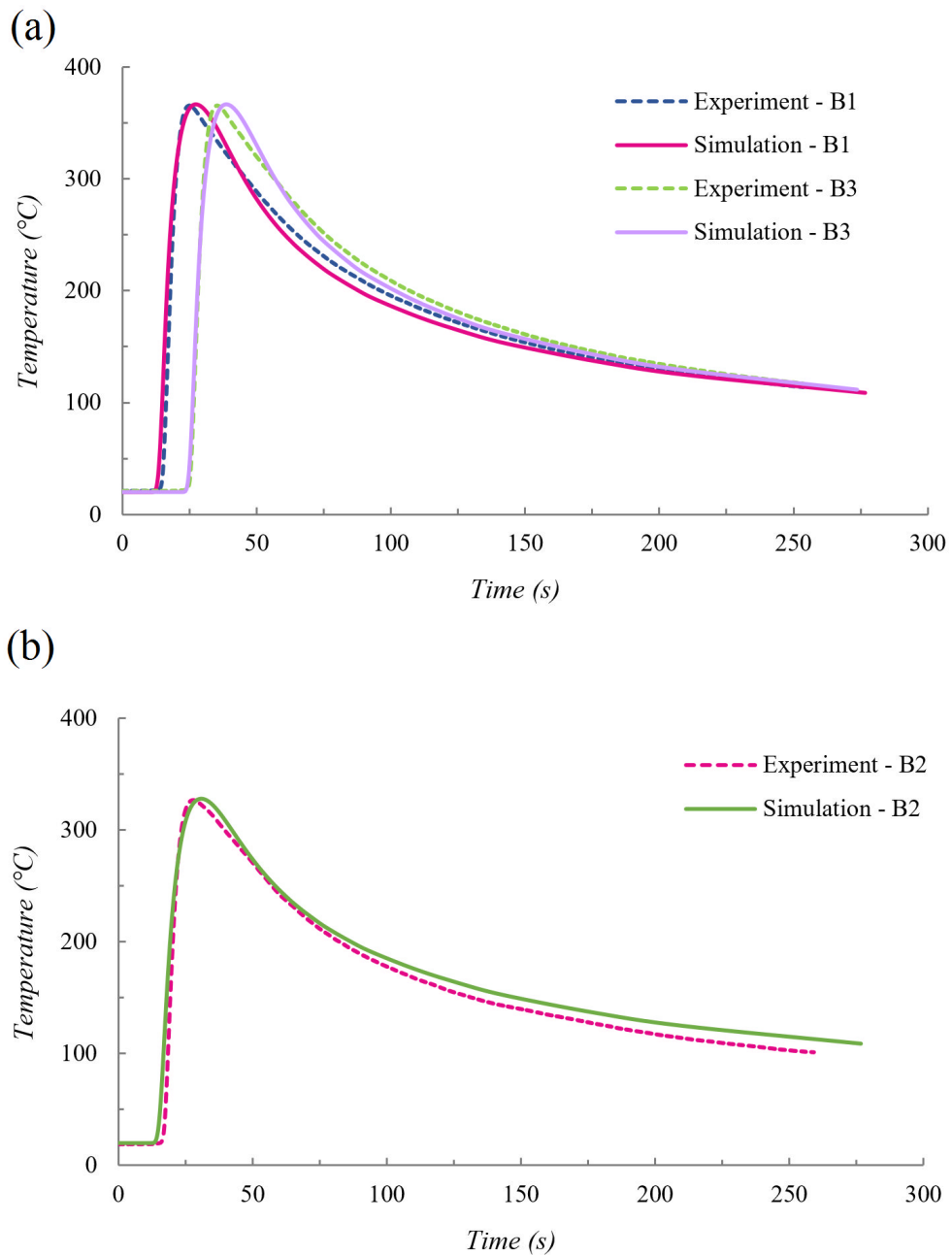


Figure 32. Predicted and measured temperature histories: locations B₁ and B₃ (a), B₂ (b) on bottom surface.

A close agreement between FE simulation and measurements in terms of peak temperature as well as cooling rate for different locations on both top and bottom surfaces, proves the accuracy of a well-defined FE model which considers anisotropic thermal conductivity in the entire temperature ranges for the investigated material which can be observed in the figures above. Such validation for temperature field, which is the most prominent measure of the correctness and precision degree of the thermo-numerical model, is the bedrock for

subsequent metallurgical and mechanical analysis which are highly contingent upon correct distribution of temperature especially in FZ and HAZ.

From the figure 31(b), $v_{8/5}$ in the HAZ can be calculated from the thermal cycle at location T4. The approximate value of $50\text{ }^{\circ}\text{C}/\text{s}$ was calculated for the $v_{8/5}$ in this study upon which, subsequent calculations regarding the fraction of phases appear upon austenite decomposition during cooling in FE analysis as well as extraction of required data from dilatometric tests and CCT diagram are accomplished.

In order to corroborate the necessity of employing the anisotropic thermal conductivity rather than the isotropic one in thermal analysis of welding process for the material under investigation and similar materials on which production process exerts alteration in size of grains in different directions, a comparison has been made between the temperature histories at the previously specified locations T1, T4, B1 and B2 predicted by two models. One of the models was developed based on the assumption of anisotropic nature of thermal conductivity, while the other one considers thermal conductivity as an isotropic material's property. The results of predictions against the experimental results for the two locations on the top surface are depicted in the figures 33 and 34. Temperature histories measured by thermocouples are shown with dashed lines while predictions of simulations running on the assumptions of anisotropic and isotropic thermal conductivity are plotted in solid and dotted lines, respectively.

It is worthy of note that in both cases, Goldak's parameters were adjusted to obtain the dimensions of fusion zone as close as possible to the experimentally measured one.

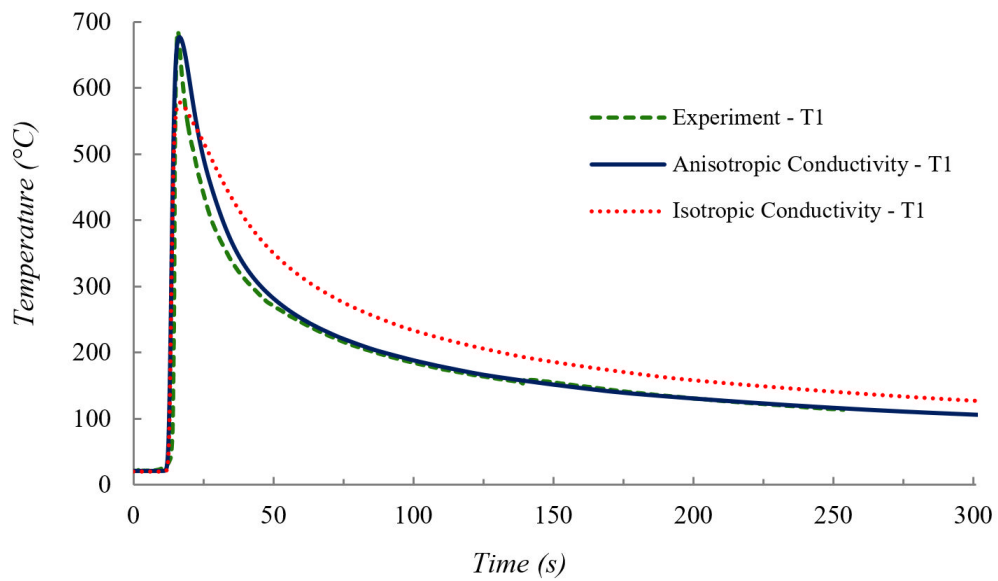


Figure 33. Predicted versus experimental temperature histories at location T_1 .

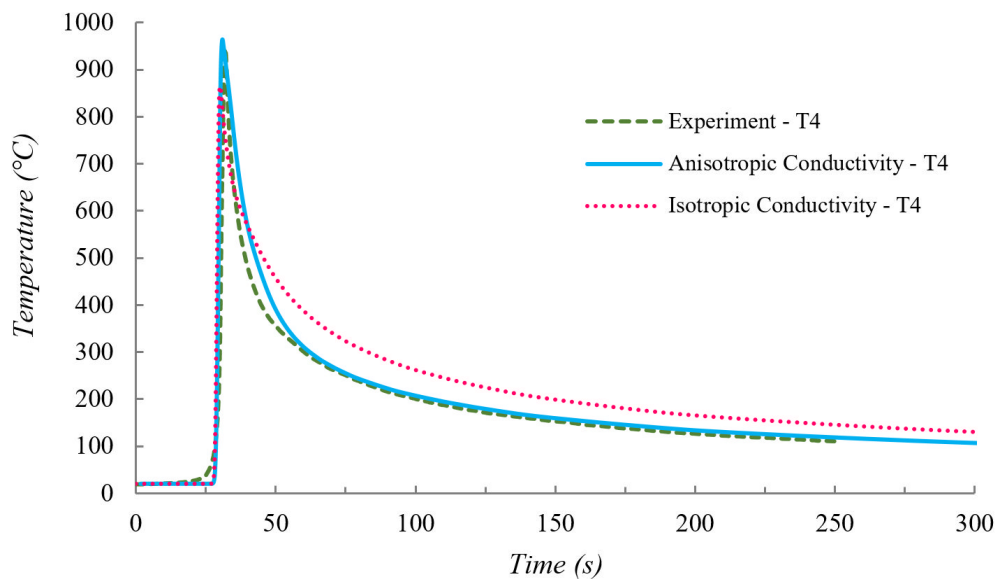


Figure 34. Predicted versus experimental temperature histories at location T_4 .

It is indubitable from the two figures that exist obvious discrepancies between the temperature histories predicted by the model which uses isotropic temperature-dependent thermal conductivity and experimental ones. That is, the peak temperatures at the two locations on top surface predicted by such model, are lower than the experimentally obtained ones. The reason might be attributed to application of the incorrect pattern of thermal conduction by the model in which the amount of energy transported in all directions are assumed to be identical while in reality, conductivity in rolling direction of material

(transverse to welding direction) due to elongated grains seems to be higher than especially in through thickness direction.

In the context of cooling rate prediction as well, slower cooling rates are resulted as a consequence of employment of isotropic thermal conductivity. It is crystal clear from thermal cycles' graphs that cooling curves of such model retain distance from the experimentally-determined ones. It is needless to mention that the model developed based on the concept of anisotropic thermal conductivity, demonstrates close agreement with experimental results in prediction of both peak temperatures and cooling rates on top surface. Likewise, for the two locations on the bottom surface, predictions of temperature histories by the two models versus experimental measurements are depicted in the figures 35 and 36 corresponding to the locations B₁ and B₂ on the bottom surface, respectively.

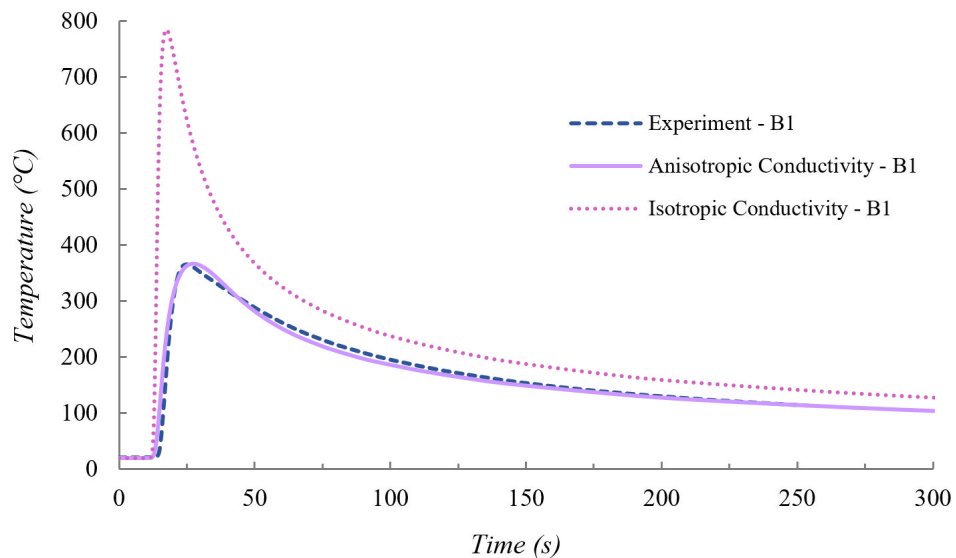


Figure 35. Simulated versus measured temperature histories at location B₁.

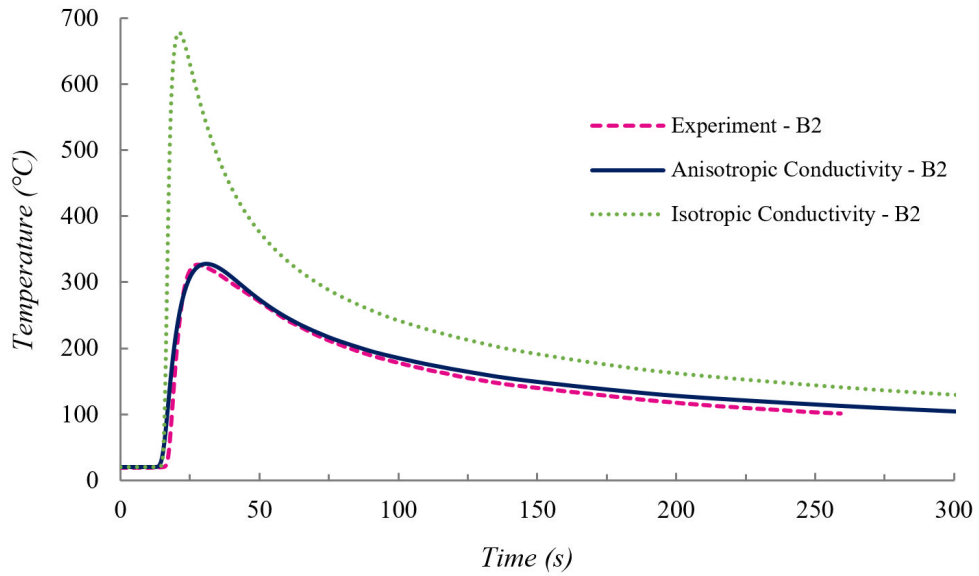


Figure 36. Simulated versus measured temperature histories at location B2.

The figures above, unequivocally demonstrate that even more dramatic discrepancies exist between the predicted thermal field by isotropic model and observed reality on the bottom side. Serious errors are involved in reflecting the heating rates, cooling rates and more importantly, peak temperatures when the model running upon the concept of isotropic conductivity is put into application for this material which proves the inability of such model to represent acceptable results with regards to prediction of the temperature histories especially at bottom surface.

Maximum temperatures at the specified locations on the bottom surface from the isotropic model are almost twice as high as the measured ones while the anisotropic model predictions meticulously agree with experiment. Higher values of thermal conductivity in the entire temperature ranges below the T_L in through thickness direction by isotropic model, gives considerable rise to the predicted temperature on the bottom surface while anisotropic model which applies reduced thermal conductivity in through thickness direction due to more barriers in transportation of heat originated from higher number of grain boundaries as a result of smaller grain size in ND, renders accurate temperature field which is closely in accordance with the experimentally-determined ones.

The importance of accuracy in determining the temperature histories is more highlighted when it pertains to evaluation of thermal field in HAZ. A close attention to the figure 34 reveals that while the location T₄ experiences temperatures higher than A₃ and is fully austenitized, as is also predicted by anisotropic model, such location is predicted to undergo incomplete austenitic transformation by isotropic model which subsequently leads to an inaccurate evaluation of the fraction of phases arising during austenite decomposition. Another relevant example in this regard, is shown in the figure 35. Based on the isotropic model, location B₁ undergoes austenitic transformation while in fact, the temperature experienced in that point is far lower than A₁ temperature and thus, no phase transformation is anticipated to occur in the mentioned location and therefore accuracy of the thermal analysis based on the assumption of isotropic conductivity for this material seems to be questionable.

6.2 Visualization of SSPT and prediction of microstructure

For the sake of simplicity, on the basis of temperature measurements, a constant $v_{8/5}$ equal to $50\text{ }^{\circ}\text{C}/\text{s}$ as is the predominant cooling rate in the HAZ of this model, in analyses regarding the prediction of microconstituents appear in HAZ and FZ was considered. Visualization of phase transformation during the bead on plate welding by implementation of the user subroutine USDFLD in ABAQUS has been performed. Austenitization and austenite disappearance as well as formation of bainite and martensite in addition to fraction of present phases as a function of time during welding at an arbitrary time of 25 seconds after start of welding is depicted in the figure 37. SDV6 was considered as austenite in the developed routine. Likewise, SDV7 denotes bainite and SDV8 implies martensite phases.

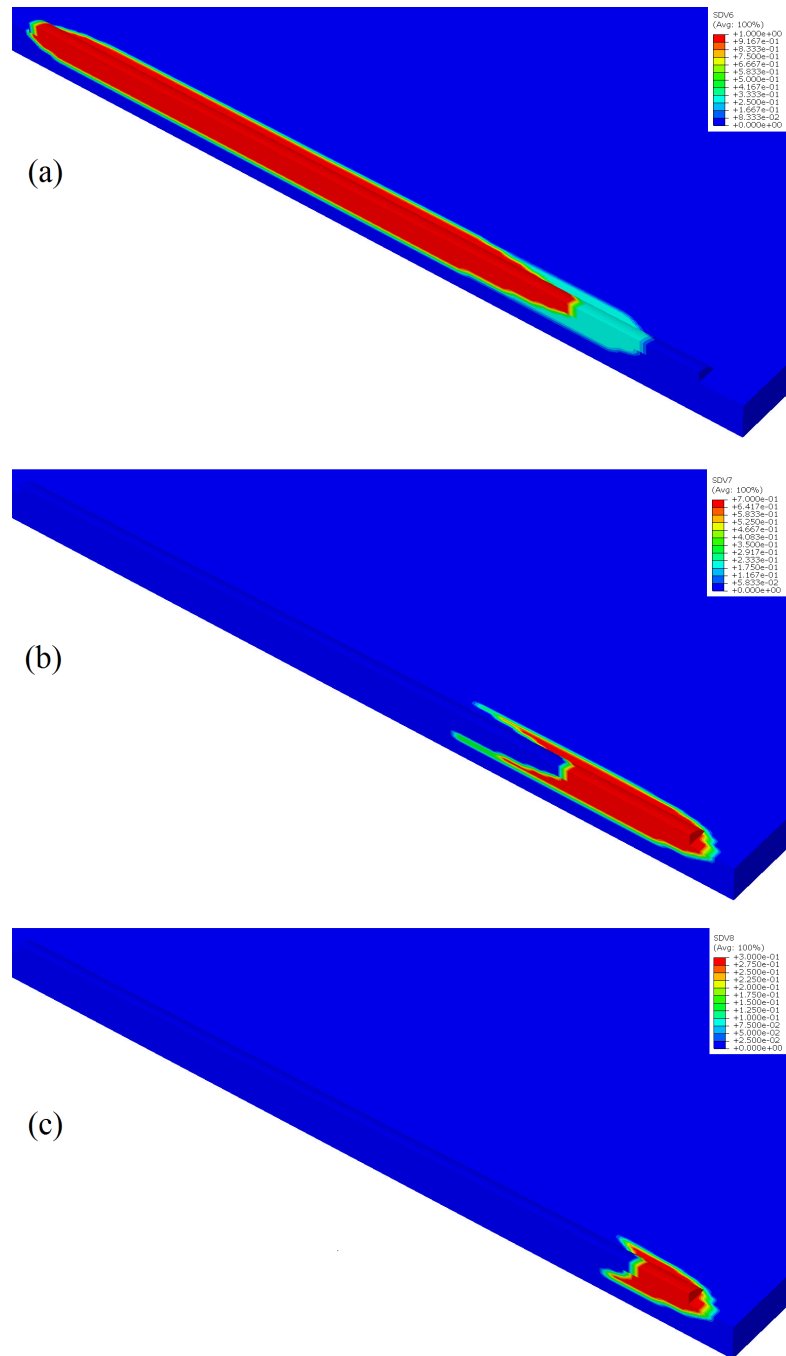


Figure 37. Predicted fractions of austenite (a), bainite (b) and martensite (c) at $t = 25$ s.

It must be elucidated that in the figure 37 (a), all the points whose temperature exceeded A_1 temperature, were considered to transform to austenite. Although at temperatures higher than almost 1400°C austenite is unstable, no differentiation has been made between liquid phase and austenite and once an element reached fully austenitization temperature it was assumed to be 100% austenite. That is to say, all the points in cooling experienced austenite decomposition, were included in SDV6. Prediction of structure composition and boundaries

of HAZ in the subzones whose temperature exceeded A_1 temperature, namely ICHAZ, CGHAZ and FGHAZ were also incorporated in the metallurgical analysis. The figure 38 demonstrates fraction of bainite and martensite formed in HAZ and FZ upon decomposition of austenite in cooling.

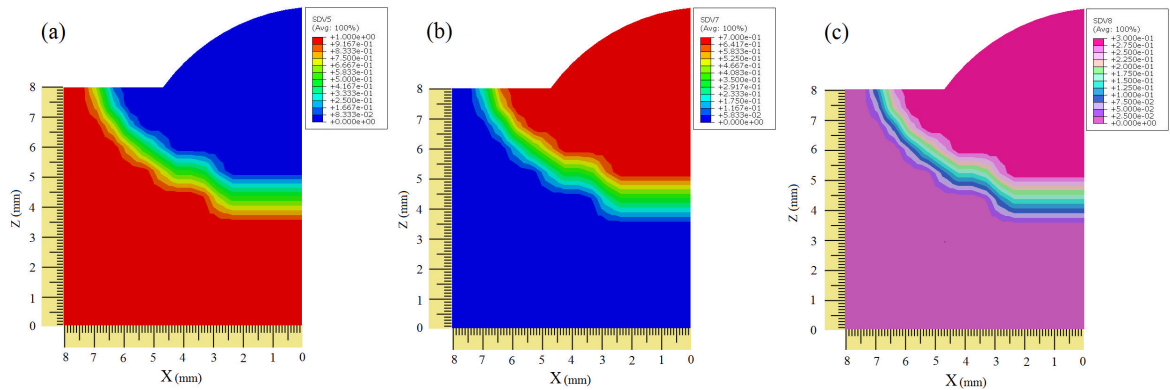


Figure 38. Volume fractions of untransformed base metal (a), formed bainite (b) and martensite (c).

In the figure 38 (a), SDV5 represents the volume fraction of parent material which might be untransformed, partially transformed or fully transformed. In the case of transformation to austenite, in cooling stage, bainite and martensite will form whose volume fractions in HAZ and FZ are respectively shown in the figures 38 (b) and 38 (c).

Microstructural observation of the welded work piece in the HAZ, confirms the results of FE simulation with respect to the presence of a mixture of bainite and martensite in which volume fraction of bainite is greater than martensite, as is shown in the figure 39. Grain growth in HAZ and prior-austenite grain boundaries are clearly shown in an SEM image in the figure 39 (a). A mixture of bainite and martensite in the HAZ microstructure of the welded plate is observable as is depicted in the figure 39 (b).

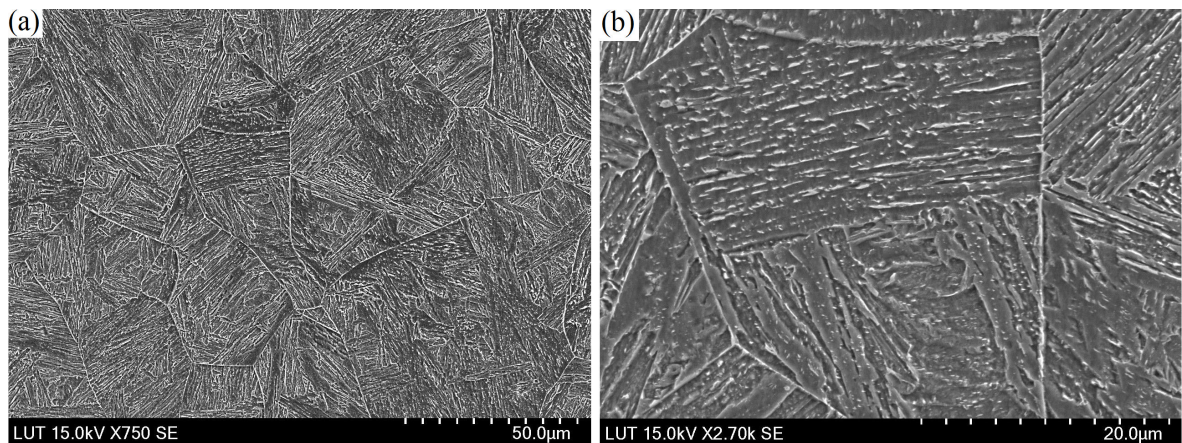


Figure 39. SEM micrographs of HAZ, Prior austenite grain boundaries (a), a mixture of bainite and martensite (b).

6.3 Analysis of transverse residual stresses

The effect of SSPT on welding residual stresses is clarified considering two cases, one takes into account phase transformation and associated volumetric change in evaluation of residual stresses, while the other one neglects the effect of volume change. Transverse residual stresses (S_{11}) in this study, perpendicular to welding direction at a cross-section and half way through the weld line for both simulation cases were determined after cooling stage.

It was assumed that transverse residual stresses are symmetrical with respect to the weld centerline and hence, only half of the test piece was considered both in simulation and experimental measurements. Those stresses are reported as a function of distance from the weld toe on top surface and plotted versus experimental measurements of surface transverse residual stresses using XRD technique. The figure 40 depicts distribution of measured transverse residual stresses versus simulations with and without considering SSPT.

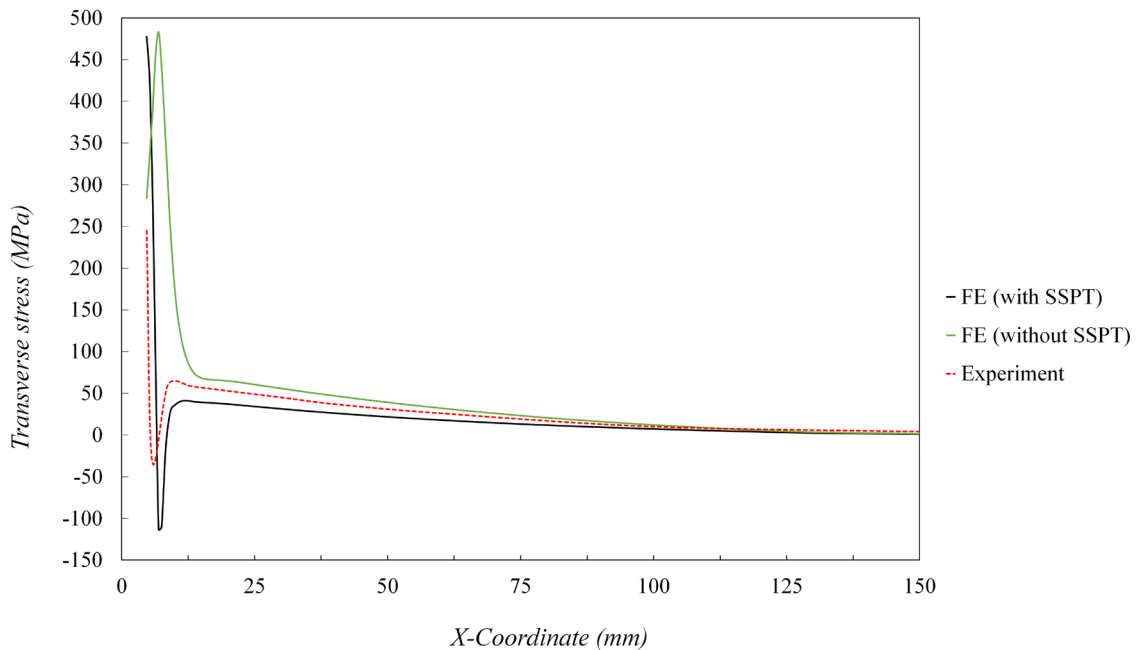


Figure 40. Transverse residual stresses from experimental measurements and FE simulations.

Measurements reveal occurrence of phase transformation in HAZ where volume expansion led to reduction of the magnitude of residual stresses and even change the sign of stresses from positive to negative (tensile to compressive). As the distance from the HAZ towards the outer edges increases, the effect of volume change decreases and magnitude of transverse stresses rises up to 60 MPa which gradually levels out to zero at the outer edges of the base plate.

The model without SSPT effect, predicts the stress distribution trend in HAZ completely different with experimental measurements. Such model predicts transverse stresses to be entirely tensile in the HAZ with a maximum tensile value at the point which in reality experienced maximum compressive stress due to phase transformation. Farther away from HAZ, tensile stresses decrease considerably and the pertinent distribution curve becomes closer to experimental one as stresses relax towards the edges. A significantly improved model to predict the distribution of transverse stresses was obtained taking the effect of SSPT into account.

As is shown in the figure 40, the general trend predicted by the SSPT model is more in agreement with the reality compared to the model without SSPT effect. This model is able to take into consideration the volume change due to formation of bainite and martensite which cause consequential expansion and formation of compressive residual stresses as a consequence in HAZ, however, the magnitude of maximum tensile and compressive transverse stresses calculated by this model, are higher than the measured values. On travelling towards base metal from HAZ, this model predicts the stresses turn from compressive to tensile and levelling off to zero, nonetheless, in relaxation of stresses, the values from SSPT model are slightly smaller than the experimental ones.

6.4 Analysis of Deformations

A comparison has been made between the results of the FE models and experimental measurements of out of plane displacements, namely angular distortion and bending deformations. The figure 41 shows the displacement contours of the simulated model considering SSPT.

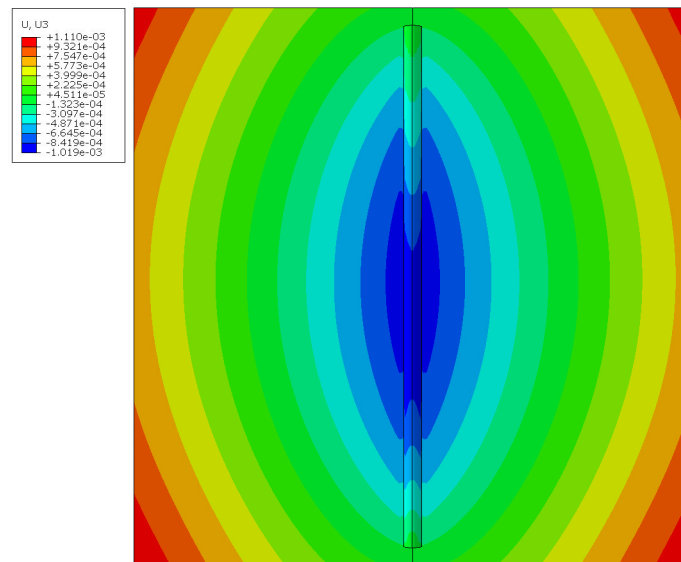


Figure 41. Displacement contours (U_3) after cooling and relaxation. (Dimensions in m)

Angular distortion as is observable in the figure 41, is symmetrical with respect to the weld seam and rises as the distance from weld line towards the outer edges increases. The results of measuring the angular distortions versus the simulated cases (one considers the effect of SSPT while the other one ignores such effect) are depicted in the figures 42 and 43, respectively for the path 1 and 2.

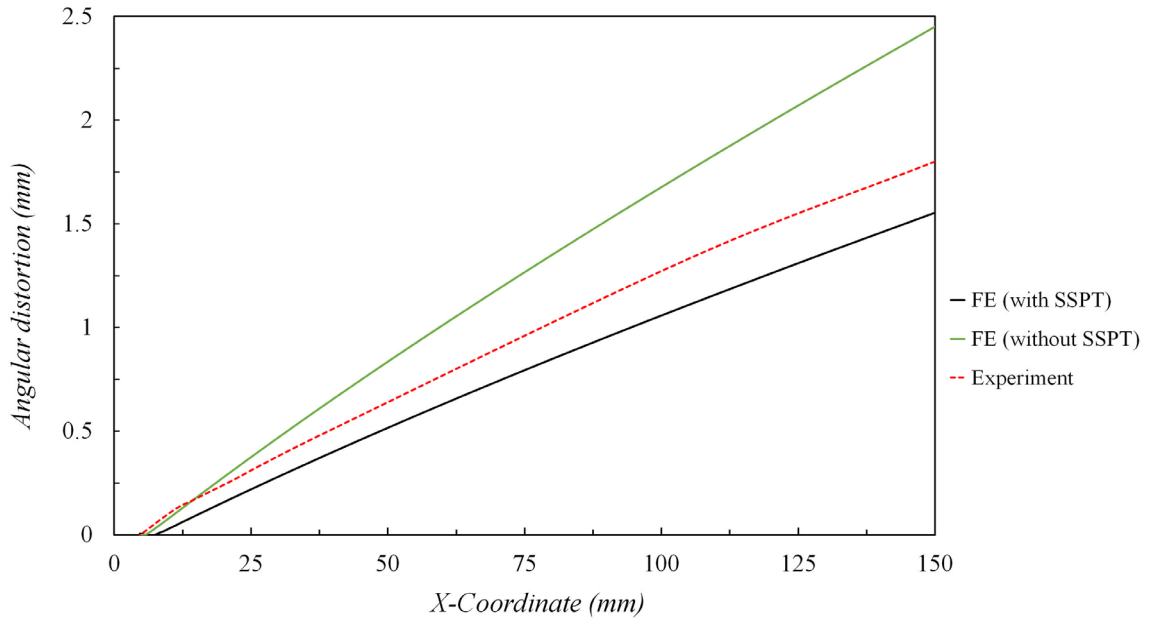


Figure 42. Angular distortion along the path1.

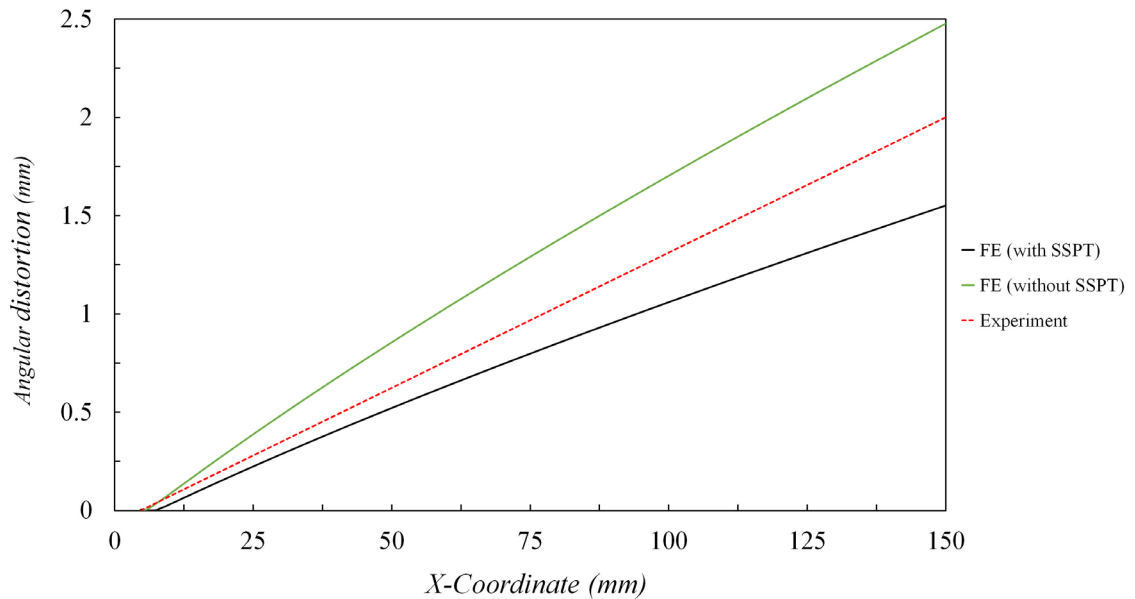


Figure 43. Angular distortion along the path2.

The results of simulations show an acceptable agreement with measurements and differences of the results of both models when compared to the experimental ones, are approximately in the same range, seen from magnitude point of view. Simulated angular distortion by the model considering the effect of SSPT is smaller than the measured ones, whereas, the model ignoring the SSPT effect, overestimates the angular deformation in contrast to the experiment. Smaller values predicted for angular displacement by the SSPT model, is originated from the volume increase during bainitic and martensitic transformations resulting in smaller angular distortion which is in concurrent with the findings of a study by Deng (2009). Out of plane bending deformation predicted by the two models are plotted versus the experimentally measured one in the figure 44.

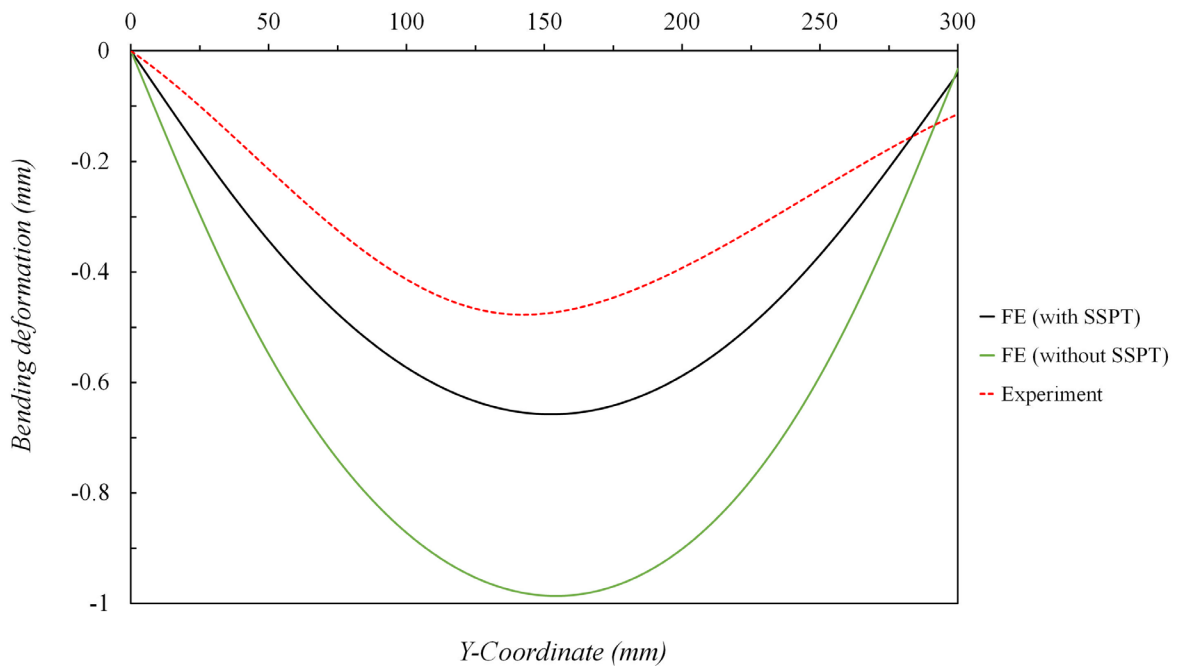


Figure 44. Simulated versus measured bending deformation.

Magnitude of bending distortion compared to the angular deformation is smaller in this study and is limited to fraction of a millimeter. Both simulation cases overpredicted bending deformation, nevertheless, smaller discrepancy is resulted between the prediction of the model taking into account phase transformation and experiment, while the results of the simulation ignoring the effect of SSPT sustain a large distance from the measurements.

7 CONCLUSION

This thesis concerns simulation of single pass bead on plate gas metal arc welding of low carbon ultra-high strength steel Strenx[®]960 MC. In this regard, a three-dimensional sequentially-coupled TMM model in FE code ABAQUS was developed to analyze the temperature field during welding, volume fraction of present phases during diffusional and displacive transformations as well as incorporation the effect of SSPT in prediction of transverse residual stresses and deformations by applying volumetric changes during austenitic, bainitic and martensitic transformations.

Analysis the temperature histories for the investigated material showed that employing anisotropic thermal conductivity, yields remarkably more accurate results compared to the model applies isotropic conductivity. The reason was speculated to be the specific rolling and quenching and in general, manufacturing process of the material and consequent effect on microstructure and size of grains which lead to anisotropic properties and reduced heat transportation in through thickness direction. Notwithstanding the accurate results of such model in evaluation of thermal field, a more in depth further study is required to investigate the effect of rolling process on anisotropy of thermal conductivity.

The model shows desirable potential to predict formation of martensite and bainite and pertinent volume fractions in the HAZ based on the mathematical kinetics models for both diffusive and diffusionless transformations.

The results of the stress analysis indicate the necessity of incorporating the effect of SSPT in evaluation of welding-induced residual stresses for high strength carbon steels and in particular, the material under investigation. It is clear that volume changes during bainite and martensite transformations and relatively large full volumetric change strain of martensite in Strenx[®]960 MC, have significant effects on not only magnitude of but also the sign of the residual stresses in the HAZ. Based on the results of mechanical analysis, although both simulation models have differences with the experimental curve in terms of the maximum magnitude of tensile and compressive stresses, the model which considers phase transformation, can predict the general trend of transverse residual stress distribution

in HAZ, more realistically compared to the model ignoring this effect and renders agreement with experimental measurements. A further study is required to take into account transformation plasticity as well as changes in yield strength due to phase transformations to improve the findings of this thesis.

Results of angular distortion analysis implies both simulation models can predict out of plane angular deformation in close agreement with experiments, however, the model with SSPT effect due to considering volume expansion in bainitic and martensitic transformations, shows relatively smaller angular distortion compared to the model neglecting this effect. Out of plane bending deformation analysis shows the superiority of the model with SSPT effect in prediction of such distortion in contrast to the model without SSPT when compared to the experimental measurements.

REFERENCES

- ABAQUS, 2017. *User's manual*, Dassault Systèmes®.
- Ahn, J. et al., 2017. Prediction and Measurement of Residual Stresses and Distortions in Fibre Laser Welded Ti-6Al-4V Considering Phase Transformation. *Materials and Design*, Volume 115, pp. 441-457.
- Amraei, M., Dabiri, M., Björk, T. & Skriko, T., 2016. Effects of Workshop Fabrication Processes on the Deformation Capacity of S960 Ultra-high Strength Steel. *Journal of Manufacturing Science and Engineering*, 138(12).
- Anca, A., Cardona, A., Risso, J. & Fachinotti, V. D., 2011. Finite element modeling of welding processes. *Applied Mathematical Modelling*, 35(2), p. 688–707.
- Aoki, S., Nishimura, T. & Hiroi, T., 2005. Reduction method for residual stress of welded joint using random vibration. *Nuclear Engineering and Design*, 235(14), pp. 1441-1445.
- Azhari, F., Heidarpour, A., Zhao, X.-L. & Hutchinson, C. R., 2015. Mechanical properties of ultra-high strength (Grade 1200) steel tubes under cooling phase of a fire: An experimental investigation. *Construction and Building Materials*, Volume 93, pp. 841-850.
- Barsoum, Z. & Barsoum, I., 2009. Residual stress effects on fatigue life of welded structures using LEFM. *Engineering Failure Analysis*, p. 449–467.
- Bhatti, A. A., Barsoum, Z. & Khurshid, M., 2014. Development of a Finite Element Simulation Framework for the Prediction of Residual Stresses in Large Welded Structures. *Computers & Structures*, Volume 133, pp. 1-11.
- Bhatti, A. A., Barsoum, Z., Murakawa, H. & Barsoum, I., 2015. Influence of thermo-mechanical material properties of different steel grades on welding residual stresses and angular distortion. *Materials and Design*, Volume 65, p. 878–889.

Biro, E., McDermid, J. R., Embury, J. D. & Zhou, Y., 2010. Softening Kinetics in the Subcritical Heat-Affected Zone of Dual-Phase Steel Welds. *Metallurgical and Materials Transactions A*, 41(9), p. 2348–2356.

Björk, T., Toivonen, J. & Nykänen, T., 2012. Capacity of Fillet Welded Joints Made of Ultra High-Strength Steel. *Welding in the World*, 56(3), pp. 71-84.

Brickstad, B. & Josefson, B., 1998. A parametric study of residual stresses in multi-pass butt-welded stainless steel pipes. *International Journal of Pressure Vessels and Piping*, 75(1), pp. 11-25.

Burst, F. & Kim, D., 2005. Mitigating welding residual stress. In: Z. Feng, ed. *Processes and mechanisms of welding residual stress and distortion*. Cambridge: Woodhead Publishing, pp. 264-294.

Callister, W. D., 2000. *Fundamentals of Materials Science and Engineering*. 5th ed. New York: John Wiley & Sons.

Çengel, Y. A. & Ghajar, A. J., 2015. *Heat and Mass Transfer: Fundamentals and Applications*. 5th ed. New York: McGraw-Hill Higher Education.

Chakrabarti, D., Davis, C. & Strangwood, M., 2007. Characterisation of Bimodal Grain Structures in HSLA Steels. *Materials Characterization*, 58(5), pp. 423-438.

Chao, Y., 2005. Measuring welding-induced distortion. In: Z. Feng, ed. *Processes and mechanisms of welding residual stress and distortion*. Cambridge: Woodhead Publishing, pp. 209-224.

Cheng, X. et al., 2003. Residual stress modification by post-weld treatment and its beneficial effect on fatigue strength of welded structures. *International Journal of Fatigue*, 25(9-11), pp. 1259-1269.

Chiumenti, M. et al., 2010. Finite Element Modeling of Multi-Pass Welding and Shaped Metal Deposition Processes. *Computer Methods in Applied Mechanics and Engineering*, 199(37-40), pp. 2343-2359.

Danis, Y., Lacoste, E. & Arvieu, C., 2010. Numerical modeling of inconel 738LC deposition welding: Prediction of residual stress induced cracking. *Journal of Materials Processing Technology*, 210(14), p. 2053–2061.

Deng, D., 2009. FEM prediction of welding residual stress and distortion in carbon steel considering phase transformation effects. *Materials and Design*, Volume 30, pp. 359-366.

Deng, D. & Murakawa, H., 2006a. Numerical simulation of temperature field and residual stress in multi-pass welds in stainless steel pipe and comparison with experimental measurements. *Computational Materials Science*, 37(3), pp. 269-277.

Deng, D. & Murakawa, H., 2006b. Prediction of Welding Residual Stress in Multi-Pass Butt-Welded Modified 9Cr–1Mo Steel Pipe Considering Phase Transformation Effects. *Computational Materials Science*, 37(3), pp. 209-219.

Deng, D. & Murakawa, H., 2008. Finite Element Analysis of Temperature Field, Microstructure and Residual Stress in Multi-Pass Butt-Welded 2.25Cr–1Mo Steel Pipes. *Computational Materials Science*, 43(4), pp. 681-695.

Deng, D., Murakawa, H. & Liang, W., 2007. Numerical Simulation of Welding Distortion in Large Structures. *Computer Methods in Applied Mechanics and Engineering*, 196(45-48), pp. 4613-4627.

Dorman, M. et al., 2012. Effect of laser shock peening on residual stress and fatigue life of clad 2024 aluminium sheet containing scribe defects. *Materials Science and Engineering: A*, Volume 548, pp. 142-151.

Dowling, N. E., 2013. *Mechanical Behavior of Materials*. 4th ed. London: Pearson.

- Durand-Charre, M., 2004. *Microstructure of Steels and Cast Irons*. 1st ed. New York: Springer.
- Eagar, T. & Tsai, N.-S., 1983. Temperature Fields Produced by Traveling Distributed Heat Sources. *Welding Journal*, Volume 62, pp. 346-355.
- Falkenreck, T. E., Klein, M. & Böllinghaus, T., 2017. Dynamic Compressive Behaviour of Weld Joints. *Materials Science and Engineering: A*, Volume 702, pp. 322-330.
- Fricke, S., Keim, E. & Schmidt, J., 2001. Numerical weld modeling — a method for calculating weld-induced residual stresses. *Nuclear Engineering and Design*, 26(2-3), pp. 139-150.
- Friedman, E., 1975. Thermo-mechanical analysis of the welding process using the finite element method. *Journal Pressure Vessel Technology*, Volume 97, pp. 206-213.
- Goldak, J. A. & Akhlaghi, M., 2005. *Computational welding mechanics*. 1st ed. New York: Springer.
- Goldak, J. et al., 1986. Computer Modeling of Heat Flow in Welds. *Metallurgical Transactions B.*, Volume Volume 17B, pp. 587-600.
- Goldak, J., Chakravarti, A. & Bibby, M., 1984. A New Finite Element Model for Welding Heat Sources. *Metallurgical Transactions B.*, Volume 15B, pp. 299-305.
- Grong, Ø., 1997. *Metallurgical Modeling of Welding*. 2nd ed. London: The Institute of Materials.
- Gryc, K. et al., 2013. Determination of the solidus and liquidus temperatures of the real-steel grades with dynamic thermal-analysis methods. *Materiali in Tehnologije*, 47(5), p. 569–575.
- Guo, W., 2015. *Laser Welding of High Strength Steels Doctoral. Dissertation*. Manchester: The University of Manchester.

Guo, W. et al., 2015. Microstructure and mechanical properties of laser welded S960 high strength steel. *Materials and Design*, Volume 85, p. 534–548.

Guo, W. et al., 2017. Comparison of microstructure and mechanical properties of ultra-narrow gap laser and gas-metal-arc welded S960 high strength steel. *Optics and Lasers in Engineering*, Volume 91, p. 1–15.

Hackenberg, R., 2012. The Historical Development of Phase Transformations Understanding in Ferrous Alloys. In: E. Pereloma & D. V. Edmonds, eds. *Phase Transformations in Steels: Volume 1: Fundamentals and Diffusion-Controlled Transformations*. Cambridge: Woodhead Publishing, pp. 3-55.

Hansen, J. L., 2003. *Numerical Modelling of Welding Induced Stresses. Doctoral Dissertation*. Copenhagen: Technical University of Denmark. Department of Manufacturing Engineering and Management.

Hartmann, V. W., Bell, M. & Nelson, T., 2001. Welding Metallurgy. In: C. L. Jenney & A. O'Brien, eds. *Welding Handbook*. Miami: American Welding Society, pp. 116-155.

Heinze, C., Schwenk, C. & Rethmeier, M., 2011. Numerical calculation of residual stress development of multi-pass gas metal arc welding. *Journal of Constructional Steel Research*, Volume 72, pp. 12-19.

Heinze, C., Schwenk, C. & Rethmeier, M., 2012. Effect of heat source configuration on the result quality of numerical calculation of welding-induced distortion. *Simulation Modelling Practice and Theory*, 20(1), pp. 112-123.

James, M. et al., 2006. Correlating weld process conditions, residual strain and stress, microstructure and mechanical properties for high strength steel—the role of neutron diffraction strain scanning. *Materials Science and Engineering: A*, 427(1-2), pp. 16-26.

Jonšta, P. et al., 2015. Contribution to the Thermal Properties of Selected Steels. *Metalurgija*, 54(1), pp. 187-190.

Kang, H. T., Lee, Y.-L. & Sun, X. J., 2008. Effects of residual stress and heat treatment on fatigue strength of weldments. *Materials Science and Engineering: A*, 497(1-2), pp. 37-43.

Kelly, P., 2012. Crystallography of Martensite Transformations in Steels. In: E. Pereloma & D. V. Edmonds, eds. *Phase Transformations in Steels: Volume 2: Diffusionless Transformations, High Strength Steels, Modelling and Advanced Analytical Techniques*. Cambridge: Woodhead Publishing, pp. 3-33.

Kielhorn, W. H., Adonyi, Y., Holdren, R. L. & Horrocks, Sr., R. C., 2001. Survey of Joining, Cutting, and Allied Processes. In: C. L. Jenney & A. O'Brien, eds. *Welding Handbook*. Miami: American Welding Society, pp. 2-50.

Klamecki, B. E., 2003. Residual stress reduction by pulsed magnetic treatment. *Journal of Materials Processing Technology*, 141(3), pp. 385-394.

Kou, S., 2003. *Welding Metallurgy*. 2nd ed. Hoboken: John Wiley & Sons.

Krutz, G. & Segerlind, L., 1978. Finite element analysis of welded structures. *Welding Journal*, Volume 57, pp. 211-216.

Kubiak, M. & Piekarska, W., 2016. Comprehensive Model of Thermal Phenomena and Phase Transformations in Laser Welding Process. *Computers & Structures*, Volume 172, pp. 29-39.

Lampa, C., Kaplan, A. F. H., Powell, J. & Magnusson, C., 1999. An Analytical Thermodynamic Model of Laser Welding. *Journal of Physics D Applied Physics*, 30(9), pp. 1293-1299.

Lancaster, J., 1999. *Metallurgy of Welding*. 6th ed. Cambridge: Woodhead Publishing.

Lauwagie, T. et al., 2003. Mixed Numerical–Experimental Identification of Elastic Properties of Orthotropic Metal Plates. *NDT & E International*, 36(7), pp. 487-495.

Leblond, J., Mottet, G. & Devaux, J., 1986a. A Theoretical and Numerical Approach to the Plastic Behaviour of Steels During Phase Transformations—I. Derivation of General Relations. *Journal of the Mechanics and Physics of Solids*, 34(4), pp. 395-409.

Leblond, J., Mottet, G. & Devaux, J., 1986b. A Theoretical and Numerical Approach to the Plastic Behaviour of Steels During Phase Transformations—II. Study of Classical Plasticity for Ideal-Plastic Phases. *Journal of the Mechanics and Physics of Solids*, 34(4), pp. 411-432.

Lee, C.-H. & Chang, K.-H., 2009. Finite element simulation of the residual stresses in high strength carbon steel butt weld incorporating solid-state phase transformation. *Computational Materials Science*, 46(4), p. 1014–1022.

Lee, C.-H. & Chang, K.-H., 2011. Prediction of residual stresses in high strength carbon steel pipe weld considering solid-state phase transformation effects. *Computers & Structures*, 89(1-2), pp. 256-265.

Lee, S.-I. & Koh, S.-K., 2002. Residual stress effects on the fatigue life of an externally grooved thick-walled pressure vessel. *International Journal of Pressure Vessels and Piping*, 79(2), pp. 119-126.

Lee, S.-J. & Lee, Y.-K., 2008. Finite Element Simulation of Quench Distortion in a Low-Alloy Steel Incorporating Transformation Kinetics. *Acta Materialia*, 56(7), pp. 1482-1490.

Li, H. et al., 2016. Non-Isothermal Phase-Transformation Kinetics Model for Evaluating the Austenization of 55CrMo Steel Based on Johnson–Mehl–Avrami Equation. *Materials & Design*, Volume 92, pp. 731-741.

Liljedahla, C. et al., 2009. Weld residual stress effects on fatigue crack growth behaviour of aluminium alloy 2024-T351. *International Journal of Fatigue*, 31(6), pp. 1081-1088.

- Lindgren, L.-E., 2001a. Finite Element Modeling and Simulation of Welding Part 1: Increased Complexity. *Journal of Thermal Stresses*, 24(2), pp. 141-192.
- Lindgren, L.-E., 2001b. Finite Element Modeling and Simulation of Welding Part 2: Improved Material Modeling. *Journal of Thermal Stresses*, 24(3), pp. 195-231.
- Lindgren, L.-E., 2001c. Finite Element Modeling and Simulation of Welding. Part 3: Efficiency and Integration. *Journal of Thermal Stresses*, 24(4), pp. 305-334.
- Lindgren, L.-E., 2006. Numerical Modelling of Welding. *Computer Methods in Applied Mechanics and Engineering*, 195(48-49), pp. 6710-6736.
- Lindgren, L.-E., 2007. *Computational Welding Mechanics*. 1st ed. Cambridge: Woodhead Publishing.
- Li, T.-J., Li, G.-Q. & Wang, Y.-B., 2015. Residual stress tests of welded Q690 high-strength steel box- and H-sections. *Journal of Constructional Steel Research*, Volume 115, pp. 283-289.
- Little, G. & Kamtekar, A., 1998. The effect of thermal properties and weld efficiency on transient temperatures during welding. *Computers & Structures*, 68(1-3), pp. 157-165.
- Li, Y., Lu, H., Yu, C. & Wu, Y., 2015. Accurate Prediction of Welding Stress Evolution by Considering Improved Phase Transformation Model. *Materials Transactions*, 56(5), pp. 715-719.
- Macherauch, E., 1987. Introduction to Residual Stresses. In: A. Niku-Lari, ed. *Advances in Surface Treatments: Technology—Applications—Effects*. Oxford: Pergamon Press, pp. 1-36.
- Mi, G. et al., 2016. A Thermal-Metallurgical-Mechanical Model for Laser Welding Q235 Steel. *Journal of Materials Processing Technology*, Volume 238, pp. 39-48.

Min, Y., Hong, M., Xi, Z. & Jian, L., 2006. Determination of residual stress by use of phase shifting moiré interferometry and hole-drilling method. *Optics and Lasers in Engineering*, 44(1), pp. 68-79.

Mirzaee-Sisan, A. et al., 2007. Residual stress measurement in a repair welded header in the as-welded condition and after advanced post weld treatment. 84(5), pp. 265-273.

Mochizuki, M., 2007. Control of welding residual stress for ensuring integrity against fatigue and stress–corrosion cracking. *Nuclear Engineering and Design*, 237(2), pp. 107-123.

Mochizuki, M. et al., 2002. *Generation Behavior of Thermal and Residual Stresses Due to Phase Transformation During Welding Heat Cycles*. Vancouver, Proceedings of ASME Pressure Vessels and Piping Conference: Computational Weld Mechanics, Constraints and Weld Fracture, ASME PVP 434, pp. 123-129.

Moshayedi, H. & Sattari-Far, I., 2015. The effect of welding residual stresses on brittle fracture in an internal surface cracked pipe. *International Journal of Pressure Vessels and Piping*, Volume 126-127, pp. 29-36.

Nguyen, T. & Wahab, M., 1998. The effect of weld geometry and residual stresses on the fatigue of welded joints under combined loading. *Journal of Materials Processing Technology*, 77(1-3), pp. 201-208.

Nunes, JR, A., 1983. An Extended Rosenthal Weld Model. *Welding Journal* , Volume 62, pp. 165-170.

Olabi, A. & Hashmi, M., 1995. The effect of post-weld heat-treatment on mechanical-properties and residual-stresses mapping in welded structural steel. *Journal of Materials Processing Technology*, 55(2), pp. 117-122.

Paley, Z. & Hibbert, P., 1975. Computation of temperatures in actual weld. *Welding Journal*, Volume 54, pp. 385-392.

Pardo, E. & Weckman, D., 1989. Prediction of Weld Pool and Reinforcement Dimensions of GMA Welds Using a Finite-Element Model. *Metallurgical and Materials Transactions B*, 20(6), pp. 937-947.

Pavelic, V., Tanbakuchi, O., Uyehara, A. & Myers, P., 1969. Experimental and Computed Temperature Histories in Gas Tungsten-Arc Welding of Thin Plates. *Welding Journal*, Volume 48, pp. 295-305.

Pearce, S., Linton, V. & Oliver, E., 2008. Residual stress in a thick section high strength T-butt weld. *Materials Science and Engineering: A*, 480(1-2), pp. 411-418.

Piekarska, W., Kubiak, M. & Saternus, Z., 2012. Numerical Modelling of Thermal and Structural Strain in Laser Welding Process. *Archives of Metallurgy and Materials*, 57(4), pp. 1219-1227.

Pilipenko, A., 2001. *Computer simulation of residual stress and distortion of thick plates in multi-electrode submerged arc welding. Doctoral Dissertation.* Trondheim: Norwegian University of Science and Technology (NTNU), Department of Machine Design and Materials Technology.

Porter, D., Easterling, K. & Sherif, M. Y., 2009. *Phase Transformation in Metals and Alloys.* 3rd ed. Boca Raton: CRC Press.

Price, J. W. et al., 2008. Comparison of experimental and theoretical residual stresses in welds: The issue of gauge volume. *International Journal of Mechanical Sciences*, 50(3), pp. 513-521.

Qian, H., Hu, P. & Zhang, J., 2012. Effect of the Non-Equilibrium Solidus Temperature on Length of Soft Reduction Zone. *Advanced Materials Research*, Volume 476-478, pp. 139-143.

Radaj, D., 1992. *Heat Effects of Welding: Temperature Field, Residual Stress, Distortion.* 1st ed. Berlin: Springer.

Rosenthal, D., 1946. The Theory of Moving Sources of Heat and Its Application to Metal Treatments. *Transactions of the A.S.M.E.*, Volume 68, pp. 849-865.

Serth, R. W. & Lestina, T. G., 2014. *Process Heat Transfer: Principles, Applications and Rules of Thumb*. 2nd ed. Oxford: Elsevier.

Shan, X. et al., 2009. Thermo-Mechanical Modelling of a Single-Bead-on-Plate Weld Using the Finite Element Method. *International Journal of Pressure Vessels and Piping*, 86(1), pp. 110-121.

Shome, M. & Tumuluru, M., 2015. Introduction to welding and joining of advanced high-strength steels (AHSS). In: M. Shome & M. Tumuluru, eds. *Welding and Joining of Advanced High Strength Steels (AHSS)*. Cambridge: Woodhead Publishing, pp. 1-8.

Siltanen, J., Tihinen, S. & Kömi, J., 2015. Laser and laser gas-metal-arc hybrid welding of 960 MPa direct-quenched structural steel in a butt joint configuration. *Journal of Laser Applications*, 27(S2).

Skriko, T., Ghafouri, M. & Björk, T., 2017. Fatigue strength of TIG-dressed ultra-high-strength steel fillet weld joints at high stress ratio. *International Journal of Fatigue*, Volume 94, pp. 110-120.

SSAB, 2016. *Welding Handbook*. 1st ed. Oxelösund: SSAB.

Steven, W. & Haynes, A., 1956. The Temperature of Formation of Martensite and Bainite in Low Alloy Steels. *Journal of the Iron and Steel Institute*, 183(8), pp. 349-359.

Suryanarayana, C., 2012. Mechanical Behavior of Emerging Materials. *Materials Today*, 15(11), pp. 486-498.

Taljat, B., Radhakrishnan, B. & Zacharia, T., 1998. Numerical analysis of GTA welding process with emphasis on post-solidification phase transformation effects on residual stresses. *Materials Science and Engineering: A*, Volume 246, pp. 45-54.

Teng, T.-L. & Chang, P.-H., 2004. Effect of residual stresses on fatigue crack initiation life for butt-welded joints. *Journal of Materials Processing Technology*, 145(3), pp. 325-335.

Torres, M. & Voorwald, H., 2002. An evaluation of shot peening, residual stress and stress relaxation on the fatigue life of AISI 4340 steel. *International Journal of Fatigue*, 24(8), pp. 877-886.

Tsai, C. L. & Kim, D., 2005. Understanding residual stress and distortion in welds: an overview. In: Z. Feng, ed. *Processes and mechanisms of welding residual stress and distortion*. 1st ed. s.l.:Woodhead Publishing Ltd, pp. 3-31.

Ueda, Y., Murakawa, H. & Ma, N., 2012. *Welding deformation and residual stress prevention*. 1st ed. Boston: Elsevier.

van Bohemen, S., 2012. Bainite and Martensite Start Temperature Calculated with Exponential Carbon Dependence. *Materials Science and Technology*, 28(4), pp. 487-495.

Watt, D. et al., 1988. An algorithm for modelling microstructural development in weld heat-affected zones (part a) reaction kinetics. *Acta Metallurgica*, 36(11), pp. 3029-3035.

Webster, G. & Ezeilo, A., 2001. Residual stress distributions and their influence on fatigue lifetimes. *International Journal of Fatigue*, Volume 23, pp. 375-383.

Ventsel, E. & Krauthammer, T., 2001. *Thin Plates and Shells: Theory, Analysis, and Applications*. 1st ed. New York: CRC Press.

Westby, O., 1968. *Temperature distribution in the workpiece by welding. Doctoal Dissertation*. Trondheim: Department of Metallurgy and Metals Working, Norwegian University of Science and Technology.

Yaghi, A. et al., 2006. Residual stress simulation in thin and thick-walled stainless steel pipe welds including pipe diameter effects. *International Journal of Pressure Vessels and Piping*, 83(11-12), pp. 864-874.

Yaghi, A., Hyde, T., Becker, A. & Sun, W., 2008. Finite Element Simulation of Welding and Residual Stresses in a P91 Steel Pipe Incorporating Solid-State Phase Transformation and Post-Weld Heat Treatment. *The Journal of Strain Analysis for Engineering Design*, 43(5), pp. 275-293.

Yaghi, A. et al., 2005. Residual Stress Simulation in Welded Sections of P91 Pipes. *Journal of Materials Processing Technology*, 167(2-3), pp. 480-487.

Yuan, K. & Sumi, Y., 2016. Simulation of residual stress and fatigue strength of welded joints under the effects of ultrasonic impact treatment (UIT). *International Journal of Fatigue*, 92(1), pp. 321-332.

Zhang, J. et al., 2005. A study on the relief of residual stresses in weldments with explosive treatment. *International Journal of Solids and Structures*, 42(13), pp. 3794-3806.

Zhu, X. & Chao, Y., 2002. Effects of temperature-dependent material properties on welding simulation. *Computers & Structures*, 80(11), p. 967-976.